Electrical and optical detection of spin-orbit fields

Dissertation

zur Erlangung des Doktorgrades
der Naturwissenschaften (Dr. rer. nat.)
der Fakultät für Physik
der Universität Regensburg

vorgelegt von
Robert Islinger
aus Regensburg

im Jahr 2019

Promotionsgesuch eingereicht am: 22.7.2019
Die Arbeit wurde angeleitet von: Prof. Dr. Christian H. Back

Prüfungsausschuss:	Vorsitzende:	PD Dr. M. Marganska-Lyzniak
	1. Gutachter:	Prof. Dr. C. H. Back
	2. Gutachter:	Prof. Dr. D. Weiss
	weiterer Prüfer:	Prof. Dr. D. Bougeard

Contents

1 Introduction

In recent years, great efforts have been made in solid state physics and especially in the understanding of spin-dependent phenomena [1]. The charge and spin degree of the electron opens a large research area considering applications in the storage information technology, known as spintronics [2]. The fast and efficient way of the generation, detection and manipulation of spin-polarized currents is a crucial goal for future spintronic devices. A large information density, low usage power and non-volatility are required for these devices which is already realized in the STT-MRAM[1] [3, 4]. There, the magnetization in one ferromagnetic (FM) layer is manipulated by a spin-transfer torque from a second FM layer due to the transfer of angular momentum from a spin-polarized current through an oxide tunnel barrier. If the current is sufficiently large, it can switch the magnetization. A degeneration of the tunnel barrier due to the large currents leads to a continuous research for new material systems and other ways to overcome this problem [5]. In the field of data storage technology, a main goal is to store more information on smaller areas, increase the device speed and with less cost of energy. Further, the data should be stored without losing information over time. Pushing the lower border in wafer fabrication down with newer lithography steps to several nanometers, heating effects become even more significant due to the high current densities.

Therefore, the conversion of a charge into a spin current became an enormous interest in recent years due to the possible applications for spintronic devices. In a bilayer, consisting of a ferromagnet and a non-magnetic metal (NM), different effects cause a conversion of charge into spin current. These arise from the spin-orbit interaction in the bulk NM or at the interface of the hybrid structure, and are known as the spin Hall, Rashba-Edelstein or inverse spin galvanic effect. A transverse spin current with respect to the charge current direction is generated independently of the type of non-magnetic material, which could be a normal metal [6], topological insulator [7] or a semiconductor [8]. The transverse spin current induces spin-orbit fields (SOFs) which manipulate the magnetization in the FM layer. The dynamics can be described by extending the equation of motion for the magnetization vector. An attempt to find the most efficient way to create spin currents is achieved by tuning the material parameters. However, a reliable method, to determine the strength and

[1] spin-transfer-torque magnetoresistive random access memory

symmetry of these SOFs, is crucial for the understanding and characterization of the spin-orbit fields.

There are several realized approaches which can be classified into two time scales: static and dynamic experiments. A quasi static method is the so-called two-omega method, where the SOFs are determined by the first and second harmonic Hall resistance at low frequencies for different magnetic field configurations [9]. Another dc-based method has recently been proposed, where the equilibrium position of the magnetization is altered by a low frequency ac-current [10, 11]. The displacement can be detected optically using the magneto-optical Kerr effect (MOKE). However this method is limited to materials showing not a too large in-plane magnetization. For this reason, the excitation in the experiments presented in this thesis is chosen in microwave frequency range and the SOFs can be detected with the help of the ferromagnetic resonance (FMR) technique. The precession of the magnetization is driven by a spin transfer torque (ST-FMR) from a spin current or by a spin-orbit fields (SOT-FMR) originating from the current flow through a conducting sample. In both cases, the rectified dc-voltage is carefully analyzed with respect to the magnetization angle in order to quantify the interface-induced SOFs. The strength and symmetry are derived for a single crystalline Fe/GaAs(001) system [8], where it is possible to tune the SOFs magnitude by a gate voltage [12]. The investigated Fe/GaAs(001) provides efficient SOFs as well as an ultra low damping compared to many FM/NM bilayers [13].

Furthermore, in this thesis, a new approach is demonstrated, where the SOFs can be determined optically by using time-resolved magneto-optical Kerr effect microscopy (TRMOKE) using the same excitation procedure as for the SOT-FMR method. Thereby, the impact of the SOFs on the magnetization dynamics is utilized to determine the SOFs in a very efficient manner. Moreover, this method is self-calibrated since the magnitude of the SOFs is compared to the effect of the current-induced Oersted field. Further, spurious effects from a rectifying dc-voltage can be neglected due to the direct optical measurement of the polar component of the magnetization. The experimental results are compared to micromagnetic simulations which include all contributing fields.

The thesis is organized as follows: Ch. 2 begins with the theoretical background which contains the different energy terms in the ferromagnet and are used to describe the dynamical motion of the magnetization vector by the Landau-Lifshitz-Gilbert (LLG) equation. The SOF related effects, arising in the two investigated material systems, are also introduced, and extend the LLG equation by two additional terms. The basic principle of the precessional motion of the magnetization by excitation in the microwave frequency range causing ferromagnetic resonance is discussed. The concept of spin waves is introduced together with the influence by a lateral confinement in a FM stripe and the magneto-optical Kerr effect. Ch. 3 explains the electrical and optical

experimental measurement principles as well as the used setup. The chapter ends with a discussion of two possible geometries for standing spin waves and a description of the basic principles of micromagnetic simulations. In Ch. 4, the conversion efficiency from a charge to a spin current is derived by ST-FMR for a Py/Pt bilayer. The spin Hall angle and the spin diffusion length are extracted from a platinum thickness dependence, and the results are compared to those from other techniques and material systems. In Ch. 5, the Bychkov-Rashba- and Dresselhaus-like spin-orbit fields are derived for the Fe/GaAs(001) system by the electrical SOT-FMR method along the different crystallographic axes of the GaAs. The last chapter explains the new optical approach where a unique mode pattern of standing spin waves is generated by an inhomogeneous driving torque. The resulting mode pattern can be compared to micromagnetic simulations to extract the SOFs which are in turn compared to the values obtained from the electrical method. At the end, the thesis concludes with a summary of all results.

2 Theoretical background

In order to describe the magnetic system, it is necessary to introduce first the magnetic energy contributions relevant for the magnetization in the sample. By exciting the magnetization vector in a proper way, it starts to precess around an equilibrium position and then undergoes ferromagnetic resonance under certain conditions. The motion can be modified by magnetic fields or additional torques arising from an injected current. The dynamics of the magnetization vector are in general described by the Landau-Lifshitz-Gilbert equation. In order to account for the dynamics, the ferromagnetic resonance is discussed which happens under particular conditions. Then, two important effects are treated which arise for the two investigated material system. Finally, the concept of spin waves is introduced, where the confinement by a simple stripe leads to the emergence of standing spin waves.

2.1 Magnetic energy terms

Magnetism, on a quantum mechanical level, can be described as an ensemble of interacting magnetic moments where the influence of every moment on the nearest neighbors is considered. A micromagnetic description of the ferromagnet includes different spatial scales in a continuum theory [14]. The local magnetization at every lattice point is represented by a vector field $\mathbf{M}(\mathbf{r}, t)$ with space coordinate $\mathbf{r}$ and time t [15]. The strong exchange interaction dominates on a small spatial scale below the Curie temperature[1], which is consistent with the continuum approximation due to the discrete nature of the lattice. The sum of all spins can be substituted by an integral over the vector field. One fundamental constraint is the conservation of the magnitude of the local magnetization

$$|\mathbf{M}(\mathbf{r}, t)| = M_\mathrm{S}, \tag{2.1}$$

which is equal to the spontaneous or saturation magnetization on every point in the ferromagnet. The vector field normalized by M_S leads to a reduced magnetic moment or unit vector $\mathbf{m}(\mathbf{r}, t)$. Simply, $\mathbf{m}$ is used in the following as the magnetization vector and simplifies micromagnetic simulations on a grid.

[1] A threshold temperature, above which a ferromagnet becomes paramagnetic. For the $3d$ ferromagnetic (FM) materials used in this thesis, this is about 1043 K for Fe, 631 K for Ni [14] and 871 K for Permalloy (Py, $Ni_{80}Fe_{20}$) [16].

The micromagnetic free energy G_{L} of the system in a volume V is expressed by [14]

$$G_{\mathrm{L}}(\mathbf{m}, \mathbf{H}_{\mathrm{ext}}) = \int_V \Big[A \left((\Delta m_x)^2 + (\Delta m_y)^2 + (\Delta m_z)^2 \right) + f_{\mathrm{ani}}(\mathbf{m}) - \frac{\mu_0 M_{\mathrm{S}}}{2} \mathbf{m} \cdot \mathbf{H}_{\mathrm{dem}} - \mu_0 M_{\mathrm{S}} \mathbf{m} \cdot \mathbf{H}_{\mathrm{ext}} \Big] \mathrm{d}V. \quad (2.2)$$

Here, only terms are involved which are necessary to describe the ferromagnet: the first term represents the exchange energy which increases for canted magnetization vectors between nearest neighbors. The exchange stiffness constant A is on the order of 10^{-11} J/m for a ferromagnet. The second term describes the crystal anisotropy energy which is explained in the following in more detail. The third and the last terms contribute to the magnetostatic and external applied fields, respectively. The magnetostatic field $\mathbf{H}_{\mathrm{dem}}$ is determined by using the Maxwell equations in order to account for the charges at the surface of the ferromagnet.

In single-crystalline samples, the so-called magneto-crystalline anisotropy leads in general to energetically favored directions for the magnetization. In the case of $3d$ ferromagnets, the $3d$ orbitals are partially filled, however, the orbital moments are almost quenched by the crystal field with a small orbital moment left. Due to spin-orbit coupling, the spin moment is coupled to the residual orbital moment and hence to the lattice arrangement leading to an energy density with the same symmetry as the crystal [1]. With the projections of the magnetization onto unit vectors of the crystal $\alpha_i = \mathbf{m} \cdot \hat{e}_i$, the energy density for a cubic system can be given in lowest order as [17]

$$E_{\text{4-fold}} = K_4(\alpha_x^2\alpha_y^2 + \alpha_y^2\alpha_z^2 + \alpha_x^2\alpha_z^2) = \frac{K_4}{2}(1 - \alpha_x^2 + \alpha_y^2 + \alpha_z^2), \quad (2.3)$$

with K_4 as the cubic or four-fold crystalline anisotropy constant. In the used Fe/GaAs system, an additional uniaxial in-plane (*ip*) component arises from an Fe/GaAs interface and causes a two-fold symmetry [18]. Further, a uniaxial out-of-plane (*oop*) term is generated by reducing the iron film thickness down to a few nanometers [17]. The resulting energy with only first order terms then reads [19]

$$E_{\mathrm{ani}} = -\frac{K_4^{\parallel}}{2}(\alpha_x^4 + \alpha_y^4) - \frac{K_4^{\perp}}{2}\alpha_z^4 - K_{\mathrm{uni}}^{\parallel}\frac{(\hat{\mathbf{n}} \cdot \mathbf{m})^2}{M_{\mathrm{S}}^2} - K_{\mathrm{uni}}^{\perp}\alpha_z^2 \quad (2.4)$$

with $K_{\mathrm{uni}}^{\parallel}$ and $K_{\mathrm{uni}}^{\perp}$ as the *ip* and *oop* uniaxial anisotropy constant, respectively. Here, the unit vector $\hat{\mathbf{n}}$ points along the uniaxial anisotropy direction. In this thesis, a compound of nickel and iron, named permalloy (Py), is investigated, which consists of 80% nickel and 20% iron atoms. The ratio of this alloy is designed to compensate the four-fold and uniaxial magneto-crystalline

anisotropies. Due to the small coercive field, this type of ferromagnet is often called soft magnetic because the anisotropies vanish [20].

The equilibrium state of the ferromagnetic system for a given externally applied magnetic field is found at $\delta G_\mathrm{L} = 0$ while varying the magnetization vector $\mathbf{m}$ and calculating the change in the Gibb's free energy Eq. (2.2). This issue was expressed by Brown [15]

$$\mathbf{m} \times \mathbf{H}_\mathrm{eff} = 0, \tag{2.5}$$

where the torque between the magnetization and an effective field must be zero. The effective field $\mathbf{H}_\mathrm{eff}$ is the sum of the four individual fields in Eq. (2.2)

$$\mathbf{H}_\mathrm{eff} = \mathbf{H}_\mathrm{ex} + \mathbf{H}_\mathrm{ani} + \mathbf{H}_\mathrm{dem} + \mathbf{H}_\mathrm{ext}, \tag{2.6}$$

where each field can be derived by the variation of the energy with respect to the magnetization $\mathbf{m}$.

2.2 Landau-Lifschitz-Gilbert (LLG) equation

The response of the system after excitation is a more interesting topic to examine. After experiencing a perturbation away from the equilibrium position, the temporal observation of the magnetization dynamics can used to further understand the magnetic properties. For a non-zero torque $\mathbf{m} \times \mathbf{H}_\mathrm{eff} \neq 0$, the system is no longer in the equilibrium position and evolves in time due to the prevailing dynamics.

The spatial and temporal evolution of $\mathbf{m}$ can be explained in the following within a relaxation process. Gilbert proposed an equation of motion for the magnetization vector [21]

$$\frac{\mathrm{d}\mathbf{m}}{\mathrm{d}t} = -\gamma \mathbf{m} \times \mu_0 \mathbf{H}_\mathrm{eff} + \alpha \mathbf{m} \times \frac{\mathrm{d}\mathbf{m}}{\mathrm{d}t} = \mathbf{T}_\mathrm{eff} + \mathbf{T}_\mathrm{damp}, \tag{2.7}$$

when it gets tilted out-of-the equilibrium state by a perturbation including a damping mechanism. Here, γ is noted a precession rate or the gyromagnetic ratio, which is given by $\gamma = g|e|/(2m_e)$ with the Landé factor g, the electron charge e and the mass m_e. The second terms exhibits a phenomenologically introduced Gilbert damping parameter α [22]. The expression can be split up into two parts, namely a precessional term which exerts an effective field-like torque $\mathbf{T}_\mathrm{eff}$ and a damping-like torque $\mathbf{T}_\mathrm{damp}$ on the magnetization.

The first term of Eq. (2.7) induces a precession of the magnetization vector around an effective magnetic field $\mathbf{H}_\mathrm{eff}$ which is introduced in Eq. (2.5). Fig. 2.1(a) sketches the precessional motion of $\mathbf{m}$ on a cone around $\mathbf{H}_\mathrm{eff}$ at an angle θ_c with an angular frequency $\omega = 2\pi f$. For a free electron, typical precession frequencies are in the range of several gigahertz (GHz). The equilibrium condition is specified by $\mathbf{m}_\mathrm{eq} \times \mathbf{H}_\mathrm{eff} = 0$ and aligns the equilibrium

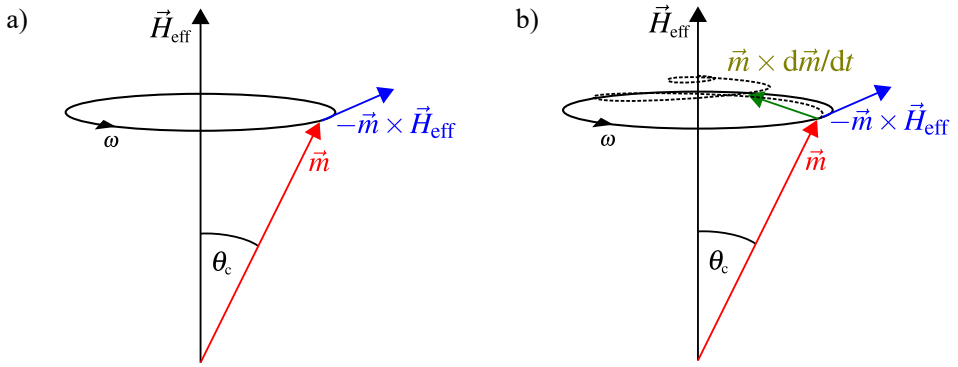

Figure 2.1: The trajectory of the magnetization vector around an effective field $\mathbf{H}_{\text{eff}}$ with only the precession term a) and with an additional damping term b). The first term in Eq. (2.7) describes the precessional motion around $\mathbf{H}_{\text{eff}}$ at a frequency ω. The second term tries to align $\mathbf{m}$ parallel to $\mathbf{H}_{\text{eff}}$ in the equilibrium position and leads finally to a spiral trajectory towards the equilibrium position along the effective field.

magnetization with the effective field. For any non-collinear $\mathbf{m}$ with respect to $\mathbf{H}_{\text{eff}}$, a driving torque $\mathbf{T}_{\text{eff}}$ leads to a precessional motion around the effective field. This would keep going forever and preserves the total energy, which is unphysical.

Therefore, a damping term accounts for the loss of energy, which is proportional to the precession velocity [23]. A proportionality factor α, the so-called Gilbert damping parameter, denotes the strength of the phenomenologically introduced term. This quantity refers to the intrinsic magnetic damping, is dimensionless and material dependent. The damping-like torque tries to align the magnetization parallel along the effective field due to the cross product $\mathbf{m} \times \mathrm{d}\mathbf{m}/\mathrm{d}t$. Fig. 2.1(b) shows the trajectory of $\mathbf{m}$ moving on a spiral curve (dashed line) towards the effective field $\mathbf{H}_{\text{eff}}$.

Additional torques can be generated for instance by electrical currents in heterostructures like a ferromagnetic metal/normal metal (FM/ NM) or ferromagnetic metal/semiconductor (FM/SMC) bilayer. Those torques are added to the LLG and will affect the magnetization dynamics in different ways. In this thesis, two current-induced torques will manipulate the magnetization:

- the spin-transfer torque (STT) caused by a transfer of angular momentum originating from a spin current, theoretically predicted by Berger [24] and Slonczewski [25].

- the spin-orbit torque (SOT) generated by a spin accumulation at an interface due to the spin-orbit coupling [1, 9].

Since $|\mathbf{M}| = M_{\text{S}}$ holds, these torques can be split into two orthogonal parts

with respect to the previously defined effective field. They read

$$\mathbf{T}_{\mathrm{FL}} = -\gamma\tau_{\mathrm{FL}}\mathbf{m}\times\boldsymbol{\sigma}_{\mathrm{FL}}, \tag{2.8}$$

$$\mathbf{T}_{\mathrm{DL}} = \gamma\tau_{\mathrm{DL}}\mathbf{m}\times(\mathbf{m}\times\boldsymbol{\sigma}_{\mathrm{DL}}), \tag{2.9}$$

with $\boldsymbol{\sigma}_{\mathrm{FL,DL}}$ as the unit vector of spin-polarization direction and $\tau_{\mathrm{FL,DL}}$ as strength of the underlying torques [22]. The torque $\mathbf{T}_{\mathrm{FL}}$ in Eq. (2.8) has the same form as the first term in the LLG and induces a precession of the magnetization if $\mathbf{H} \parallel \boldsymbol{\sigma}_{\mathrm{FL}}$. Therefore, this term is called field-like torque and acts perpendicular to $\mathbf{m}$. The damping-like torque in Eq. (2.9) shows a double cross product and also generates a torque perpendicular to the magnetization. This conducts to a reduction or enhancement of the former introduced damping torque $\mathbf{T}_{\mathrm{damp}}$. For this reason, this term is called damping-like torque since it is similar to the second term of Eq. (2.7). The extended LLG equation with the two torques reads:

$$\frac{\mathrm{d}\mathbf{m}}{\mathrm{d}t} = -\gamma\mathbf{m}\times(\mu_0\mathbf{H}_{\mathrm{eff}}+\tau_{\mathrm{FL}}\boldsymbol{\sigma}_{\mathrm{FL}})+\alpha\mathbf{m}\times\frac{\mathrm{d}\mathbf{m}}{\mathrm{d}t}+\gamma\tau_{\mathrm{DL}}\mathbf{m}\times(\mathbf{m}\times\boldsymbol{\sigma}_{\mathrm{DL}}). \tag{2.10}$$

Basically, the magnetization can be manipulated by current-induced torques which are generated by either pure spin currents in the ferromagnetic material via the interface or by spin accumulation. Both field- and damping-like torques originate from the spin-orbit coupling, however, the magnitude and sign depend on the used material. These torques can act on $\mathbf{m}$ in two possible ways. First, spin currents enter the ferromagnetic layer through an interface, gets absorbed and transports angular momentum to the FM. Thereby, a damping-like torque acts on the magnetization. Second, a spin accumulation, non-collinear with the magnetization, engages a precession around the local magnetization due to exchange coupling and vice versa [26]. Both torques originate from either a 3D spin-orbit coupling (SOC) effect called spin Hall effect (SHE) or a 2D SOC effect called Rashba-Edelstein effect (REE).

2.3 Spin-orbit coupling related effects (I) - FM/NM bilayer

In this section, the basic concept of spin currents and spin accumulation are discussed for the case of a FM/NM bilayer. Further, the spin Hall effect is introduced, which generates a spin-polarized current in the heavy metal due to the spin-orbit coupling. The transport of angular momentum to the attached ferromagnetic layer causes a torque on the magnetization in the FM and leads to precession of $\mathbf{m}$. Finally, the properties of the FM/NM interface are discussed in the light of the transmission and absorption of the spin currents.

2.3.1 Spin current and diffusion

Spin-orbit coupling is defined as the interaction of the electron's spin with the gradient of the electrical field which can be imagined as a magnetic field in the rest frame of the electron due to relativistic effects

$$H_{\mathrm{SO}} = \frac{\hbar}{4m_e^2c^2}\left(\nabla V \times \mathbf{p}\right) \cdot \boldsymbol{\sigma} \tag{2.11}$$

with the electrostatic potential V, the momentum $\mathbf{p}$ and the Pauli spin matrices $\boldsymbol{\sigma}$.

For example, spin-polarized currents can be generated by a charge current flow in a FM, where different conductivities for spin up and down electrons are present. The difference in electron spins $j_{\mathrm{s}} = j^{\uparrow} - j^{\downarrow}$ defines the resulting net spin current next to the normal charge current $j_{\mathrm{c}} = j^{\uparrow} + j^{\downarrow}$. The spin current can pass an interface to a normal metal or semiconductor, where it is transmitted with a certain efficiency. Away from the interface, the electron current has to be unpolarized $j_{\mathrm{s}} = 0$, since the conductivities for both spin are equal. The transfer of spin up and down electrons from the FM to the NM/SMC goes along with an accumulation of spins at the interface by a splitting of the chemical potentials $\mu^{\uparrow}$ and $\mu^{\downarrow}$. The resulting spin accumulation $\mu_{\mathrm{s}} = (\mu^{\uparrow} - \mu^{\downarrow})/2$ is localized at the interface and decays with the spin diffusion length (SDL) λ_{sd} in the material.

A net spin accumulation of $\mathbf{s}\hbar/2$ can be defined with the net spin particle number $s = n^{\uparrow} - n^{\downarrow}$ of up and down spins pointing in different directions. The drift-diffusion continuity equation for a spin density is given by [27]

$$\frac{\partial s}{\partial t} + \frac{\partial}{\partial x}\left(-\mu s E - D\frac{\partial s}{\partial x}\right) = \frac{\partial s}{\partial t} - \frac{\partial}{\partial x}J_{\mathrm{S}} = -\frac{s}{\tau_{\mathrm{s}}}, \tag{2.12}$$

where J_s denotes the spin particle density, D the diffusion parameter, μ the magnetic moment and τ_{s} the spin relaxation time. Assuming a constant spin density $\partial s/\partial t = E = 0$, Eq. (2.12) reduces to

$$\frac{\partial^2 s}{\partial x^2} = \frac{s}{\lambda_{\mathrm{sd}}^2}, \tag{2.13}$$

where the spin diffusion length $\lambda_{\mathrm{sd}} = \sqrt{D\tau_{\mathrm{s}}}$ quantifies a characteristic distance for a conserved spin transport [1]. The SDL in metals is only several nanometers compared to micrometers in semiconductors [28].

A spatially varying spin density or spin accumulation from a FM/NM interface into the FM layer can be mathematically described by the following expression for a spin current density

$$j_{\mathrm{s}}(x) = j_{\mathrm{s}}^0 \exp(-\frac{x}{\lambda_{\mathrm{NM}}}) \tag{2.14}$$

with an initial spin current density $j_{\mathrm{s}}^0 = -D\partial s(x=0)/\partial x$ at $x = 0$.

2.3.2 Spin Hall effect (SHE)

The spin Hall effect describes the conversion of a charge current into a transverse spin current in the absence of external magnetic fields by the spin-orbit coupling in a normal metal. The effect was discovered in 1971 by Dyakonov and Perel [29] and brought back into attention in 1999 by Hirsch [30]. The first observations were made in semiconductors [28], which sparked interest in the research for FM/NM systems. There, the magnetization can be manipulated and switched by injecting charge currents [31–33].

The phenomenon is based on the spin-dependent asymmetric scattering of unpolarized electrons in the NM material. The spin-orbit coupling originates from the band structure of the material (intrinsic) or from impurities (extrinsic) and leads to a coupling between spin and charge currents. Thereby, a transverse pure spin current is created from a charge current and vice versa due to the Onsager principle [34]. Both conversions are connected via the effective spin Hall angle $\theta_{\mathrm{SHA}}^{\mathrm{eff}}$ to

$$j_{\mathrm{c}} = \frac{2|e|}{\hbar}\theta_{\mathrm{SHA}}^{\mathrm{eff}} j_{\mathrm{s}}, \tag{2.15}$$

where the spin Hall angle has values between $0 < \theta_{\mathrm{SHA}}^{\mathrm{eff}} < 1$ for FM/NM material system and can be denoted as an effective SHA if a transparent interface is considered. Thereby, a charge current through for example a NM stripe does lead to a spin accumulation at all boundaries perpendicular to the current direction.

Two type of spin currents arise in a thin stripe due to the symmetry of the system with an in-plane charge current flow $\mathbf{j} = j_x\hat{x}$: first, spin currents in both z directions which are in-plane spin-polarized. Second, two in-plane spin currents along the y directions with *oop* spin-polarization. These four spin currents cause spin accumulation at all interfaces of the stripe. However, only at one interface, one part of the spin accumulation diffuses into the attached FM layer, where the perpendicular component with respect to $\mathbf{m}$ gets absorbed. Thereby, angular momentum is transferred to e.g. a FM film which influences the magnetization dynamics. The torques depend on the bulk properties of the NM as well as on the FM/NM interface. The other part of the spin current is reflected back into the NM layer. Therefore, the interface has also to be taken into account which is discussed in the following.

2.3.3 Interface effects and torques

The torque, generated via the transfer of angular momentum through an interface, is the so-called spin transfer torque (ST). It can be decomposed into the two terms [26]

$$\mathbf{T} = \frac{\gamma}{\tau_{\mathrm{ex}} M_{\mathrm{S}}}\mathbf{m}\times\mathbf{s} + \frac{\gamma}{\tau_{\mathrm{damp}} M_{\mathrm{S}}}\mathbf{m}\times(\mathbf{m}\times\mathbf{s}), \tag{2.16}$$

depending on the orientation of the cross product. The first term describes the precession of the spin accumulation **s** around the local magnetization **m** due to exchange coupling. The second term is perpendicular to this precessional motion, which is similar to the previously mentioned damping-like term. The damping process is fast in the treated metallic ferromagnets and any non-collinear spin accumulation leads to a relaxation of the transverse spin current within a few lattice constants [35]. Therefore, it is justified to assume an instant torque at the interface. The relaxation of the collinear spin accumulation occurs by transferring angular momentum to the lattice. Finally, the drift diffusion equation from Eq. (2.12) is solved and the resulting damping- and field-like torques are obtained [26]

$$\mathbf{T}_{\mathrm{FL}} = \gamma\tau_{\mathrm{FL}}\mathbf{m} \times \boldsymbol{\sigma}_{\mathrm{FL}}, \tag{2.17}$$

$$\mathbf{T}_{\mathrm{DL}} = \gamma\tau_{\mathrm{DL}}\mathbf{m} \times (\mathbf{m} \times \boldsymbol{\sigma}_{\mathrm{DL}}). \tag{2.18}$$

with the field- and damping-like unit-vector of the spin polarization direction, see Eq. (2.9). The two spin injection efficiencies are given by

$$\tau_{\mathrm{DL,FL}} = -\frac{\hbar}{2|e|\mu_0 M_{\mathrm{S}} \mathrm{d}_{\mathrm{FM}}} \eta_{\mathrm{FL,DL}}\, \theta_{\mathrm{SHA}}^{\mathrm{eff}}\, j_{\mathrm{c}}, \tag{2.19}$$

and the magnitude is between $0 < \eta_{\mathrm{FL,DL}} \leq 1$.

The equation for the current conversion, Eq. (2.15), can be rewritten with a normalized spin Hall angle $\theta^{\mathrm{norm}} = \eta_{\mathrm{DL}}\theta_{\mathrm{SHA}}$ by considering the interface of the heterostructure. In order to evaluate the experimental data, an exact knowledge of the interface properties is necessary. Therefore, an expression for the spin injection efficiency η_{trans} was proposed [36]

$$\eta_{\mathrm{trans}} = \left(1 - \frac{1}{\cosh(\frac{d_{\mathrm{NM}}}{\lambda_{\mathrm{NM}}})}\right), \tag{2.20}$$

which is the first part of a full calculation of the drift diffusion equation with a boundary condition of a vanishing transverse spin accumulation [26]. The interface reflectivity η_{trans} depends on the thickness of the NM layer in comparison to the spin diffusion length of the used material. If the NM layer thickness reaches the spin diffusion length λ_{NM}, η_{trans} saturates due to the cosh-term and the net spin current across the interface stays constant due to the backflow from the NM/substrate interface [37].

Further, two parameters are required for calculating the interface resistance: first, the effective spin-mixing conductance (SMC) [26]

$$g_{\mathrm{eff}}^{\uparrow\downarrow} = \mu_0 M_{\mathrm{S}} d_{\mathrm{FM}}\, \mathrm{e}\, \frac{\alpha_{\mathrm{NM}} - \alpha_0}{\gamma\hbar}, \tag{2.21}$$

which accounts for the difference of the Gilbert damping parameter between a FM/NM layer and a sample with only a FM layer (α_0). And second, the

knowledge of the bulk conductivity of the normal metal layer σ_0 is needed, which can be determined by a conductivity measurement.

The resulting expression for the damping-like injection efficiency η_{DL} can be written as [38]

$$\eta_{\mathrm{DL}} = 2\frac{e^2}{h} g_{\mathrm{eff}}^{\uparrow\downarrow} \frac{\lambda_{\mathrm{NM}}}{\sigma_{\mathrm{NM}}} \tanh\left(\frac{d_{\mathrm{NM}}}{2\lambda_{\mathrm{NM}}}\right). \tag{2.22}$$

A normalized product of the spin injection efficiency and the spin Hall angle can be defined as

$$(\eta_{\mathrm{DL}}\theta_{\mathrm{SHA}}^{\mathrm{eff}})^{\mathrm{norm}} := \eta_{\mathrm{DL}}\theta_{\mathrm{SHA}}^{\mathrm{i}} \frac{h}{2e^2} \frac{\sigma_{\mathrm{NM}}}{g_{\mathrm{eff}}^{\uparrow\downarrow}} = \theta_{\mathrm{SHA}}^{\mathrm{i}}\, \lambda_{\mathrm{NM}} \tanh\left(\frac{d_{\mathrm{NM}}}{2\lambda_{\mathrm{NM}}}\right), \tag{2.23}$$

where the effective spin Hall angle is normalized by the factor $h\sigma_{\mathrm{NM}}/2e^2 g_{\mathrm{eff}}^{\uparrow\downarrow}$. An interface-related SHA $\theta_{\mathrm{SHA}}^{\mathrm{i}}$ is introduced, which can be determined by the fit of a tanh-function in a NM layer thickness dependence. Thereby, also the spin diffusion length λ_{NM} can be extracted [38–40].

2.4 Spin-orbit coupling related effects (II) - Fe/GaAs system

In this section, the Rashba-Edelstein effect (REE) is discussed [41, 42]. It can be understood as transverse in-plane spin-polarization generated at the interface of a normal metal by application of an electrical field. This effect was first experimentally observed by Kato [43] and Silov [44]. Basically, the Rashba effect can be seen as an effective magnetic field due to the spin-orbit coupling, which is seen by the drifting electrons in their own reference frame [45, 46]. The field generates additional terms in the Hamiltonian and removes the spin degeneracy of the energy bands.

In semiconductors with SOC, the Hamiltonian can be split up into a Dresselhaus and a Bychkov-Rashba field originating from a bulk (BIA) or structure inversion asymmetry (SIA), respectively. The Hamiltonian finally reads as

$$\mathfrak{H} = \frac{\hbar k^2}{2m^*} + H_{\mathrm{SO}}^{\mathrm{BIA}} + H_{\mathrm{SO}}^{\mathrm{SIA}}, \tag{2.24}$$

with the momentum $\hbar k^2$ and the effective mass of the electron m^*.

2.4.1 Crystal structure and anisotropy

One part of thesis was the electrical and optical determination of spin-orbit fields in thin Fe/GaAs stripes. Therefore, the treated material is briefly discussed. Gallium arsenide is a III-V semiconductor and shows a zinc-blende structure with a face-centered cubic (fcc) lattice structure. The diatomic basis contains a Ga and an As atom which can be imaged as an atom in the center of a tetrahedron with four nearest neighbor atoms at the vertex corners [48].

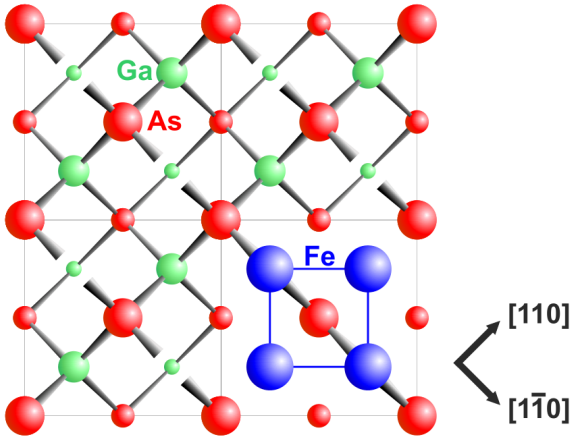

Figure 2.2: Top view of an unreconstructed GaAs(001) surface where the different size of atoms corresponds to the position of the atomic layers. The lower right section shows the unit cell of the first monolayer of Fe (blue) on the GaAs lattice with the two bonds along the [-110] direction (image taken from [47]).

Fig. 2.2 displays the top view on a GaAs(001) lattice which is not reconstructed during the Fe growth. Every atom is connected by two bonds to the lower and two bonds to the higher lattice plane to the other type of atom.

In GaAs(001), the top layer consists of either only Ga or As atoms, where a single atom shares only two bonds to the lower lattice plane. The other two bonds point into vacuum and are called dangling bonds. They are oriented along the [-110] or [110] crystallographic direction depending on whether the crystal is As- or Ga-terminated interface. For this reason, an intrinsic anisotropy emerges at the surface independent of the termination. Both directions are not equivalent and this results in a two- and four-fold anisotropy which can be described by a C_{2v} point group [49]. A Fe layer grown on GaAs(001) adapts this interface symmetry, since the lowest Fe atoms are bonded to the GaAs(001) by the two dangling bonds [1]. The Fe atoms occupy the same lattice positions since Fe grows epitaxially on GaAs. In detail, the lattice constant of GaAs ($a_{\mathrm{GaAs}} = 5.653$ Å) is almost twice as large as iron ($a_{\mathrm{Fe}} = 2.867$ Å), which results in a roughly strain-free and pseudomorphic crystalline growth [50].

In a thin Fe film attached to the GaAs(001), there exists both a cubic magneto-crystalline anisotropy originating from the bulk Fe as well as the previously introduced uniaxial magneto-crystalline anisotropy from the Fe/GaAs interface. The anisotropy energy from Eq. (2.4) for the in-plane case can be rewritten as [51]

$$\epsilon_{\mathrm{ani}}(\phi_M) = \frac{K_4^{\parallel}}{4}\sin^2(2\phi_M) + K_{\mathrm{uni}}^{\parallel}\cos^2(\phi_M), \tag{2.25}$$

where ϕ_M defines the angle between the magnetization and the [-110] direction. The two anisotropy constants $K_4^{\parallel}$ and $K_{\mathrm{uni}}^{\parallel}$ depend on the FM layer thickness and specify the strength of the four-fold and uniaxial anisotropy, respectively. The four-fold parameter is negative for films sizes thicker than one nanometer, which favors two easy axes along the [100] and [010] direction. The uniaxial term stems from the bonds of the Fe/GaAs(001) interface and has a positive value,

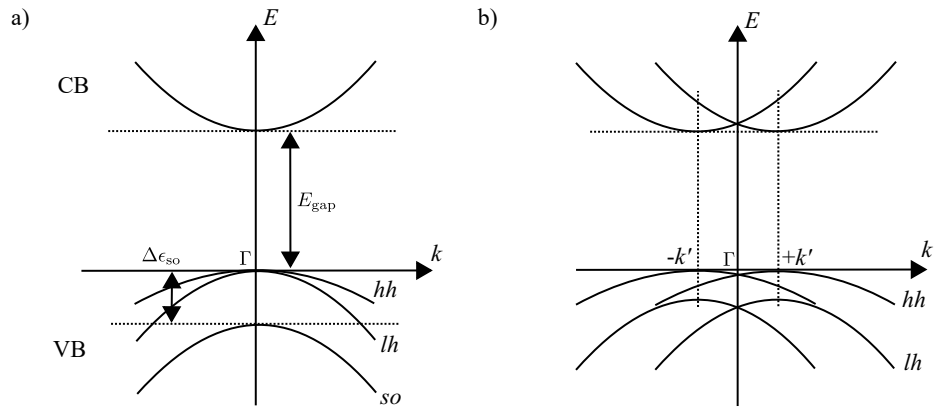

Figure 2.3: a) The band structure of a III-V semiconductor shows a fundamental gap between conduction and valence band. b) The spin-orbit interaction leads to band-splitting with $\Delta\epsilon_{SO}$ and the subbands are shifted by $\pm k$' due to the Rashba field (replotted from [1]).

which favors an easy axis along the [110] orientation [52, 53]. The interplay between both anisotropies depends strongly on the film thickness. For a 3.5 nm thin Fe film, the uniaxial anisotropy dominates the four-fold contribution by a factor of about two, which increases for thinner samples, since it originates from the interface.

2.4.2 Bychkov-Rashba effect

The band structure of a III-V semiconductor, as GaAs(001), is sketched in Fig. 2.3. Panel (a) shows the s-type (conduction band (cb), atomic orbital momentum $l = 0$) and p-type (valence band (vb), $l = 1$) energy bands. The spin-orbit interaction lifts the three-fold valence band degeneracy into a two-fold generated light (lh) and heavy hole (hh) band and a split-off band (so). The arising energy gap $\Delta\epsilon_{so}$ is about $\Delta\epsilon_{so} \approx 0.3$ eV for GaAs [54].

A confinement of electrons, e.g. along the growth direction, leads to a quantization, which lifts the degeneracy of the lh/hh bands, see panel (b). Further, the structure inversion asymmetry from the GaAs(001) zinc-blende structure induces a spin-splitting of the subbands by $-\Delta\mathbf{k}$ and $+\Delta\mathbf{k}$ with respect to $\mathbf{k} = 0$. The effect is called Bychkov-Rashba effect (BR) when spin currents are involved. In the 2D GaAs(001) system, this effect is caused by an asymmetric spin relaxation in a system with lifted spin degeneracy due to $\mathbf{k}$-linear terms in the Hamiltonian [55].

The microscopic origin of the Rashba effect can be explained by the movement of a electron with momentum in an electrical potential of a nucleus [1]. With relativistic corrections, the electric field is transformed into an effective magnetic field acting on the spin of the electron via the spin-orbit coupling. If the crystal has broken inversion symmetry, the conduction electrons will expe-

rience a net electric field perpendicular to the interface. The Rashba field is related to an asymmetric crystal field potential V of either the interface (SIA), and the Dresselhaus field to the crystal itself (BIA) [56]. A moving electron in the electric field of this potential feels a magnetic field

$$\mathbf{B}_{\mathrm{SO,R}} = -\frac{\hbar}{2m_e c^2}\mathbf{k} \times \mathbf{E}. \tag{2.26}$$

It was shown by Vasko [57], Aronov [42] and Edelstein [41] that a charge current in presence of Rashba Hamiltonian leads to spin polarization of the conduction electrons in semiconductor [55]. In bulk material with the SHE, the spin accumulation builds up directly at the interface between semiconductor and ferromagnet leading to a coupling of spin accumulation and magnetization generating a torque on **m**.

The Rashba field gives rise to three types of spin-splittings with different broken symmetries. The first type is the formerly explained Bychkov-Rashba spin-splitting which is predicted for crystals with one high-symmetry axis [58]. This effect is studied mostly in 2D semiconductor heterostructures where the electrons are confined to the xy-plane [45, 56]. The field term $H_{\mathrm{SO}}^{\mathrm{SIA}}$ in Eq. (2.24) is given by

$$H_{\mathrm{BR}} = \alpha_{\mathrm{BR}}(\hat{\boldsymbol{z}} \times \mathbf{k}) \cdot \boldsymbol{\sigma} \tag{2.27}$$

with the Rashba coefficient α_{BR}, the electron wave vector $\mathbf{k}$, the Pauli spin matrix $\boldsymbol{\sigma}$ and the growth direction $\hat{\boldsymbol{z}}$, which breaks the symmetry. The so-called Dresselhaus term links to the bulk inversion asymmetry in bulk zinc-blende crystals. For 2D GaAs(001) system, the Dresselhaus field is proportional to k and k^3 [59] and reads

$$H_{\mathrm{D}} = \beta \left[\sigma_x k_x (k_y^2 - k_z^2) + \sigma_y k_y (k_z^2 - k_x^2) + \sigma_z k_z (k_x^2 - k_y^2)\right] \tag{2.28}$$

with β as the strength parameter. The last contribution is present at interfaces with different types of atoms and is called the interface inversion asymmetry

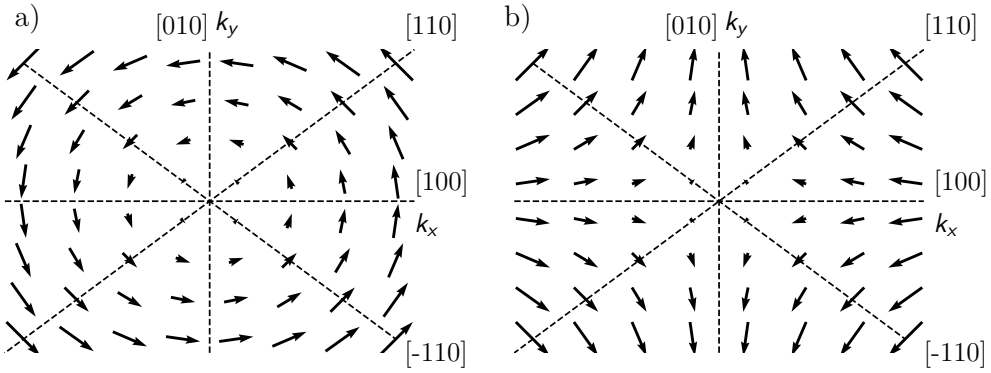

Figure 2.4: The Bychkov-Rashba (a) and Dresselhaus (b) spin-orbit fields are plotted as vector fields with respect to the two in-plane components $k_{x,y}$ of the wave vector and the crystallographic axes of GaAs(001).

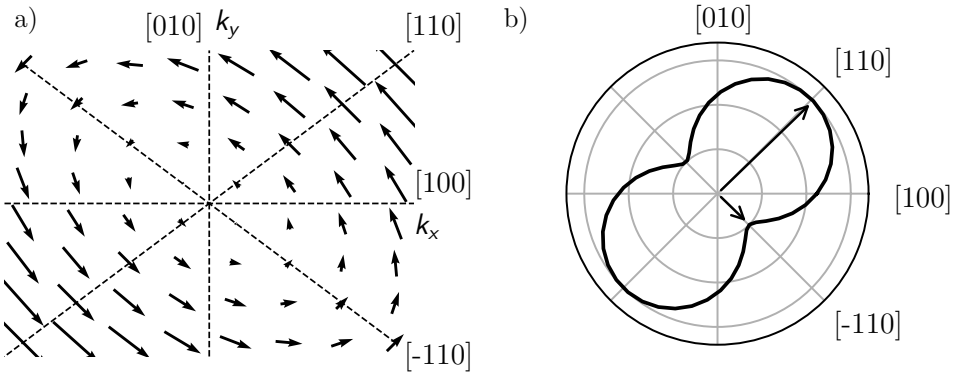

Figure 2.5: The combination of both fields shows a uniaxial anisotropy in terms of a vector field plot (a) and polar plot (b), where the Bychkov-Rashba is assumed to be twice as large as the Dresselhaus term.

(IIA) [60]. The IIA causes additional **k**-linear terms, which can be related to the bulk inversion asymmetry due to the same phenomenological behavior.

Fig. 2.4 plots the Bychkov-Rashba and Dresselhaus fields as vector fields and as a function of the two in-plane wave vectors $k_{x,y}$. While the spin Hall effect generates a pure spin current and causes a spin accumulation at the edges, the Rashba effect generates a spin accumulation at the interface. The Rashba effect can only be present in gyrotropic media[2] resulting in a non-zero average spin polarization [61] by a Rashba or Dresselhaus spin splitting of bands in a gyrotropic media due to a dc-current [55].

2.4.3 Spin-orbit fields and torques

The resulting spin polarization depend on the strength of both structure and bulk inversion asymmetry which induces a uniaxial anisotropy. A Zeeman-like effective term can be derived from the combined Dresselhaus and Bychkov-Rashba field as

$$\mathbf{B}_{\text{eff}}(\mathbf{k}) = \frac{1}{\mu_{\text{B}}} \begin{pmatrix} \beta k_x - \alpha_{\text{BR}} k_y \\ \alpha_{\text{BR}} k_x - \beta k_y \end{pmatrix} \tag{2.29}$$

with the corresponding strength parameter.

The superposition of both fields is visualized in Fig. 2.5(a) where a two times larger Rashba contribution is assumed. A two-fold symmetry of the spin-splitting energy can be found where the dominating part is oriented along the [110] direction for a Fe/GaAs(001) system. This originates from the superposition of both BIA and SIA, which can be visualized as a C_{2v} point group.

The spin-splitting energy from the SOI is defined as $\Delta\epsilon_{\text{SO}} = 2\mu_{\text{B}}|\mathbf{B}_{\text{eff}}|$

[2]Materials with a space inversion asymmetry and a low symmetry, i.e. the class of C_{2v}-symmetry with Fe/GaAs interface.

where the magnitude is calculated to [1]

$$|\Delta\epsilon_{\mathrm{SO}}| = 2k_{\parallel}\sqrt{\alpha_{\mathrm{BR}}^2 + \beta^2 + 2\alpha_{\mathrm{BR}}\beta\sin(2\phi_k)}, \tag{2.30}$$

with an in-plane wave vector $k_{\parallel}$ with $k_x = k_{\parallel}\cos(\phi)$ and $k_y = k_{\parallel}\sin(\phi)$. Fig. 2.5(b) depicts the magnitude of the SOC in a polar plot.

The anisotropy axis can be flipped by tuning the Bychkov-Rashba parameter via a gate voltage or an electron density in a 2DEGs [62] or Fe/GaAs/Au heterojunctions [63]. Furthermore, both interactions can be adjusted in order to cancel out along certain crystallographic directions, which gives rise to interesting effects, i.e. the vanishing spin-splitting in certain $\mathbf{k}$ directions [64], the lack of Shubnikov-de-Haas oscillations [65], the absence of spin relaxation [66] and the non-ballistic field-electron transistor [67]. Nevertheless, it is crucial to be able to disentangle both contributions which was done in experiments using the spin galvanic effect [68] and spin-splitting in quantum wells [69].

The previous introduced fields can act as torques on the magnetization in the FM layer, which is discussed in the following. The torque from the Rashba effect can be calculated to [70, 71]

$$\mathbf{T}_{\mathrm{BR}} = \frac{m\Delta_{\mathrm{ex}}}{e\hbar E_{\mathrm{F}}}\alpha_{\mathrm{BR}}\mathbf{m}\times(\hat{\mathbf{z}}\times\mathbf{m}), \tag{2.31}$$

where the exchange energy $\Delta_{\mathrm{ex}} = J_{\mathrm{ex}}\hbar M_{\mathrm{S}}/(2\gamma)$ is introduced with the exchange coupling J_{ex} between spin and magnetization, and Fermi energy E_{F}. This torque can be inserted into the LLG equation, where it acts on the magnetization like a magnetic field

$$\mu_0\mathbf{H}_{\mathrm{BR}} = \frac{\alpha_{\mathrm{BR}}}{2\mu_{\mathrm{B}}M_{\mathrm{S}}}P(\hat{\mathbf{z}}\times\mathbf{j}_{\mathrm{c}}) \tag{2.32}$$

with the spin polarization $P = \Delta_{\mathrm{ex}}/E_{\mathrm{F}}$ [26, 56]. This field is proportional to the applied current and is important for thin films since it scales inversely with the film thickness. Finally, the field-like torque can be written as

$$\mathbf{T}_{\mathrm{FL,BR}} = -\gamma\tau_{\mathrm{FL,R}}\mathbf{m}\times\boldsymbol{\sigma}_{\mathrm{FL,BR}} \tag{2.33}$$

with the torque strength

$$\tau_{\mathrm{FL,R}} = -\frac{\alpha_{\mathrm{BR}}P}{2\mu_{\mathrm{B}}M_{\mathrm{S}}}j_c \tag{2.34}$$

and spin polarization $\boldsymbol{\sigma}_{\mathrm{FL,BR}} = \hat{y}$ perpendicular to a charge current in x-direction.

2.5 Magnetization dynamics - ferromagnetic resonance (FMR)

This section treats the temporal evolution of the magnetization when it is driven out of the equilibrium position $\mathbf{m}_{\mathrm{eq}}$ by an external applied magnetic driving

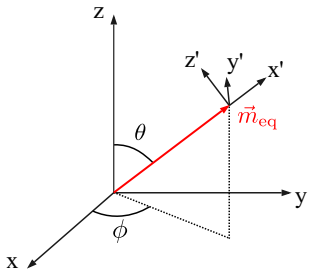

Figure 2.6: Used measurement system (x, y, z) is transferred to a new coordinate system (x', y', z') where the equilibrium magnetization is oriented along $\mathbf{m}_{eq} = (x', 0, 0)$ in order to calculate the magnetization dynamics.

field $\mathbf{h}_{rf}(t)$. The precession of $\mathbf{m}$ in a resonant manner on a cone around a stable equilibrium position $\mathbf{m}_{eq}$ is called ferromagnetic resonance (FMR). The response is linear for small deflections from $\mathbf{m}_{eq}$ and thus, the amplitude is directly proportional to the driving torque strength [72]. At the resonance frequency of the system, the internal frequency of the magnetic moments fulfill the FMR condition and the precession amplitude becomes maximal.

In experiments, the equilibrium condition $\mathbf{m}_{eq} \parallel H_{eff}$ is perturbed by a periodic excitation via a small, time varying magnetic field $\mathbf{h}_{rf}(t)$. This field exerts a torque on the magnetization which tilts $\mathbf{m}$ away from the effective field ($\mathbf{m} \nparallel \mathbf{H}_{eff}$) into a precessional motion. In addition, an external static field H_{ext} is applied in order to tune the magnetic stiffness of the system. Thereby, the resonance frequency of the system changes within the GHz range. FMR occurs at a certain magnetic resonance field H_{res} when both driving and resonance frequency coincide. There, the precessional amplitude becomes maximal. The FMR technique is often used to determine magnetic properties, as for example the effective magnetization M_{eff} and the Gilbert damping parameter α. Notably, a large magneto-crystalline anisotropy, i.e. for iron, changes the magnitude of the resonance field along the different crystallographic axes. Therefore, the FMR technique is also used to derive the anisotropy constants.

The linearized Landau-Lifschitz-Gilbert equation from Eq. (2.7) can be solved around the equilibrium magnetization position by assuming only small deviations expanding the damping term. This procedure was derived in detail by Obstbaum and Decker [27, 37], thus only the most important steps are displayed in the following.

All contributing fields, acting as torques on the magnetization, have to be divided into static and dynamic contributions while each of them can be splitted into a field- and damping-like term. First, the equilibrium position $\mathbf{m}_{eq}$ has to be found and expressed in the azimuth angle ϕ and the polar angle θ to

$$\mathbf{m}_{eq} = \begin{pmatrix} \sin(\theta)\cos(\phi) \\ \sin(\theta)\sin(\phi) \\ \cos(\theta). \end{pmatrix} \tag{2.35}$$

Fig. 2.6 sketches a second coordinate system (x',y',z') in order to apply for $\mathbf{m}_{eq} = \hat{x}'$. The magnetization can be split up into a static and dynamic part

as

$$\mathbf{m}(t) = \mathbf{m}_{\mathrm{eq}} + \Delta\mathbf{m}(t) = \begin{pmatrix} 1 \\ \Delta m_{y'}(t) \\ \Delta m_{z'}(t), \end{pmatrix} \tag{2.36}$$

where the magnetization is precessing around $\mathbf{m}_{\mathrm{eq}}$ in the $y'z'$-plane. Notably, there is no dynamic part along x' and the change of $\Delta\mathbf{m}$ is perpendicular to $\mathbf{m}_{\mathrm{eq}}$. All contributing fields have to be transformed into the local coordinate system with respect to ϕ and θ.

The result from a complex exponential ansatz $\Delta\mathbf{m}(t) = \Delta\mathbf{m}e^{i\omega t}$ is linearized by discarding higher-order terms. The solution is a set of two equations which can be written in terms of matrix elements with the dynamic susceptibilities:

$$\begin{pmatrix} \Delta m_{y'}(t) \\ \Delta m_{z'}(t) \end{pmatrix} = \begin{pmatrix} \chi_{y'y'} & \chi_{y'z'} \\ \chi_{z'y'} & \chi_{z'z'} \end{pmatrix} \cdot \begin{pmatrix} w_{y'} \\ w_{z'} \end{pmatrix}. \tag{2.37}$$

Here, the in-plane $w_{y'} = (h_{y'} - \tau_{\mathrm{DL}}/\mu_0\sigma_{z'})e^{i\omega t}$ and out-of-plane $w_{z'} = (h_{z'} - \tau_{\mathrm{DL}}/\mu_0\sigma_{y'})e^{i\omega t}$ driving torques summarize the driving fields with the field-like SOT and the damping-like SOT. Remarkably, $h_{y'}$ and $\sigma_{z'}$ act in the same manner on the magnetization due to the double cross product in the damping-like SOT. Thereby, a small rf damping-like torque can be substituted into an oop driving field [8].

A general form of the susceptibility matrix is given by [37]

$$\chi_f = \frac{1}{N_f} \begin{pmatrix} \mathcal{H}_0 + i\frac{\alpha\omega}{\mu_0\gamma} & i\frac{\alpha\omega}{\mu_0\gamma} \\ -i\frac{\alpha\omega}{\mu_0\gamma} & \mathcal{H}_1 + i\frac{\alpha\omega}{\mu_0\gamma} \end{pmatrix}, \tag{2.38}$$

$$N_f = \mathcal{H}_0\mathcal{H}_1 - (1+\alpha^2)\left(\frac{\omega}{\mu_0\gamma}\right)^2 + i(\mathcal{H}_0 + \mathcal{H}_1)\frac{\omega\alpha}{\mu_0\gamma}, \tag{2.39}$$

where each element of the susceptibility matrix is a complex number. Both parameters $\mathcal{H}_0$ and $\mathcal{H}_1$ are expressions from calculations of the different energy contributions and read as follows

$$\mathcal{H}_0 = H_{\mathrm{res}}\cos(\phi_M - \phi_H) + \mu_0 M_{\mathrm{S}} - H_{\mathrm{uni}}^{\perp} + \frac{H_{\mathrm{uni}}^{\parallel}}{2}\left[1 + \cos(2\phi_M)\right] + \\ + \frac{H_4^{\parallel}}{4}\left[3 + \cos(4\phi_M)\right], \tag{2.40}$$

$$\mathcal{H}_1 = H_{\mathrm{res}}\cos(\phi_M - \phi_H) + H_4^{\parallel}\cos(4\phi_M) + H_{\mathrm{uni}}^{\parallel}\cos\left(2\phi_M\right). \tag{2.41}$$

The term for the saturation magnetization $\mu_0 M_{\mathrm{S}}$ can be substituted by the so-called effective magnetization

$$\mu_0 M_{\mathrm{eff}} = \mu_0 M_{\mathrm{S}} - \frac{2K_{\mathrm{oop}}}{\mu_0 M_{\mathrm{S}}}, \tag{2.42}$$

since both demagnetization and out-of-plane anisotropy K_{oop} have the same dependence.

In the following, the simplest case is assumed without any spin-orbit torques or anisotropy fields. Thus, the two equations of Eq. (2.40) and (2.41) simplify to $\mathcal{H}_0 = H_{\mathrm{res}} + M_{\mathrm{eff}}$ and $\mathcal{H}_1 = H_{\mathrm{res}}$, respectively. The resonance condition is determined by setting the denominator N_f in Eq. (2.39) to zero. Thereby maximizing the susceptibility, the so-called Kittel formula

$$\left(\frac{\omega}{\gamma}\right)^2 = \sqrt{\mu_0 H_{\mathrm{res}} \cdot (\mu_0 H_{\mathrm{res}} + \mu_0 M_{\mathrm{eff}})} \tag{2.43}$$

is obtained. The effective magnetization can be determined by a frequency dependent measurement of the resonance position.

By adding the *ip* anisotropies and SOTs, it my happen that the external field is no longer aligned parallel along the equilibrium position. In other words, the two angles of magnetic field ϕ_H and magnetization ϕ_M differ with respect to the anisotropy energy. This issue is described by the dragging effect, which depends on the strength of the in-plane anisotropy and on the magnetic field amplitude. This dragging effect occurs always if the magnetic field is not aligned with the easy or hard axis. The susceptibilities can be expanded around the resonance field in terms of $\mathcal{H}_i = \mathcal{H}_i^{\mathrm{r}} + (H_{\mathrm{ext}} - H_{\mathrm{res}})$. Neglecting quadratic terms in α and using the simplified expressions of Eq. (2.40) and (2.41), the denominator from Eq. (2.39) can be rewritten to

$$N_f \approx N = (\mathcal{H}_0^{\mathrm{r}} + \mathcal{H}_1^{\mathrm{r}}) \left[(H_{\mathrm{ext}} - H_{\mathrm{res}}) + i \frac{\alpha\, \omega}{\mu_0 \gamma} \right]. \tag{2.44}$$

Thereby, the contribution from the damping-like SOT is included and a linewidth can be defined as $\Delta H = \alpha\omega/(\mu_0\gamma)$. The real part of the diagonal and off-diagonal susceptibility elements are obtained to ($H \equiv H_{\mathrm{ext}}$)

$$\begin{aligned}
\chi_{y'y'} &= \frac{\mathcal{H}_0^{\mathrm{r}}}{\Delta H(\mathcal{H}_0^{\mathrm{r}} + \mathcal{H}_1^{\mathrm{r}})} \frac{\Delta H(H - H_{\mathrm{res}}) - i(\Delta H)^2}{(H - H_{\mathrm{res}})^2 + (\Delta H)^2} = A_{y'y'} \left[F_{\mathrm{A}}(H) - i F_{\mathrm{S}}(H) \right], \\
\chi_{y'z'} &= \frac{\omega/\mu_0\gamma}{\Delta H(\mathcal{H}_0^{\mathrm{r}} + \mathcal{H}_1^{\mathrm{r}})} \frac{(\Delta H)^2 + i\Delta H(H - H_{\mathrm{res}})}{(H - H_{\mathrm{res}})^2 + (\Delta H)^2} = A_{y'z'} \left[F_{\mathrm{S}}(H) + i F_{\mathrm{A}}(H) \right],
\end{aligned} \tag{2.45}$$

which can be expressed by an amplitude A_i. The two symmetric and anti-symmetric Lorentzian functions are defined as

$$F_{\mathrm{S}}(H) = \frac{(\Delta H)^2}{(H - H_{\mathrm{res}})^2 + (\Delta H)^2}, \tag{2.46}$$

$$F_{\mathrm{A}}(H) = \frac{\Delta H(H - H_{\mathrm{res}})}{(H - H_{\mathrm{res}})^2 + (\Delta H)^2}. \tag{2.47}$$

The experimental data can be fitted with these two functions in order to extract the resonance field H_{res}, the linewidth ΔH[3] and the two amplitudes of the symmetric and anti-symmetric Lorentzian lineshape $F_{\mathrm{S,A}}(H)$.

[3] full width at half maximum of the Lorentzian curve

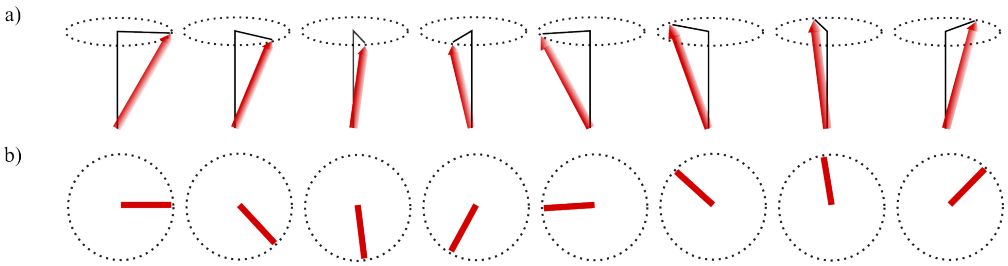

Figure 2.7: Top (a) and side view (b) of a spin wave as a one-dimensional chain of coupled magnetic moments (red arrows) with a finite phase lag between them.

2.6 Spin waves in thin ferromagnetic films

Up to now, only a homogeneous precession of $\mathbf{m}$ throughout the whole sample volume has been considered where magnetic moments precess at the same frequency and phase in a uniform mode. A higher-order excitation, however, forces the magnetization to precess at the same frequency but locally at slightly different phases. Fig. 2.7 sketches a propagating spin wave (SW) which can be modeled as a chain of coupled magnetic moments. The magnetization precesses around an equilibrium state and the phase from one to another moment shifts slightly.

The SWs have different properties depending on the relative orientation of wave vector and magnetization which are explained in this section. There are also different characteristics by means of the wave vector amplitude. The two extremes for a very small and a large wave vector magnitude are the dipolar and exchange dominated SWs, respectively.

2.6.1 Spin wave geometry and dispersion relation

The properties and amplitudes of SWs depend on the geometry of their propagation direction with respect to the static magnetization. Fig. 2.8 shows two in-plane magnetization geometries of a thin ferromagnetic film, which are characterized by the angle $\phi_{\mathbf{k}}$ between the wave vector $\mathbf{k}$ and the equilibrium magnetization $\mathbf{m}_{\mathrm{eq}}$. In the parallel configuration (a), $\phi_{\mathbf{k}} = 0°$, the propagation is along the magnetization direction and the SW is named backward volume wave (BV). At an angle of $\phi_{\mathbf{k}} = 90°$ (b), the wave is called Damon-Eshbach (DE) or surface wave.

Spin waves can be defined as collective excitations of magnetic moments with a finite phase to their next neighbors as mentioned above. The excitation can be described by a dispersion of angular frequency $\omega(\mathbf{k}) = 2\pi f(\mathbf{k})$ with a wave vector $\mathbf{k}$ which defines the propagation direction of the SW. The resulting wavelength is given by $\lambda = 2\pi/|\mathbf{k}|$. The dispersion relation for a thin film is described by $\mathbf{k}$ vectors in the film plane. In thicker films, an inhomogeneous magnetization profile along z causes an increase of exchange energy which favors

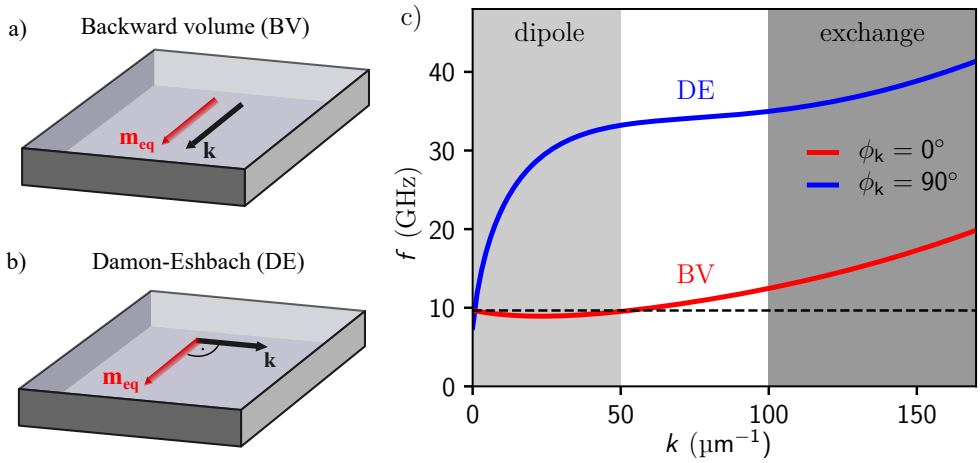

Figure 2.8: a, b) Two in-plane magnetized geometries where magnetization and **k**-vector are oriented parallel or perpendicular to each other. c) Without anisotropies, the dispersion relations are calculated for a 30 nm thick iron film with $\mu_0 H_{\text{ext}} = 50\,\text{mT}$, $\mu_0 M_S = 2.1\,\text{T}$ and $A = 13\,\text{pJ/m}$ where $\phi_{\mathbf{k}}$ denotes the angle between **m** and **k**. Two areas can be addressed depending on the magnitude of wave vector: dipole and exchange dominated regions correspond to small and large wave vectors, respectively.

perpendicular standing spin waves. These are created if the film thickness is larger than the exchange length

$$l_{\text{ex}} = \sqrt{\frac{2A}{\mu_0 M_S^2}}. \tag{2.48}$$

For the used ferromagnets in this thesis, the exchange length is about 5 nm for Py and 2.3 nm for Fe [73]. The thickness of the investigated films is in the range of l_{ex}, thus no perpendicular standing spin waves are neglected.

The solution of the LLG equation for an in-plane wave vector and a non-homogeneous demagnetization field must obey Maxwell's equations in the magneto-static limit with the usual electrodynamic boundary conditions. The general dispersion relation is derived for a thin film by assuming small wave vectors (dipolar dominated, $|\mathbf{k}| d_{\text{FM}} << 1$) and no anisotropy [74][4]:

$$\left(\frac{\omega}{\mu_0 \gamma}\right)^2 = \left(H_{\text{ext}} + l_{\text{ex}}^2 k^2 + M_S - \frac{M_S}{2} k d_{\text{FM}}\right) \cdot \left(H_{\text{ext}} + l_{\text{ex}}^2 k^2 + \frac{M_S}{2} k d_{\text{FM}} \sin^2(\phi_{\mathbf{k}})\right). \tag{2.49}$$

Notably, all wave vector related terms vanish for $k = 0$ and the Kittel formula is obtained as in Eq. (2.43). Fig. 2.8(c) shows the calculated dispersion relation for the two geometries over a wide range of wave vector amplitudes. The plot can be split into two regions: for very small **k** the dynamics are described by the weak,

[4] adapted from Kalinikos and Slavin [75]

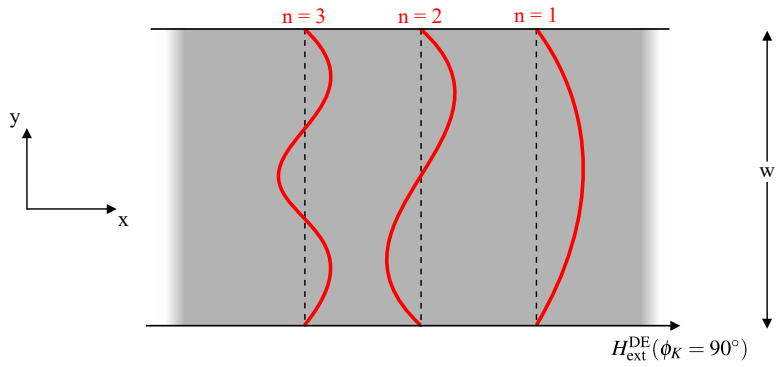

Figure 2.9: A lateral confinement due to a stripe generates standing spin waves along the y direction. In the DE geometry (the field along x direction) the first mode is highest in field and higher mode numbers decrease in distinct steps in terms of magnetic field. In the BV case all modes merge together due to the almost horizontal dispersion relation at $|\mathbf{k}| = 0$ and are displayed as a hatched area around the first mode.

long-ranged dipolar interaction since the terms with the exchange contribution are negligibly small. For large wave vectors, the quadratic dependence of the k^2 terms leads to a short-ranged, exchange dominated regime which is marked as a dark grey area in the figure.

Around $|\mathbf{k}| = 0$ the DE mode has a positive slope, which is caused by volume and surface demagnetizing fields. The BV branch has a negative slope and only exhibits surface demagnetizing fields. Both group $\nu_g = \partial\omega/\partial|\mathbf{k}|$ and phase $\nu_p = \omega/|\mathbf{k}|$ velocities depend on the geometry and either have equal or opposite signs for DE and BV case, respectively. This difference has a big impact on the following experiments [72]. There, only wave vectors of several μm^{-1} are present and thus dipolar dominated SWs are assumed in the following.

2.6.2 Lateral confinement

Before, spin waves were treated in thin ferromagnetic films, where they are only confined in the z direction. With better lithographic techniques, samples can be produced sufficiently small to get a lateral confinement in either 1D as stripes or 0D as dots. In the following, we will consider the formation of standing spin waves (SSWs) in a thin stripe.

The efficiency ϵ_{SW} to excite spin waves is proportional to the overlap integral of driving field h and mode profile q as [76]

$$\epsilon_{SW} \propto \int_0^{\frac{2\pi}{k}} dx\, h(x) q(x,k) \tag{2.50}$$

with $q(x,k) \propto \exp(i(\omega t - kx))$ for plane waves. In full films, the homogeneous driving fields create no propagating spin waves since the spin excitation efficiency is zero. Only inhomogeneous driving fields, caused by antenna structures for example, are able to excite such propagating SWs [77]. However, if a

homogeneous driving field is restricted due to a lateral confinement, it is also possible to excite standing spin waves [78]. Further, the modes can be separated in terms of magnetic field by reducing the width of the stripe, where higher modes shift towards lower magnetic fields.

In Fig. 2.9, the first three SSWs are sketched in an infinite long stripe as function of applied magnetic field. The spatial confinement in y causes a separation of modes under linear excitation in the film plane depending on the dimensions and orientation of the externally applied field [78]. This can be transferred to the former two geometries. In a longitudinally magnetized stripe (along the stripe axis, DE geometry), the lateral confinement results in a quantization of the in-plane wave vector perpendicular to the stripe in y direction. The first mode is highest in magnetic field and for increasing mode number the resonance field decreases. The modes are separated in field from each other by the same distance due to the almost linear dispersion for low wave vectors.

This is in contrast to SSWs in the backward volume geometry, where the slope of the dispersion relation is much lower and thus the modes are less separated. In addition, the magnetic field is inhomogeneous inside the stripe due to the static demagnetization field. The analytic expression of the internal field is given by

$$H_{\mathrm{int}} = H_{\mathrm{ext}} - \frac{\mu_0 M_{\mathrm{S}}}{\pi}\left[\arctan\left(\frac{d_{\mathrm{FM}}}{2y+\omega}\right) - \arctan\left(\frac{d_{\mathrm{FM}}}{2y-\omega}\right)\right], \tag{2.51}$$

which is maximal at the center of the stripe and reduces to zero at both edges [79]. There, the magnetization is not saturated which changes the spin wave eigenspectrum leading to a spin-wave barrier [80, 81]. This creates localized spin wave modes which are also called edge modes. Further, the negative dispersion relation in the low-k region, see Fig. 2.8(c) leads to a concentration of modes at roughly the same magnetic field position.

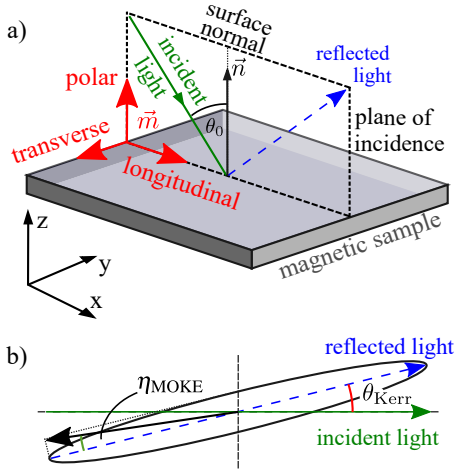

Figure 2.10: a) The three MOKE configurations depend on the orientation of the magnetization **m** with respect to the incident plane of the light: polar, longitudinal and transverse MOKE. b) The light is reflected from the FM surface at a complex Kerr angle for the longitudinal and polar MOKE. The polarization plane is rotated by the Kerr angle θ_{Kerr} and the beam receives an additional ellipticity η_{Kerr}.

2.7 Magneto-optical Kerr effect (MOKE)

In the experiments, the magnetization direction is detected optically by means of the magneto-optical Kerr effect (MOKE). It occurs when linearly polarized light is reflected from the surface of a magnetic material. Thereby, the polarization and/or intensity of the reflected beam can be changed. Fig. 2.10(a) depicts three possible configurations which can be categorized by the orientation of **m** with respect to the plane of incidence:

- polar MOKE (PMOKE): The magnetization points out-of-the film plane perpendicular to the sample surface. The polarization of the reflected beam gets rotated as well as gains an additional ellipticity, see panel (b).
- longitudinal MOKE (LMOKE): the magnetization is parallel to the plane of the incoming light and the surface normal. Therefore, this effect is used to determine the in-plane component of **m** and has also the same two effects on the reflected light as in the previous geometry.
- transverse MOKE (TMOKE): the magnetization is still parallel to the sample surface but lies perpendicular to the plane of incidence. This effect is the weakest of all three since no rotation of the polarization is involved in this case.

The magnitude of the effect depends on the angle θ_0 between the incident light direction and the surface normal. The incoming beam can be polarized parallel or perpendicular to the plane of incidence. Fig. 2.10(b) shows the characteristics of used PMOKE geometry which can expressed by a complex Kerr angle

$$\Theta^{\mathrm{Kerr}} = \theta_{\mathrm{Kerr}} + i \cdot \eta_{\mathrm{Kerr}} \tag{2.52}$$

with θ_{Kerr} as the Kerr rotation and η_{Kerr} as Kerr ellipticity or the ratio between semi-minor and -major axis. The complex Kerr angle is proportional to the magnetization and changes sign if the direction of **m** switches.

The microscopic origin of this effect lies in the occurrence of both exchange splitting and spin-orbit coupling and can be calculated by perturbation theory [82]. A linearly polarized light can be regarded as a combination of right and left circularly polarized light. In a magnetized medium, the refractive index of a left- and right-circular polarized light is different. Entering the medium, the linear polarized light is decomposed and gains a shift in the rotation of the polarization plane proportional to the refractive indices and sample thickness.

3

Experimental techniques

The third chapter introduces the two experimental techniques which are used to determine the spin-orbit fields and the spin Hall angle. The precession of the magnetization in a thin stripe can be detected electrically by means of the rectified dc-voltage or optically with MOKE. First, the process of sample fabrication is explained together with the basic principle of the excitation of the magnetization in the FM layer with a rf-driving field. Then, the electrical method is introduced along with the routine of data acquisition and the measurement setup. Next, the optical laser system is introduced where the magnetization is probed by short laser pulses. The standing spin wave geometries are discussed in the two geometries, where the lateral profile of the mode is investigated. Further, the fundamentals of the micromagnetic simulations are introduced, which are used to determine the spin-orbit fields by comparing the simulated mode pattern with the optically obtained results. Finally, the bolometric current calibration is displayed, which is very useful to determine the current flow in the FM stripe properly.

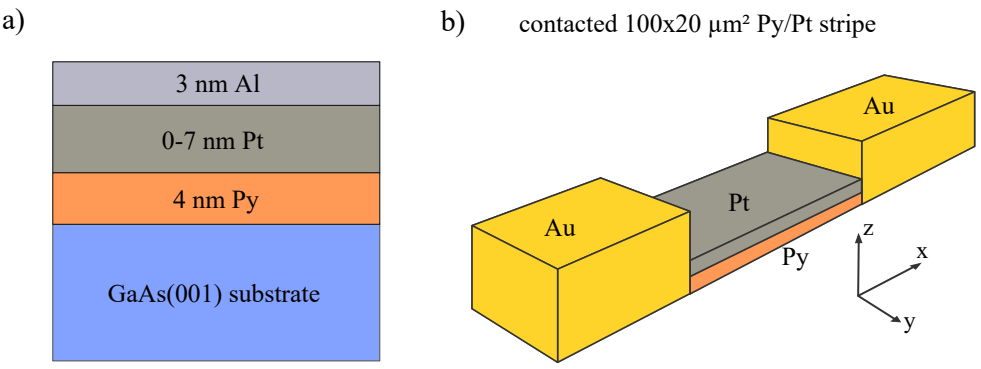

Figure 3.1: a) The MBE-grown stack of a Py/Pt bilayer is sketched with the varying platinum thickness on a fixed Py layer of 4 nm. The stack is sealed by aluminiumoxid to prevent the FM from oxidation. b) The geometry for current-induced excitation is the following: a patterned stripe (by EBL) is etched into the surface and contacted by two Au bondpads on both ends for injecting a rf-current.

3.1 Layer growth and sample fabrication

Both material systems in this thesis have the same GaAs(001) substrate in common, where a Py/Pt bilayer or a Fe film is grown onto the semiconductor. All layers are grown on the prepared substrate in a molecular beam epitaxy (MBE) chamber by Matthias Kronseder at room temperature. Fig. 3.1(a) sketches the first wafer, which consists of a 4 nm thick Py film below a series of different platinum layers ranging from 0 to 8.4 nm. The second stack, see panel (b),

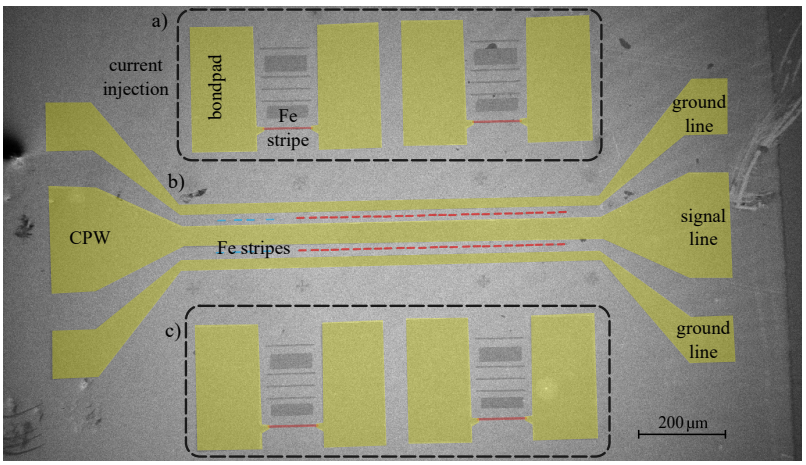

Figure 3.2: The two basic geometries are patterned next to each other on a piece of Fe/GaAs(001) wafer along the crystallographic [100] axis: a, c) four SOT-FMR devices, where one of five Fe stripes is connected to two large bondpads at both sides to directly inject a rf-current. b) Here, a co-planar waveguide (CPW), where Fe (red) and Py (blue) stripes are placed in the gap between the signal and two ground lines of the CPW.

contains a 3.5 nm thin Fe film on several tens of nanometers of a GaAs buffer layer, which is produced in a III-V MBE system without breaking the ultra-high vacuum. Finally, a 3 nm thin aluminum layer oxidizes under ambient conditions and therefore prevents all layers from oxidization.

Fig. 3.2 visualizes the two main geometries in SEM images with a colored overlay: a co-planar waveguide[1] (CPW) and a SOT-FMR design for direct current injection. The devices are fabricated in several steps out of the wafer by means of electron beam lithography[2] (EBL) with dimensions down to about a hundred of nanometers.

There are two kinds of resists depending on the development process: the exposed parts, written by EBL on a positive resist, becomes solvable to a developer liquid and second, a negative resist which strengthens the written areas and removes the unexposed part. For both types of devices, the FM stripe has first to be carved out of the wafer. In the first step, a $5\times5\,\mathrm{mm}^2$ piece of the wafer is covered by a negative resist and thinned down to several hundred nanometers thickness by fast rotation on a spin coater. The favored magnetic structure is then written by an electron beam into a positive resist and remains after the development. The resist protects the FM layer from ion beam etching using Ar^+ ions. The uncovered areas of the wafer are removed down to the GaAs substrate. The dimensions of the stripe vary between different material systems: rectangles of $100\times20\,\mu\mathrm{m}^2$ are used in the Py/Pt measurements in contrast to stripes of only $20\times2.8\,\mu\mathrm{m}^2$ in case of the Fe/GaAs samples. In the second step, two pads of about $400\times150\,\mu\mathrm{m}^2$ for the current injection or a co-planar waveguide are written by using two layers of positive resist to achieve proper edges. The CPW consists of a 50 µm wide signal line in the center and two ground lines of 30 µm, which are separated by a gap of 25 µm. The dimensions are tuned such that the impedance matches 50 Ω. After developing, the wafer is covered with 10 nm Ti and 140 nm Au in an evaporation chamber. The covered resist can be dissolved by acetone and the remaining current parts remain on the sample. In addition, small $10\times1\,\mu\mathrm{m}^2$ stripes of Py can be added in a third EBL step if necessary for the experiment.

3.2 Electrical detection technique

This section deals with the electrical approach to quantify the precession amplitude of the magnetization. First, the basic concept and the setup is explained together with the excitation by the driving field, which is also used later for the optical method. In the experiments, thin films or micrometer sized devices, made out of Fe/GaAs and Py/Pt, are measured by full-film, ST- or SOT-FMR

[1] It consists of three lines separated by two gaps where the inner one is called signal line carrying a positive current at a certain time. The two outer lines are called ground line which both support the half of the current flow in the opposite direction.

[2] more details on the process of sample fabrication is given in [27, 37]

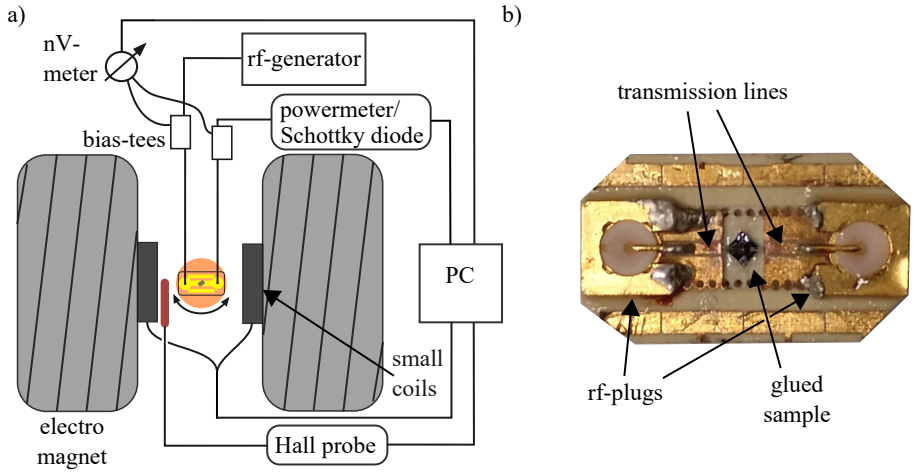

Figure 3.3: a) A simplified sketch of the main features of the electrical detection approach. The rf-current drives the magnetization and the transmitted rf-signal is measured at the end by a powermeter or a Schottky diode. Two large electromagnets provide a static magnetic field where two smaller coils with a 86 Hz field modulation for the lock-in technique are built-on. The induced dc-voltage can be picked up by two bias tees before and after the sample holder. b) Image of a sample holder with three transmission lines, two connection plugs and aluminum wires connecting the sample.

technique.

In order to detect the precession amplitude, three basic components are needed: a static magnetic field, a rf-driving field in the GHz range, which excites the magnetization and a measuring technique to detect it. Two basic ways to initiate a motion of the magnetization are carried out in this thesis, which are

- a microwave current flow through a co-planar waveguide (CPW), which generates a local rf-driving field h_{rf}. The following two possible designs are frequently used: first, the CPW is implemented in a chip carrier where a piece of FM wafer is placed on top. Or second, the CPW structure is patterned directly on the sample by EBL and a FM stripe is located in the gap. The transmissivity of the CPW is altered due to a coupling of the magnetization and the CPW which induces a current during FMR. The loss of transmitted signal is detected by a Schottky diode and relates directly to the precession amplitude.

- Passing a current through the device which directly drives the magnetization by a spin-transfer or spin-orbit torque. Thereby, a dc-voltage V_{dc} builds up due to rectification which can be measured by a nanovoltmeter. This is explained later in Sec. 3.2.4 in more detail.

3.2.1 Experimental setup

Fig. 3.3(a) sketches the basic setup of the electrical detection method. Two setups are used, one for room temperature measurements and the other for temperatures down to a few Kelvin.

In both cases, a rf-signal generator provides a current in the microwave frequency range between 2-18 GHz with an output power of 21 dBm. The rf-signal is guided through several wires and a bias tee to a rotatable sample holder, centered between the yoke of an electromagnet. Fig. 3.3(b) pictures the fabricated device which is glued on a sample holder. The rf-signal is fed with cables to the rf-plugs which is soldered on the chip carrier. The transmission lines are contacted by thin aluminum wires on the sample in order to transfer the rf-current through the FM layer. Another bias tee is inserted in the circuit, which detects the generated dc-voltage built up by the device. This signal is recorded by a nanovoltmeter while the external magnetic field is steadily increased at a fixed rf-frequency. At the end, a powermeter measures the transmitted power, which gives a total power loss through the setup with a calibrated power input. For a measurement of an unaffected film, the powermeter is substituted by a Schottky diode converting the transmitted ac-signal into a dc-voltage. The electromagnet creates a static in-plane field up to 300 mT and the field magnitude is measured continuously by a Hall sensor. Two additional small coils, attached to the inner parts of the yoke, create small fields up to two mT with a frequency of 86 Hz to enable lock-in technique.

3.2.2 Creation of the rf-driving field

A small driving field in the GHz regime is sufficient to bring the magnetization into a precessional motion and under certain conditions into ferromagnetic resonance. This field can be created in two different ways which is described in more detail in [27, 37]. The main results are presented in the following.

First by a CPW, which provides a wide range of frequencies combined with

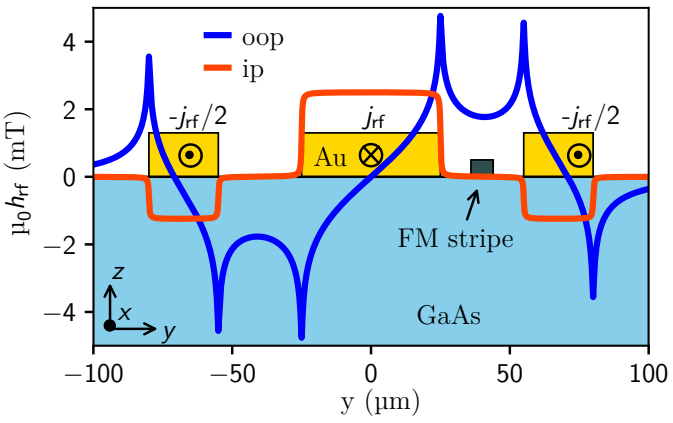

Figure 3.4: The rf-current through a CPW generates an Oersted field around it which can be decomposed into an in- and out-of-plane field. A FM stripe in the gap is only excited by a homogeneous *oop* driving field in the range of several mT.

a relatively low current density of about $j_{\mathrm{rf}} = 3 \cdot 10^9\,\mathrm{A/m^2}$. There, magnetic fields up to several mT are achieved with the used design of a 50 µm wide signal line and a gap of 25 µm. The current through the signal and ground lines create an Oersted field around the wires, which in turn can be calculated with Biot-Savart's law by assuming a homogeneous current distribution within the NM wire. Fig. 3.4 shows the cross section of the device with in- and out-of-plane generated Oersted fields. A FM stripe in the center of the gap is excited by a homogeneous *oop* field. The driving torque is always perpendicular to the *ip* external static magnetic field in this configuration. Thus, the torque is maximized since the precession angle between the magnetization and external field is largest during FMR. The cross product $\mathbf{m} \times \mathbf{H}_{\mathrm{ext}}$ is maximal and the magnetization has the largest precession angle.

The second approach is realized by passing a rf-current directly through the patterned stripe in another geometry, see Fig. 3.1b). The exact knowledge of the current magnitude in each layer is crucial for a proper data evaluation. In a Py/Pt bilayer, a resistor model [37] is used with Kirchhoff's law in order to calculate the current density of the Pt layer according to

$$j_{\mathrm{Pt}} = \frac{I}{w} \frac{\sigma_{\mathrm{Pt}}}{\sigma_{\mathrm{Pt}} d_{\mathrm{Pt}} + \sigma_{\mathrm{Py}} d_{\mathrm{Py}}} \tag{3.1}$$

with the conductivity σ, the stripe width w and the thickness of the individual layer d. This formula does not reflect the actual situation perfectly, since it neglects any skin effects and holds only for homogeneously magnetized samples. However, this simplification is only appropriate for a thin and low-conductance film in the range of several nm.

The generated Oersted field from the rf-current can be divided into an in- and out-of-plane component. The *ip* field across the wire in y direction splits up into two parts of the NM and FM layer. In the latter case, the Oersted field can be neglected if the FM thickness is in the order of the exchange length. Assuming a homogeneous magnetization distribution across the FM thickness, the created fields cancel out each other across the stripe. The *ip* Oersted field from the NM stripe can be calculated to

$$\mu_0 h^{\mathrm{ip}} = \frac{\mu_0}{2} j_{\mathrm{rf}}\, d_{\mathrm{NM}} \tag{3.2}$$

by assuming a much wider stripe width w than the NM thickness d_{NM}.

The z component of the Oersted field depends on the lateral stripe dimensions and is given by [11]

$$\mu_0 h_{\mathrm{rf}}^{\mathrm{oop}}(y) = -\frac{\mu_0}{2} \frac{I}{\pi w} \frac{\ln(y)}{\ln(w - x_0)} \quad x_0 \leq y \leq x_0 + w \tag{3.3}$$

with the position x_0 of one edge.

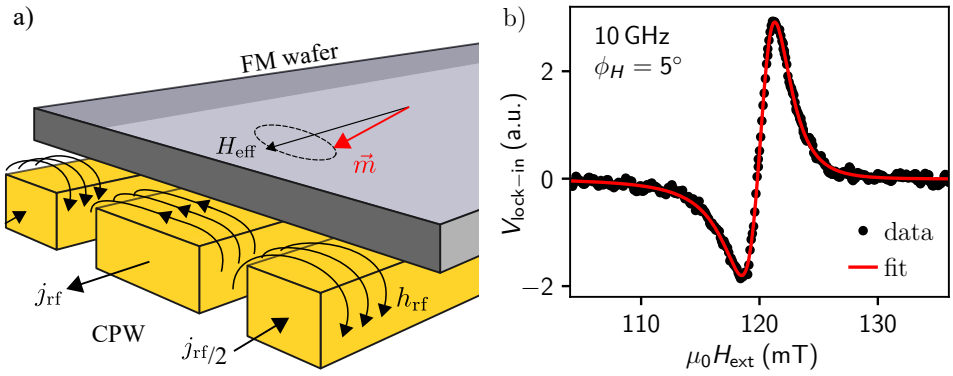

Figure 3.5: a) Sketch of the full-film FMR technique: a homogeneous driving field above the signal line of the CPW excites the magnetization in a ferromagnetic layer above. b) Typical lock-in signal measured for a full-film of 20 nm thick Py film at an excitation frequency of 10 GHz and a field angle of 5°. A resonance field of $\mu_0 H_{\text{res}} = 120.3\,\text{mT}$ and a linewidth of $\Delta H = 2.37\,\text{mT}$ is obtained by a fit with an anti-symmetric Lorentzian lineshape.

3.2.3 Full-film FMR characterization

FMR measurements on an unstructured piece of wafer (full-film) are a useful tool to check the magnetic properties and wafer quality before the lithography process is started. The technique provides an insight to the Gilbert damping parameter α, the gyromagnetic ratio γ and the effective magnetization M_{eff} of the FM layer.

A small piece of wafer is glued on top of a sample holder which is designed to act as a co-planar waveguide, see Fig. 3.5(a). Above the signal line, a homogeneous in-plane driving field is generated in order to excite the magnetization in the sample. The precessional motion of $\mathbf{m}$ undergoes ferromagnetic resonance at a certain external field strength while sweeping the external field at a fixed frequency of several GHz. The alternating magnetization leads to an inductive coupling into the signal line which reduces the transmitted power. The signal is converted into a dc-voltage by a Schottky diode and the signal magnitude is proportional to the absorbed rf-power during FMR and the magnetization precession angle. A small magnetic field with a frequency of 86 Hz modifies the external magnetic field and provides a reference signal for the lock-in technique. Fig. 3.5(b) shows the recorded voltage from the Schottky diode which can be well fitted by the derivative of a Lorentzian

$$V_{\text{lock-in}} = A\frac{-2(H_{\text{ext}} - H_{\text{res}})\Delta H\cos(\epsilon) + [(\Delta H)^2 - (H_{\text{ext}} - H_{\text{res}})^2]\sin(\epsilon)}{(H_{\text{ext}} - H_{\text{res}})^2 + (\Delta H)^2} \tag{3.4}$$

with an amplitude A and an additional phase ϵ [37]. The resonance field H_{res} and the linewidth ΔH as the full width at half maximum of the Lorentzian can be extracted from the fit of the anti-symmetric lineshape.

The gyromagnetic ratio γ and effective magnetization M_{eff} can be fitted by the Kittel formula introduced in Eq. (2.43) by repeating this for a series of different frequencies. The frequency dependence of ΔH scales linearly and the Gilbert damping parameter α can be derived by

$$\mu_0 \Delta H = \frac{\alpha \omega}{\gamma} + \mu_0 \Delta H_0 \tag{3.5}$$

with an additional offset ΔH_0 of the linewidth. This increase in linewidth is present throughout all frequencies, which indicates a broadening due to inhomogeneities in FM the layer or variations of M_{eff} within different grains [17].

Another purpose of the full-film FMR is the analysis of the anisotropy. This is achieved by changing the magnetic field angle ϕ_H for every magnetic field sweep. Thereby, the change of the resonance field during a full rotation can be used to determine the anisotropy constant. The recorded spectrum shifts by means of the resonance field H_{res} due to the anisotropy energy depending on the crystal axis of the FM layer. A polycrystalline Py film exhibits no preferred axis and thus shows an insignificant dependence of H_{res} on ϕ_H whereas an epitaxial, thin Fe film shows two pronounced easy and hard axes. Due to the anisotropy in iron, a larger field is needed to align the magnetization along the hard axis which results in a difference of $\Delta \mu_0 H_{\text{res}} = 130\,\text{mT}$ for a rf-frequency of 12 GHz between the easy and hard axis of a 3.5 nm thin iron film.

3.2.4 Voltage rectification

A second way to excite the magnetization is to use spin torques generated from a current through the device. This technique is called spin-transfer (ST-) or spin-orbit torque (SOT-)FMR depending on the origin of the spin-polarized current or spin accumulation, respectively. Both torques cause a precession of the magnetization which leads to a rectified dc-voltage along the device due to the mixing of high-frequency current and resistance. For example, the behavior of this voltage with respect to the frequency is useful to evaluate the charge-to-spin conversion efficiency or to determine the spin-orbit field by analyzing the magnetic field angle. Further, it is also used to understand the physics of the emerging materials [83].

In a Py/Pt bilayer, a rf-current I_x through a Pt wire causes a spin current in z direction into the Py layer which has a spin-polarization along the y direction. The spin current enters the Py layer and brings the magnetization into a precessional motion via damping- and field-like torques. In contrast, in the case of a Fe/GaAs(001) interface, a non-equilibrium spin accumulation is built up due to spin-orbit coupling at the interface. The spins diffuse through the boundary into the ferromagnet and exert damping- and field-like torques on the magnetization. Moreover, the current induces an Oersted field which contributes to the dynamics, however only as an antisymmetric *oop* field across

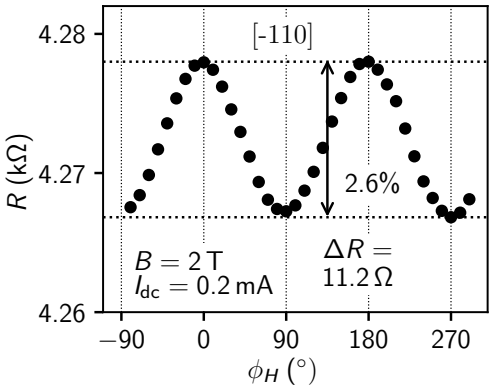

Figure 3.6: The angular dependence of the resistance is displayed for a dc-current of 0.2 mA along a [-110] patterned stripe at a magnetic field of 2 T. An AMR difference of 11.2 Ω (2.6%) is found between the [110] and [-110] direction.

the device [36]. All torques possess an oscillatory nature since driving frequency is the microwave regime.

The anisotropic-magneto resistance[3] (AMR) corresponds to a change of resistance when the angle between the current and magnetization of a bulk material is modified. For a parallel alignment, the resistance of a collinear configuration $\rho_{\parallel}$ is a few percent higher than for $\rho_{\perp}$, which is the perpendicular configuration. The maximal change between the two orientations is defined as

$$\Delta R = \frac{2(\rho_{\parallel} - \rho_{\perp})}{\rho_{\parallel} + \rho_{\perp}} \approx \frac{\rho_{\parallel} - \rho_{\perp}}{\rho_{\perp}}. \tag{3.6}$$

Fig. 3.6 shows the measured resistance for a full rotation of magnetic field at 2 T with a small, applied dc-current of 0.2 mA. A resistance difference of 11.8 Ω (2.6%) is observed for a 2.8 µm wide stripe of a 3.5 nm thin Fe film.

Next, the calculation of the rectified dc-voltage is discussed by regarding the rf-current and resistance of the stripe. The total resistance of the FM is given by

$$R(t) = R_0 + \Delta R \cos^2(\varphi_M(t)) \tag{3.7}$$

with the static, longitudinal resistance R_0 and the additional contribution due to AMR with the AMR coefficient $\Delta R = R_{\parallel} - R_{\perp}$ and the dynamic magnetization angle $\varphi_M = \sphericalangle(\mathbf{m}, \mathbf{I})$. In FMR experiments, the precessional motion of the magnetization results in time-varying angle $\varphi_M(t)$ between the current and the magnetization direction:

$$\varphi_M(t) = \sin(\phi_M + \theta_c(t)) \cos(\zeta(t)). \tag{3.8}$$

Here, the sine term contains the static magnetization angle ϕ_M defined by the in-plane effective field and the *ip* cone angle $\theta_c(t)$, which describes the deviation of the magnetization from the axis of rotation. The cosine terms denotes the *oop* component, which is can be neglected due to the large elliptical *ip* precession

[3]The AMR was first described in 1857 by William Thomson who recognized a change in the resistance of iron and nickel for different current to magnetization orientations [84].

is present since the equilibrium orientation of $\mathbf{m}$ is fixed in-plane due to the dominate *ip* applied external magnetic field [37]. For small cone angles, it is possible to expand $\cos^2(\phi_M)$ in a Taylor series up to the first order [85]. The time average voltage from Ohm's law is given by

$$< V(t) >= \Delta R < \theta_{\mathrm{c}}(t) I(t) > \sin(2\phi_M). \tag{3.9}$$

Notably, only the in-plane cone angle in the first order appears since thin FM films are treated where $\theta_{\mathrm{c}}(t) \gg \zeta(t)$. In the investigated system of Py and Fe, the *ip* cone angle can be expressed by [86]

$$\theta_{\mathrm{c}}(t) = \frac{\Delta m_{y'}(t)}{M_{\mathrm{S}}} \tag{3.10}$$

with the *ip* component $\Delta m_{y'}$ for small precession angles. Eq. 3.9 can be written by using the susceptibility tensor entries from Eq. (2.37). The driving fields and the current originate from the same microwave current source. Thus, they are oscillating with the same frequency ω as the precession frequency of the magnetization. Hence, by using the ansatz $I_{\mathrm{rf}}(t) = I_0 \cos(\omega t)$ and the real part of the susceptibilities, the voltage reads

$$< V(t) >= \frac{\Delta R}{M_{\mathrm{S}}} < \left[\mathfrak{Re}(\chi_{y'y'} w_{y'}(t)) + \mathfrak{Im}(\chi_{y'z'} w_{z'}(t))\right] I(t) > \sin(2\phi_M). \tag{3.11}$$

The imaginary part of $\chi_{y'z'}$ and the real part of $\chi_{y'y'}$ are already given in Eq. 2.45 as the function of the symmetric and anti-symmetric Lorentzian lineshape. The dc-voltage can be written as the sum of two Lorentzian functions

$$V_{\mathrm{dc}} = V_{\mathrm{S}} \cdot F_{\mathrm{S}}(H_{\mathrm{ext}}) + V_{\mathrm{A}} \cdot F_{\mathrm{A}}(H_{\mathrm{ext}}) \tag{3.12}$$

by using Eq. (2.47) with the corresponding amplitudes V_{S} and V_{A}.

3.2.5 Spin-transfer torque FMR (ST-FMR)

The ST-FMR provides a reliable and robust method to find the conversion efficiency of a charge into a spin current [36]. However, there are some material limitations and concerns due to the data evaluation led to controversial discussions in recent years.

It was shown previously that the symmetric amplitude of the Lorentzian in Eq. (3.12) is linked to the damping-like torque and is proportional to the spin current. The symmetric voltage can be written as [31, 87]

$$V_{\mathrm{S}} = \frac{\hbar j_{\mathrm{s}}}{2\mathrm{e}\mu_0 M_{\mathrm{S}} d_{\mathrm{Py}}} \tag{3.13}$$

with the spin current density j_{s} and thickness of the permalloy layer d_{Py}. The anti-symmetric voltage correlates with the generated Oersted field h_{rf} from the rf-current by

$$V_{\mathrm{A}} = h_{\mathrm{rf}} \sqrt{1 + \frac{\mu_0 M_{\mathrm{eff}}}{H_{\mathrm{res}}}} \tag{3.14}$$

with the effective magnetization M_{eff} and resonance field H_{res}. The field-like torque term can be neglected since it is very small for a Py/Pt bilayer [83]. The Oersted field is calculated with Ampere's law to $h_{\text{rf}} = j_{\text{rf}} d_{\text{Pt}}/2$. The charge current density j_{rf}, which is assumed to be only in the Pt layer, is homogeneous over the whole cross section, since there is no net in-plane Oersted field torque acting on the magnetization [36].

The material dependent spin Hall angle, proposed as the conversion efficiency, can be quantified by the ratio of the spin and charge current densities as [31]

$$\theta_{\text{SHA}} = \frac{j_{\text{s}}}{j_{\text{c}}} = \frac{V_{\text{S}}}{V_{\text{A}}} \frac{\text{e}\mu_0 M_{\text{S}} d_{\text{FM}} d_{\text{NM}}}{\hbar} \sqrt{1 + \frac{\mu_0 M_{\text{eff}}}{H_{\text{res}}}}. \tag{3.15}$$

For our sample, the saturation magnetization $\mu_0 M_{\text{S}}$ was determined by separate SQUID measurements. The effective magnetization M_{eff} is derived in a separate full-film FMR measurement. Both voltage amplitudes and the resonance field H_{res} are extracted by a fit from a single voltage spectrum with two Lorentzian lineshapes, see Eq. (3.12). This is repeated for a set of different microwave frequencies and magnetic field angles. This method is self-calibrated since the strength of the torque acting on $\mathbf{m}$ is measured with respect to the torque h_{rf}, which is easily calculated from current in the Pt layer [31].

However, this approach can be only used for materials without field-like torques. For a non-zero τ_{FL}, an additional anti-symmetric signal contributes to V_{A}, which would over- or underestimate the spin Hall angle. In the used Py/Pt bilayers, the spin Hall effect is assumed to originate only from the damping-like torque. In addition, another method is introduced later, which can resolve the damping- and field-like torques and quantify the spin Hall angle as well.

3.2.6 Spin-orbit torque FMR (SOT-FMR)

In a Fe/GaAs(001) system with non-zero field-like torque, the previously discussed simplification cannot be used. Instead, the spin-orbit fields can be quantified by evaluating the dependence of the symmetric and anti-symmetric voltage with respect to the magnetization angle ϕ_M. As explained earlier, C_{2v} symmetry at the interface induces a field-like contribution caused by the Bychkov-Rashba-like or Dresselhaus-like spin-orbit fields. Therefore, it is possible to determine the underlying SOT induced fields by using the same electrical measurement technique.

The rectified dc-voltage from Eq. (3.11) is discussed in more detail:

$$V_{\text{dc}} = -\frac{I \Delta R}{2 M_{\text{S}}} \sin(2\phi) \mathfrak{Re}(\Delta m_{y'}) \tag{3.16}$$

Here, the $-1 \cdot \sin(2\phi)$-term depends on the orientation of the stripe with respect to a crystallographic axis. From the GaAs the following four configuration are investigated: [100], [010], [110] and [-110]. These crystal orientations differ by

a change of sign ±1 as well as a sin/cos(2ϕ) dependence, which is shown later in more detail.

An expression of $\Delta m_{y'}$ can be obtained by solving the linearized equation from Eq. (2.37) and inserting the susceptibilities from Eq. (2.45) to get the following expression for the real part [8, 11]

$$\begin{aligned}\mathfrak{Re}(\Delta m_{y'}) =& \mathfrak{Re}(\chi_{y'y'}) \left[-h^{\mathrm{ip}}_{[100]}\sin(\phi_M) + h^{\mathrm{ip}}_{[010]}\cos(\phi_M)\right] - \\ & \mathfrak{Im}(\chi_{y'z'}) \left[-h^{\mathrm{oop}}_{[100]}\sin(\phi_M) + h^{\mathrm{oop}}_{[010]}\cos(\phi_M)\right]. \end{aligned} \tag{3.17}$$

Previously, the last term in Eq. (3.17) was only proposed by a single *oop* field, which does not perfectly reflect the experimentally observed behavior [88, 89]. Thus, the same combination of a sine and cosine contribution is used as in the in-plane case [12].

The first term in Eq. (3.17) contributes to the in-plane SOFs and leads to an anti-symmetric voltage via the real part of the diagonal susceptibility $\chi_{y'y'}$ [86]. In contrast, the second term is connected to the symmetric voltage and the imaginary part of the off-diagonal element $\chi_{y'z'}$. Both fields $h_{[100]}$ and $h_{[010]}$ denote the driving SOFs parallel and perpendicular to the patterned crystal axis and current direction.

The two fields are related to the general coordinate system as seen in Fig. 2.4. Note that, for stripes patterned along [100] and [010], the fields can be directly linked to the Bychkov-Rashba and Dresselhaus fields. For [110] and [-110] stripes, the Bychkov-Rashba and Dresselhaus SOFs are perpendicular to each other and their strength has to be calculated by trigonometry.

As an example, for a [100] oriented stripe, both voltages are given by [8]

$$V_{\mathrm{S}} = -V_{\mathrm{AMR}}\sin(2\phi_M)\mathfrak{Im}(\chi_{y'z'}) \left[-h^{\mathrm{oop}}_{[100]}\sin(\phi_M) + h^{\mathrm{oop}}_{[010]}\cos(\phi_M)\right], \tag{3.18}$$

$$V_{\mathrm{A}} = -V_{\mathrm{AMR}}\sin(2\phi_M)\mathfrak{Re}(\chi_{y'y'}) \left[-h^{\mathrm{ip}}_{[100]}\sin(\phi_M) + h^{\mathrm{ip}}_{[010]}\cos(\phi_M)\right], \tag{3.19}$$

with $V_{\mathrm{AMR}} = I\Delta R/(2M_{\mathrm{S}})$ as the AMR voltage. The SOFs can be determined by a fit of the voltage spectra with respect to the magnetization angle ϕ_M, where the symmetric and anti-symmetric magnitude $V_{\mathrm{S,A}}$ is extracted from a fit with a Lorentzian lineshape. The measurement is repeated at different magnetic field angles for a full rotation in steps of 5°. This results in a detailed angular dependence of the two voltage magnitudes, the resonance field and linewidth. Thereby, the magnetization angle ϕ_M and the susceptibilities $\chi_{y'y'}$ and $\chi_{y'z'}$ can be calculated which requires a detailed analysis of the resonance field and linewidth as a function of applied magnetic field angle ϕ_H. Finally, the resulting SOFs are obtained by fitting the normalized voltage with Eq. (3.18) and (3.19), separately.

3.2.7 Modulation of damping (MOD)

The following method is used in this thesis for a Py/Pt system to separate the damping- and field-like torques. In this case, the magnetization dynamics are

altered by an additional applied dc-current which leads to the injection of a pure spin current into Py via the SHE in Pt. The injected spin current modifies the effective damping depending on the polarity of the current [90]. The damping- and field-like torques can be quantified by analyzing the resonance field and linewidth of the Lorentzian lineshape.

The damping-like torque induces a shift in the linewidth ΔH to

$$\mu_0 \Delta H = \frac{2\pi f}{\gamma}\alpha + \frac{2\pi f}{\gamma}\frac{\sin(\phi_H)}{\mu_0(H_{\mathrm{ext}} + M_{\mathrm{eff}}/2)M_{\mathrm{S}}d_{\mathrm{Py}}}\frac{\hbar}{2\mathrm{e}}j_{\mathrm{c}}\theta_{\mathrm{SHA}}^{\mathrm{eff}}, \tag{3.20}$$

where the first term describes the linewidth at zero dc-current [31]. The second term accounts for the modulation of linewidth or damping, where the magnetic field angle ϕ_H and the product of current density in the Pt layer and spin Hall angle $\theta_{\mathrm{SHA}}^{\mathrm{eff}}$ are included. Eq. (3.20) is only valid if the anisotropy and the in-plane demagnetizating fields are negligibly small, which is the case for a Py/Pt stripe with dimensions of 100 µm×20 µm×4 nm.

The shift of linewidth due to the applied dc-current can be detected optically and electrically with the previously introduced TRMOKE and ST-FMR setups, respectively. In the latter, the rf-current is modulated by a kHz-signal in order to enable a lock-in technique. In the two approaches, the recorded FMR spectrum is fitted by a Lorentzian, where the linewidth is determined as reported above. This is repeated for different bias currents as well as for positive and negative magnetic fields.

3.3 Time-resolved magneto-optical Kerr effect microscope

The second measurement technique, used in this thesis is based on the optical detection of spin waves in nanostructures at room temperatures. The dynamics of the SWs are detected by a time-resolved magneto-optical Kerr microscope. A femtosecond laser system in combination with a microscope provides both spatial and temporal resolution to observe magnetization dynamics in the polar MOKE geometry. The principle as well as the two operation modes are discussed in the following.

Fig. 3.7 shows the Time-resolved magneto-optical Kerr effect microscope (TRMOKE) setup, which is divided into an optical and a microwave part. The sample is again glued on a sample holder, which is mounted on a piezo stage with a fine (nm) precision and a micrometer stage for a coarse (µm-mm) precision in all three dimensions. A pulse length much smaller than one single SW oscillation is required in order to resolve the SW dynamics, which is provided by a femtosecond laser system. A pumped Ti:Sapphire laser generates pulses at a wavelength of $\lambda_c \sim 800\,\mathrm{nm}$ and a pulse width of $\tau_w \sim 150\,\mathrm{fs}$. The pulse repetition rate is 80 MHz and thus the time between two pulses is $\Delta t =$

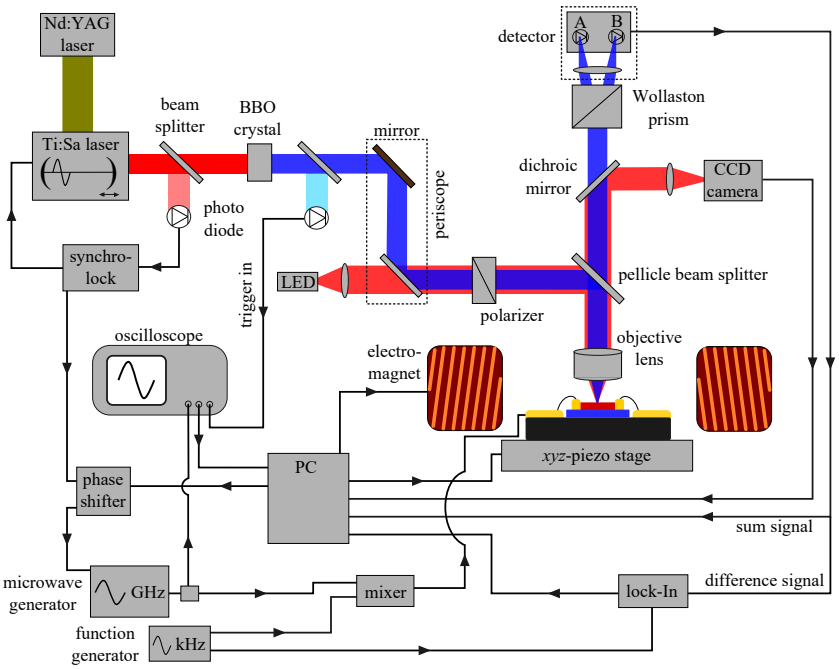

Figure 3.7: Sketch of the TRMOKE setup: a frequency doubled Ti:Sa laser pumped by a Nd:YAG laser emits pulses to probe the *oop* component of **m** at a distinct rf-to-laser phase ψ. A synchrolock between rf-generator and laser stabilizes the phase (replotted from [77]).

12.5 ns. This is enough to probe the magnetization at certain states given by

$$\tilde{t}_n = n \cdot \Delta t + t_0 \quad n \in \mathbb{N}^+, \tag{3.21}$$

with t_0 as an arbitrary offset in time. Apparently, at each time $\tilde{t}_n$ the out-of-plane magnetization is desired to be in the same state of the precession, which can be ensured by setting the rf-excitation frequency at a multiple of 80 MHz. Further, it requires a constant phase ψ between the excitation and detection. This is achieved by using a synchrolock. It locks the phase of the probing laser pulse with the microwave excitation.

The repetition rate is read out via an optical fibre connected to an internal photo diode and is stabilized by a computer. The signal is compared to an internal 80 MHz clock. If the signal differs from the internal 80 MHz clock, the length of Ti:Sapphire cavity can be adjusted by moving a mirror with the help of a piezo stage. The synchrolock also sends a 10 MHz reference signal to the rf-generator via an electronic phase shifter. The latter is used to change and stabilize the phase ψ between rf-current and laser pulse. This corresponds to a relative phase since the absolute phase is unknown due to the many components in the rf-circuit. The relative phase can be stabilized by a sampling oscilloscope which monitors the rf-signal. It is triggered by the laser pulses via a second fast laser diode. A computer processes the oscillations and fits a sine function

in order to determine the current phase ψ. If it is required, the phase will be changed by the phase shifter during a stabilizing process.

The optical beam path begins on the upper left side of Fig. 3.7 where a Nd:YAG laser with 10 W output power pumps an infrared Ti:Sapphire laser. The beam gets frequency doubled inside a barium borate oxid (BBO) crystal by means of second harmonic generation. Afterwards, it has a power of 100 mW at a wavelength of about 400 nm. A periscope enables a proper alignment of the microscope and the polarization is fixed along one axis by a polarizer. Then, the beam hits a pellicle at an angle of 45° where only 8% of the light is reflected to a 100x objective lens with a numerical aperture of NA=0.7. This provides a spatial resolution between $d_{\mathrm{min}} = \lambda/(2 \cdot \mathrm{NA}) \sim 285\,\mathrm{nm}$ and $\lambda \approx 400\,\mathrm{nm}$, which is in the order of the Abbe limit. The reflected beam, focused onto a FM surface, becomes elliptically polarized and rotated by the Kerr effect. The polar MOKE geometry, introduced in Sec. 2.7, is sensitive to the *oop* component of the magnetization.

The light propagates again through the same pellicle with 92% transmission and passes a dichroic mirror towards a Wollaston prism. There, the beam is split up into two orthogonally polarized beams, which are focused on two photo diodes. The light is converted into a photo voltage and amplified for further data processing by a lock-in. The detector unit outputs two voltages, namely the sum and difference of the two diodes. The sum signal is proportional to the local reflectivity of the sample surface and further called topography voltage V_{Topo}. The difference signal contains the magnetic information of m_z at the laser spot for a given phase ψ. Further, it is proportional to the Kerr angle and is denoted as V_{Kerr}. Both voltages are detected by a Zuerich Instruments lock-in with a phase-modulation of 6.6 kHz from a function wave generator. A second optical path is installed to monitor the sample through the same optical

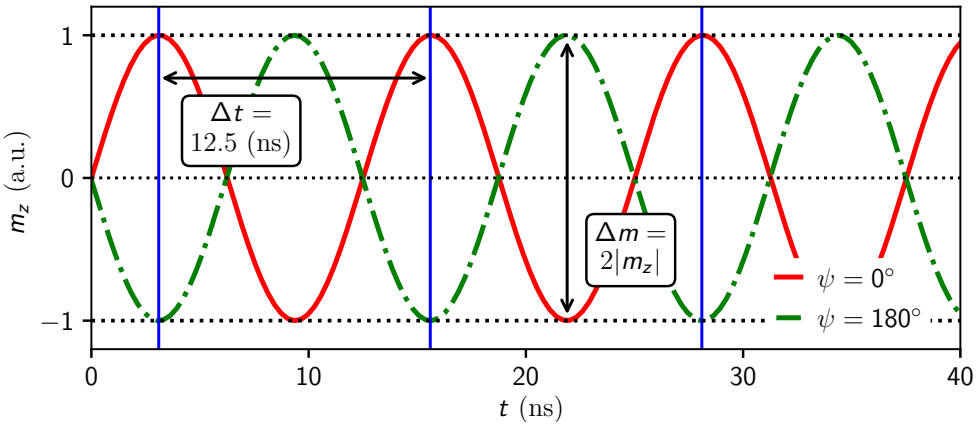

Figure 3.8: The stabilized phase of rf-excitation (red) is switched by 180° (green) at a low kHz-frequency in order to detect a signal proportional to $\Delta m = 2m_z$ via a lock-in. The blue lines indicate the laser pulses.

path. This is achieved by a red LED light which is coupled into the laser beam path by a dichroic mirror. The reflected light is then coupled out by a second mirror and captured by a CCD camera. The mirrors are only sensitive to the LED wavelength thus not disturbing the blue laser light.

The microwave part starts with a microwave generator providing a rf-signal in the GHz range with up to 24 dBm output power. Here, we make use of a 180° phase modulation at 6.6 kHz provided by a function generator and mixed with a microwave signal. The modulation of several kHz is quasi-statical compared to the GHz signal and the 80 MHz repetition rate of the laser. This situation is depicted in Fig. 3.8: the signal amplitude and consequently the signal-to-noise ratio is enhanced as compared to using a simple on/off modulation instead. The integration time of the lock-in is about several hundreds of milliseconds containing thousands of SW oscillations. An image stabilization process keeps the sample on the same position under the objective lens during the measurements and always focussed on the same spot. For this reason, a computer compares the live image with a reference image and moves the sample back with the help of the piezo stage in order to match the two images. An external magnetic field up to 400 mT can be applied in any in-plane direction.

3.4 Operation modes

For the SW detection, the TRMOKE setup supplies two operation modes revealing different insights: the SW spectroscopy and the SW imaging mode, which are discussed in detail in the following. In this section, the external field is always applied in the film plane and along the stripe in the DE geometry.

3.4.1 Spin wave spectroscopy

In the spectroscopy or static mode, the laser beam is focused on a single spot with the help of the piezo stage. Further, the rf-frequency, -phase and -power are kept constant during the complete measurement routine. Merely the magnetic

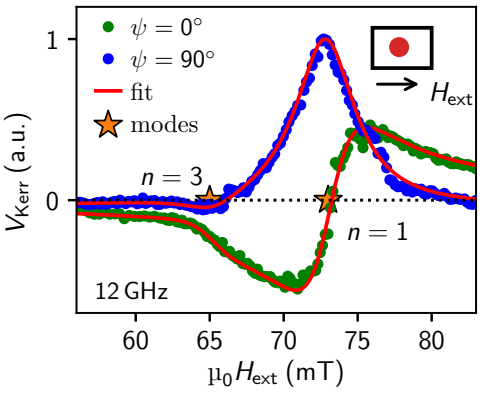

Figure 3.9: Spectroscopy mode of the TRMOKE setup: the Kerr signal of a 2.8 µm wide [110] stripe is recorded at a fixed rf-frequency of 12 GHz. This is done for a relative phase of $\psi = 0$ and 90° between laser and excitation while sweeping the external field. The data can be fitted by Lorentzian functions in order to find resonance position (orange stars) and linewidth of each mode.

field is swept at a constant rate while the Kerr signal V_{Kerr} is recorded.

Fig. 3.9 shows the resulting curves for two phases which are called SW resonance spectra. Here, two rf-excitation phases of $\psi = 0$ and 90° are displayed for a wide range of magnetic fields and the data is normalized to the highest amplitude. At fields near the resonance position of about 72 mT either a symmetric ($\psi = 0°$) or anti-symmetric ($\psi = 90°$) Lorentzian function appears and represents the FMR. The data shown in Fig. 3.9 is recorded from a Fe stripe in the gap of a CPW, which is driven by a homogeneous out-of-plane field. This adds a 90° shift to the phase due to the *oop* configuration and explains the anti-symmetric line shape at a phase of $\psi = 0°$ [27]. The data is well fitted by a Lorentzian function to determine the resonance field as well as the linewidth. Even a mode with mode number $n = 3$ can be resolved when the same linewidth is assumed in the fit function. The resonance field position of the individual modes allows the calculation of the magnetic field mode spacing. It depends on the ratio of stripe width to thickness and is crucial for the evaluation of modes. In conclusion, the resonance positions and mode spacing of standing spin waves can be found with this method.

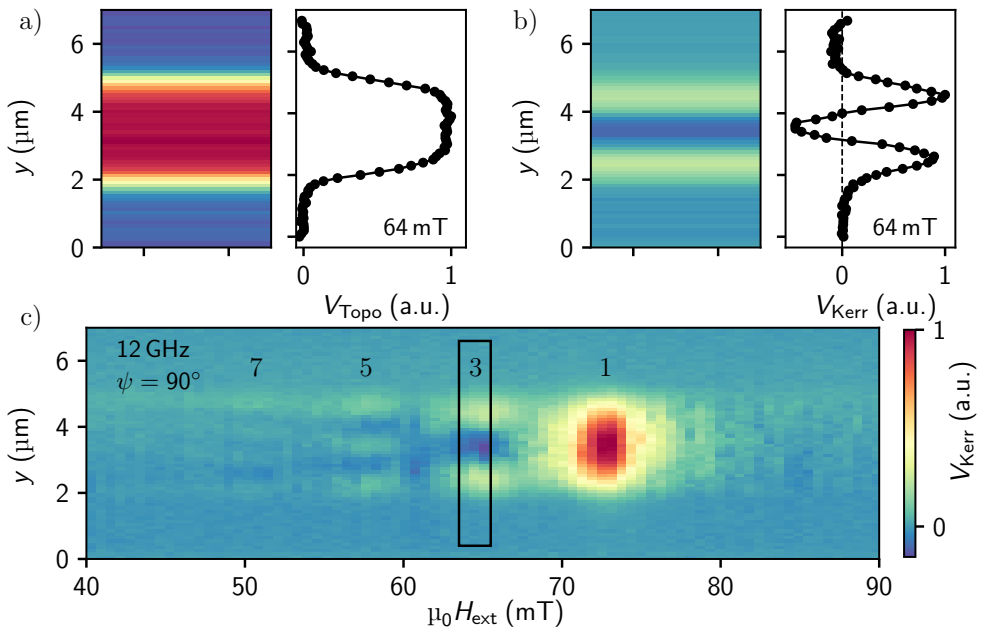

Figure 3.10: Sample data of the SW imaging mode: a) the sum signal shows the topographic signal or reflectivity of the sample whereas in b) the Kerr signal gives access to the *oop* magnetization at 64 mT field for $\psi = 90°$ at a frequency of 12 GHz. Repeating these scans for a wide range of fields, a 2D magnetization pattern is obtained as a function of lateral space coordinate and magnetic field as shown in c).

3.4.2 Spin wave imaging

The second operation mode is used for spin wave imaging where the microwave frequency, phase and power are fixed in addition to the external field. In contrast to the previous subsection, the sample is moved along the lateral y axis of the stripe with a step size of 100 nm by the piezo stage. Thereby, both voltages V_{Topo} and V_{Kerr} are recorded for every distinct spot with typical integration times of 300 ms.

Fig. 3.10(a) visualizes the topographic (Topo) signal of one line scan as a colored image on the left and as a stripe profile on the right panel. Thereby, it is possible to determine both edges of the stripe precisely by fitting the derivative of the topographic signal by a Gaussian function. Subplot (b) shows the Kerr signal at a field strength of 64 mT, where the third mode is located for this stripe direction. The magnetization shape clearly indicates two nodes and consequently the development of a standing wave with mode number $n = 3$. The line scan is repeated for a wide range of external fields in order to map the different dynamical features. By doing so, the Kerr signal line scans can be plotted versus the applied field to get the 2D mode pattern as seen in panel (c). This pattern reveals the spatial distribution of the dynamic *oop* magnetization as well as its field dependence. The maximum amplitude is found at around 72 mT where the first mode is located showing a large red area. Modes up to the seventh order are visible by a careful inspection of the pattern, since the magnetization is driven by a homogeneous out-of-plane field. Spin waves are therefore detectable in a large range of magnetic fields. In this thesis, this mode pattern is of great importance since all contributions from underlying fields enter the SW dynamics and leave a trace in the 2D magnetization image.

3.5 Confinement of spin waves

As discussed previously, a standing spin wave evolves due to a confinement in lateral dimensions. This results in a generation of even and odd modes which are characterized by a mode number n. These waves are treated by assuming a much larger stripe length than width. Two major cases are implied relating to the orientation of the applied magnetic field affecting the mode appearance. First, a field aligned parallel along the x axis (stripe's long axis) is called longitudinally magnetized and the SWs propagate in the Damon-Eshbach geometry. By contrast, in the perpendicular (backward volume) configuration, the stripe is transversally magnetized.

3.5.1 Longitudinally magnetized stripes

In the following, a stripe is discussed which is magnetized by an applied field along the x axis with a resulting field angle of $\phi_H = 0°$. In an infinitely long

stripe, no static demagnetization field occurs in this configuration and thus the equilibrium magnetization is fully saturated along x. Hence, this defines a 1D problem across the stripe width. The dispersion relation has to be taken for the Damon-Eshbach geometry which is given by Eq. (2.49) with $\phi_K = 90°$.

The eigenfunctions are either symmetric or anti-symmetric with respect to the cross section of the stripe and can be approximated by a cosine or sine function, respectively [91]. It has been shown by Bayer et al. [78] that a confinement leads to a discrete set of symmetric and anti-symmetric eigenmodes

$$q_n^{\mathrm{S}}(y) = A_n^{\mathrm{S}} \cos(k_n y) \quad q_n^{\mathrm{A}}(y) = A_n^{\mathrm{A}} \sin(k_n y) \tag{3.22}$$

$$k_n = \frac{n\pi}{w} \frac{d(p) - 2}{d(p)}, \quad d(p) = \frac{2\pi}{p(1 - 2\ln(p))}, \tag{3.23}$$

with the thickness-to-width ratio of the FM layer denoted as the parameter $p = d_{\mathrm{FM}}/w$. The eigenvalues are given by [78]

$$\lambda_n(p) = -4\pi + \pi^2 (2n - 1)\, p, \quad n \in \mathbb{N} \tag{3.24}$$

and the associated eigenfrequencies are

$$f_n = \frac{\gamma}{2\pi} \sqrt{\mu_0 H_{\mathrm{ext}} (\mu_0 H_{\mathrm{ext}} + \mu_0 M_{\mathrm{S}}) + \frac{\pi}{4} (\mu_0 M_{\mathrm{S}})^2 \frac{d_{\mathrm{FM}}}{w} (2n - 1)}, \quad n \in \mathbb{N}. \tag{3.25}$$

Comparing these eigenfrequencies with the Kittel formula from Eq. (2.43) reveals a shift of frequency by a factor depending on the mode number n and thickness-to-width ratio p. The first mode with mode number $n = 1$ lies lower in field as in the case for full-film FMR. If the magnetization is excited at a fixed frequency, the higher order modes will appear at smaller magnetic fields.

An important parameter is the previously introduced mode spacing, which is the difference between two neighboring modes in terms of magnetic field. This parameter depends solely on the width w for a fixed FM layer thickness. The ratio p is enhanced by reducing the stripe width and thus the distance between two modes is increased. For smaller p, the modes overlap and cannot be clearly separated. This behavior can be divided into three regimes of the mode spacing parameter p:

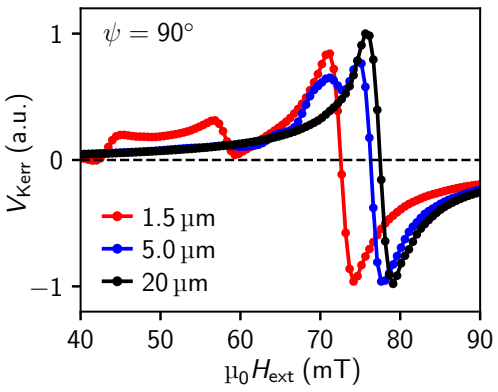

Figure 3.11: The impact of the stripe width on the magnetic field dependence is shown for a phase of $\psi = 90°$ for varying stripe widths between 1.5-20 µm. For a [110] patterned stripe, a simulation reveals the mode spacing as well as the shift towards lower field for narrow stripes.

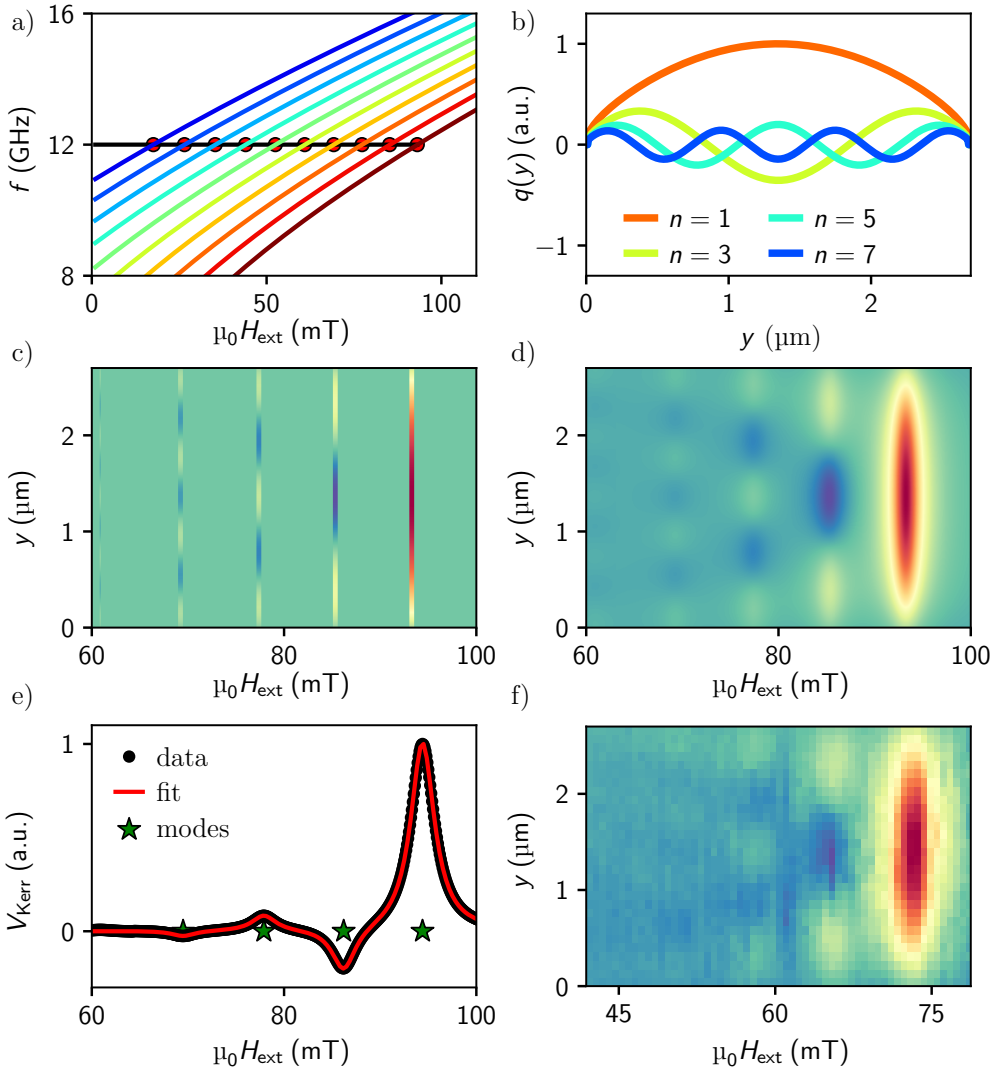

Figure 3.12: Numerical calculation of SSWs without anisotropy in a 3.5 nm thin and 2.8 µm wide longitudinally magnetized Fe stripe and comparison with measured TRMOKE data. a) Dispersion branches of different modes and points of intersection with a fixed frequency. b) First four mode profiles with odd mode numbers. c) Modes are put into an array to visualize their behavior in a (H,y) plane. d) Convolution with linewidth and probing spot size. Panel e) shows a cut along the middle of the stripe ($y \approx 1.5\,\mu m$) together with a fit to extract $H_{res,n}$ and ΔH. f) experimental data with anisotropy.

- very narrow stripes (high p): the gap between the modes is much larger than the linewidth of the single mode and all modes can be distinguished.
- intermediate ratio: the modes start to merge and cannot be fitted accurately
- very wide stripes (small p): the modes overlap indistinguishably and are located at almost the same resonance field showing one single mode.

Both the narrow and wide case are crucial from an experimental point of view. However, the balance between the lowest possible spatial resolution of the setup and a proper mode spacing has to be found. For a 3.5 nm thin iron, a width of 2.8 µm is chosen for a proper measurement resolution as well as a good mode spacing of about 4 mT. Above 10 µm, all modes overlap and form the well-known FMR mode. Fig. 3.11 shows the dependence of the Kerr signal for three different stripe widths for a fixed film thickness calculated by micromagnetic simulations. All in all, a reduction of the stripe width down to several micrometers leads to a displacement of the resonance position of the individual modes towards lower fields. Higher modes decrease in terms of the signal amplitude and move to even smaller magnetic fields.

For this reason, it is essential to study the eigenmodes in the very narrow case by performing numerical calculations. The mode profiles and corresponding eigenfrequencies at a given external field are calculated for the corresponding material parameters. By repeating this for a wide range of fields, it is possible to visualize the modes. In Fig. 3.12(a), the modes are plotted as dispersion branches in a H_{ext} vs. f plot. An intersection at a fixed frequency determines the resonance position of each mode. There, the equivalent eigenmodes are taken and their amplitudes are scaled with their excitation efficiencies, as shown in panel (b). Here, only odd modes with mode numbers $n = 1, 3, 5, ...$ are excited due to a homogeneous driving field, which fully suppresses modes with even mode numbers by a simple geometrical consideration of the cross section. Panel (c) displays the eigenmodes as a 2D color plot with the x axis as magnetic field and y axis as the spatial coordinate across the stripe. In a next step, a finite linewidth ΔH is added as an artificial linewidth broadening. For SSWs with small $\mathbf{k}$ vector, the quality factor and frequency linewidth Δf are approximately equal to the one of FMR [76]. Then, the linewidth has to be converted back, which depends on the slope of the dispersion relation [92]. The difference between different dispersion branches is very small, thus the same linewidth ΔH is suitable for all modes. For the final pattern (d), the modes are convolved with a Gaussian beam profile along the y direction taking into account the finite laser spot in the experiment. This result is in good agreement with the experimental data where almost the same mode pattern is observed, as shown in subplot (f). The mode spectrum is plotted in (e) where a multi-peak fit with a fixed linewidth for all modes resolves the first four peaks very well.

3.5.2 Transversely magnetized stripe

The field is now applied perpendicular to the stripe axis ($\mathbf{H}_{\text{ext}} \parallel \hat{y}$, $\phi_H = 90°$) resulting in the backward volume (BV) geometry, introduced in Sec. 2.6. This leads to a different behavior in three points: first, the negative dispersion relation of a BV mode exhibits a much smaller slope around $\mathbf{k} = 0$ compared to the DE case. This causes a much smaller mode spacing and has to be kept in

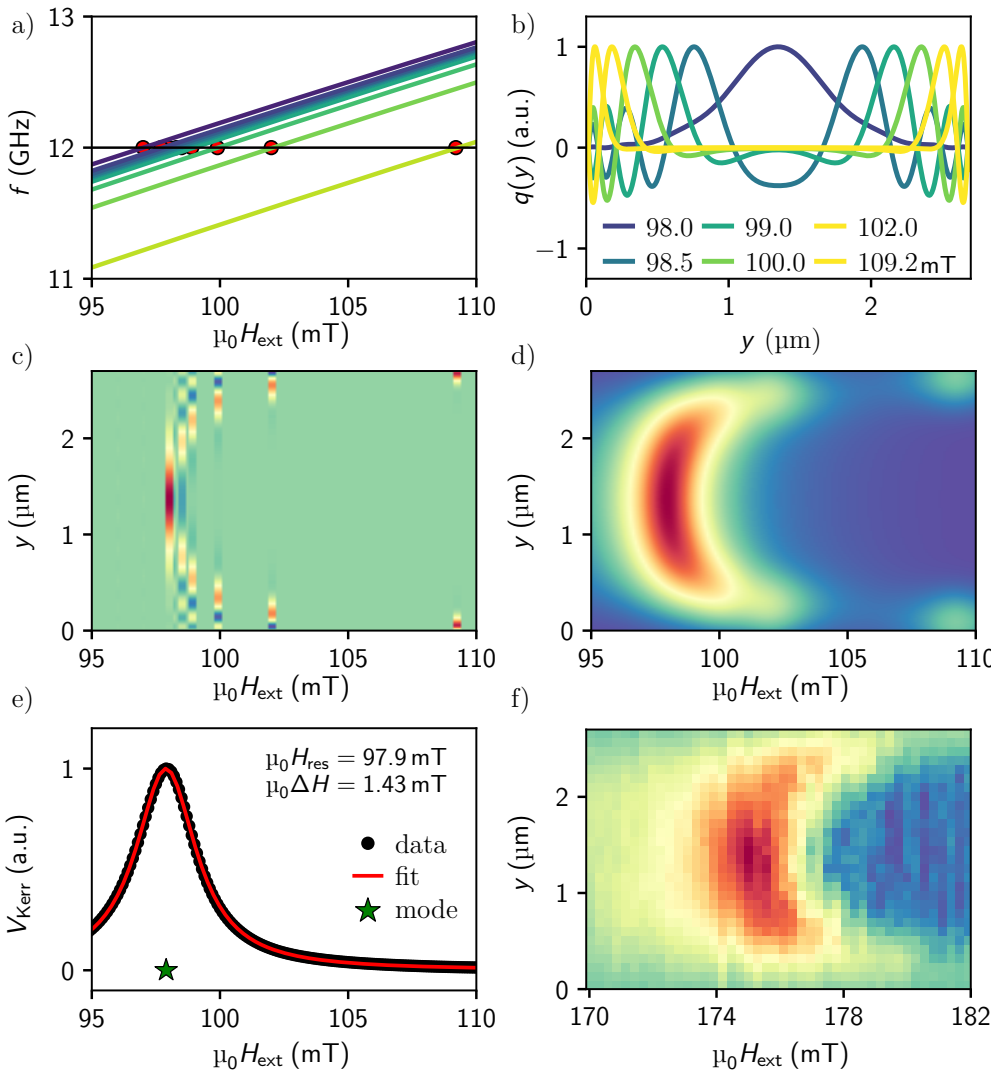

Figure 3.13: Numerical calculation of SSW for a perpendicularly magnetized 3.5 nm thin and 2.8 µm wide Fe stripe. a) most of the modes are located at the same field due to a small slope in the dispersion relation. b) at higher fields, the modes move to the edge and form so-called edge modes. c) Location of the modes in a (H,y) diagram with d) added linewidth and laser beam width to get a realistic mode pattern. e) field dependence in the middle of the stripe shows one big peak due to merged modes. f) measured data reflects the numerical data quite well for a [-110] hard axis direction.

mind when distinguishing the different modes as a function of magnetic field. Second, the static demagnetization field of the BV geometry mentioned earlier provokes an inhomogeneous internal field across the stripe width, as given in Eq. (2.51). The eigenmodes are deformed since, in first approximation, the dispersion relation matches with the internal field at every point in y. This is no longer possible when approaching the edge, which fully suppresses the magnetization precession. Therefore, the maximum of the mode moves towards

the stripe center and away from the edges. Third, so-called edge modes appear next to the stripe border at higher fields, which cannot be described by an analytic formula. Nevertheless, the eigenmodes and frequencies can be obtained numerically as discussed in the longitudinal case.

Fig. 3.13 pictures the calculated results in the same layout as in the DE case. From the fact that the spacing of the modes is much smaller compared to the DE geometry, the dispersion branches lie closer together by forming a thin band for lower fields. This can be seen as blue and yellow lines in panel (a), where the first mode with $n = 1$ is now lowest in field. The higher modes are compressed towards the center and located at higher fields due to the slightly negative slope of the BV dispersion relation for small $\mathbf{k}$. The edge mode (red line) is located at higher fields and well separated from the other band of modes. Panel (b) confirms that the mode profile is mostly located at the edges of the stripe. The position of the modes in space and field coordinates is displayed in (c) as well as the linewidth broadened pattern in (d). The closely packed modes cannot be distinguished by the fit leading to an overestimated linewidth. The experimental data in panel (f) shows a big difference in resonance field position since the anisotropy fields are not considered in the calculation. Qualitatively, the same shape is obtained experimentally, as shown in subplot e).

3.6 Static equilibrium change method

The equilibrium change method is a static, optical technique devised in order to determine spin-orbit fields [10]. The magnetization is excited at time scales of kHz and thus can be treated approximately adiabatic or quasi static compared to the microwave excitation explained previously. The next section discusses this approach, since it allows a comparison of the different methods.

Fan et al. developed a magneto-meter to determine the spin-orbit fields and torques by an optical MOKE measurement without applying any electrical bias current [10]. It is an elegant method, which is based on the fact that the magnetic fields which arise due to an ac-current shifts the magnetization vector slightly away from its equilibrium position. This gives an opportunity to quantify directly the strength of the spin-orbit torques. The new approach is independent of the damping compared to modulation of damping (MOD) experiments. The approach is easy to realize by an optical setup where the out-of-plane component of the magnetization is detected without any temporal resolution.

3.6.1 Simplified TRMOKE setup

Fig. 3.14 sketches a simplified TRMOKE microscope setup without the time-resolution part and the pulsed laser system. Instead, linearly polarized light from a laser diode with a wavelength of about 820 nm probes the *oop*-component

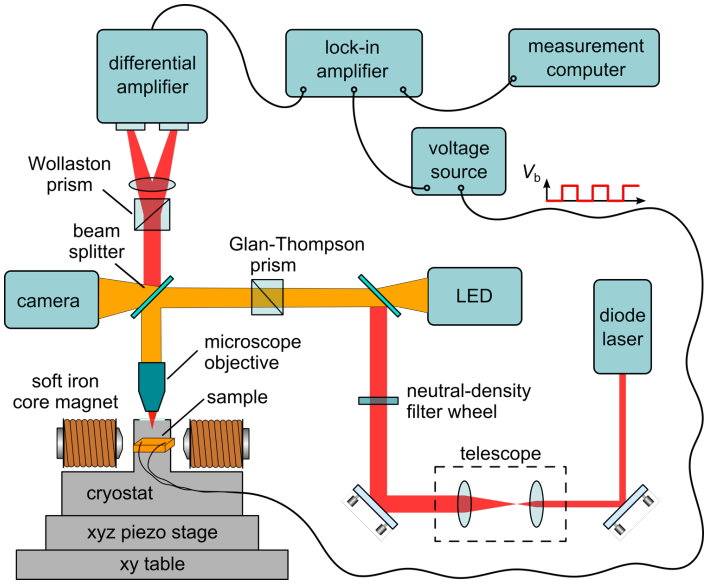

Figure 3.14: Simplified TRMOKE setup with a laser diode and a cryostat which provides temperatures down to a few Kelvin using liquid helium (image taken from [47]).

in the PMOKE geometry. The reflected light from the FM surface is analyzed by a Wollastone prism and two photo diodes convert the signal into two voltages as in the former case. A waveform generator provides a sinusoidal 6.6 kHz signal with a peak-to-peak voltage up to 10 V. This ac-signal feeds also a lock-in amplifier as a reference signal in order to increase the signal-to-noise ratio. An external field can be applied in-plane along the stripe axis up to 220 mT and a cryostat enables temperatures down to a few Kelvin. The positioning of the sample in all three directions is realized by a piezo stage. It can be utilized to fulfill line scans across the stripe on the desired step size.

3.6.2 Theoretical background

The magnetization vector can be decomposed into an equilibrium position $\mathbf{m}_{\mathrm{eq}}$ and an additional shift Δm from the torques since the driving torques are quasi static. For an in-plane magnetized FM layer and therefore an in-plane spin polarization, the damping-like torque $\mathbf{m} \times (\mathbf{m} \times \boldsymbol{\sigma})$ induces an out-of-plane tilt while the field-like torque $\mathbf{m} \times \boldsymbol{\sigma}$ causes an in-plane displacement of $\mathbf{m}_{\mathrm{eq}}$.

This shift can be expressed with Eq. (2.37) in the normal coordinate system which reduces to

$$\Delta\mathbf{m} = \chi_{st} \cdot \mathbf{w} = \begin{pmatrix} 1/\mathcal{H}_1 & 0 \\ 0 & 1/\mathcal{H}_0 \end{pmatrix} \cdot \begin{pmatrix} w_{y'} \\ w_{z'} \end{pmatrix} \tag{3.26}$$

by assuming a static excitation $\omega \to 0$ and a static susceptibility χ_{st}. The driving fields are given by $w_y = h_y^{\mathrm{Oe}}(y) - \tau_{\mathrm{DL}}/\mu_0\,\sigma_z$ and $w_z = h_z^{\mathrm{Oe}}(y) - \tau_{\mathrm{DL}}/\mu_0\,\sigma_y$. It

is noted, that h_z^{Oe} has the same effect on m_z as a damping-like torque from an in-plane spin-polarized current from a NM layer.

The polar MOKE microscope is only sensitive to the component m_z, which reduces Eq. (3.26) to

$$\Delta m_z = \frac{h_z^{\mathrm{Oe}}(y) - \tau_{\mathrm{DL}}/\mu_0 \cos(\phi_H)}{\mathfrak{H}_0} = \frac{h_z^{\mathrm{Oe}}(y) - \tau_{\mathrm{DL}}/\mu_0 \cos(\phi_H)}{H_{\mathrm{ext}} - M_{\mathrm{eff}}} \tag{3.27}$$

with the effective magnetization M_{eff}.

The effect of an *oop* field h_z^{Oe} on m_z is independent of the magnetic field angle compared to the SOT contribution which follows a cosine dependence of ϕ_H. For this reason, the in-plane applied external field should always be parallel to the stripe ($\phi_H = 0°$) in order to maximize the damping-like torque and thus the tilt of the magnetization and signal amplitude. The sign of m_z changes if the direction of the magnetic field is reversed due to the double cross product in the damping-like torque term.

The two different contributions to m_z can be separated into two equations with respect to their driving mechanism:

$$\Delta m_{z,\mathrm{SOT}} = \frac{1}{2}\left[m_z(+H_{\mathrm{ext}}) - m_z(-H_{\mathrm{ext}})\right], \tag{3.28}$$

$$\Delta m_{z,\mathrm{Oe}} = \frac{1}{2}\left[m_z(+H_{\mathrm{ext}}) + m_z(-H_{\mathrm{ext}})\right]. \tag{3.29}$$

The Oersted field can be calculated by Ampere's law to

$$h_z^{\mathrm{Oe}}(y) = \frac{I_{\mathrm{ac}}}{2\pi w} \ln\left(\frac{w - x_0}{x_0}\right) \quad x_0 \leq y \leq x_0 + w \tag{3.30}$$

with the calibrated current I_{ac}, the width w and the position of one edge x_0 of the stripe.

The magnetic response for an ac-current flowing through a FM stripe from Eq. (3.27) can be rewritten in terms of fields to

$$\Delta m_z = \frac{h_{\mathrm{SOT}} + h_z^{\mathrm{Oe}}(y)}{H_{\mathrm{ext}} + M_{\mathrm{eff}}} \quad x_0 \leq y \leq x_0 + w \tag{3.31}$$

with the spin-orbit torque field h_{SOT}. Notably, the denominator in Eq. (3.31) is responsible for the signal strength and depends on the magnetic orientation of the sample. The *oop* tilt and SOT magnitude are smaller for in-plane magnetized samples if m_z is detected. In case of a Py/Pt bilayer, a signal related to the SOT can be observed for the Py/Pt bilayer. However, the signal on a Fe/GaAs(001) layer is too weak because of the effective magnetization is about twice as large.

3.6.3 Determining the spin-orbit fields

A line scan across the stripe is needed to resolve the logarithmic contribution of $h_z^{\mathrm{Oe}}(y)$ from Eq. (3.30), since the Oersted field depends on the lateral stripe

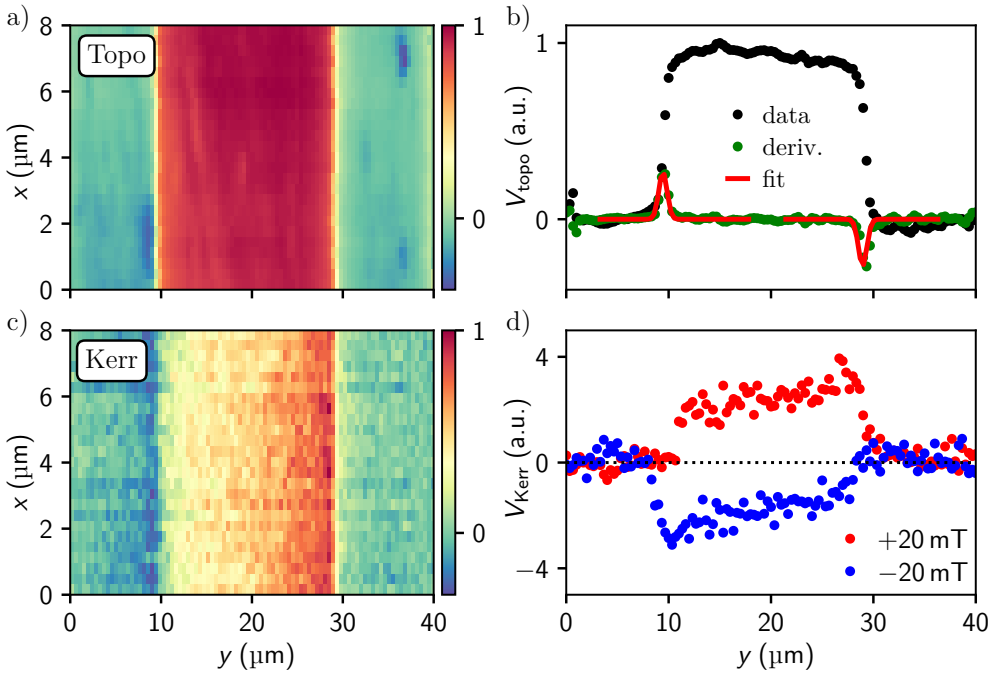

Figure 3.15: a) The topographic signal of several line scans along the y-direction gives a proper signal for edge detection of a $40\times10\,\mu m^2$ stripe. b) The derivative of the sum signal can be easily fitted by two Gaussian profiles to extract the exact edge position of the stripe. c) The detected Kerr signal for a fixed magnetic field of 20 mT and a current density of $5\cdot10^{10}\,A/m^2$ shows an asymmetric signal across the stripe which is opposite for reversed external field direction as seen in panel d).

coordinate. Fig. 3.15(a) shows the recorded topographic signal V_{Topo} in false colors measured in steps of 300 nm for several line scans across a $40\times10\,\mu m^2$ Py/Pt stripe. In panel (b), the scans are averaged along the x axis in order to improve the signal-to-noise ratio. Two Gaussian functions fit the derivative of the topography signal which is done in order to find the exact position of the two stripe edges. Panel (c) displays the Kerr signal on the stripe which steadily increases from the left to right side on the stripe for a magnetic field of 20 mT. In panel (d), the averaged line scans are plotted for the two opposite magnetic fields of ±20 mT. A sign change of the amplitude can be observed as well as a similar slope. The first issue indicates the sign change of m_z while the latter corresponds to the Oersted field which is independent of the field direction.

In the next step, both curves are either subtracted or added to obtain the SOT or Oersted voltage, respectively. The two contributing voltages can be expressed as

$$V_{\mathrm{SOT}} = \frac{1}{2}\left[V_{\mathrm{Kerr}}(+H_{\mathrm{ext}}) - V_{\mathrm{Kerr}}(-H_{\mathrm{ext}})\right], \tag{3.32}$$

$$V_{\mathrm{Oe}} = \frac{1}{2}\left[V_{\mathrm{Kerr}}(+H_{\mathrm{ext}}) + V_{\mathrm{Kerr}}(-H_{\mathrm{ext}})\right]. \tag{3.33}$$

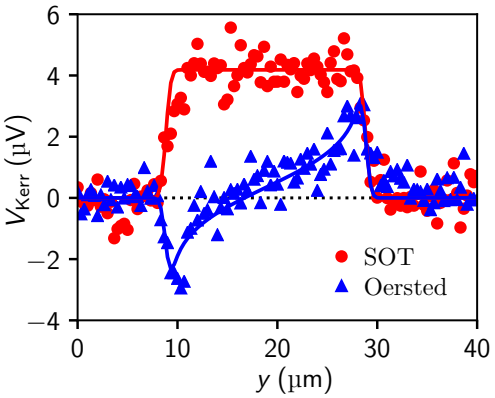

Figure 3.16: Both Kerr signals for positive and negative fields can be subtracted or added in order to access the spin-orbit torque or Oersted contribution respectively. The corresponding curves can be fitted with the given equation to extract the amplitudes.

Fig. 3.16 shows the resulting curves of both voltages from Eq. (3.32) and (3.33) as a related SOT signal (red) and an anti-symmetric Oersted voltage (blue). The constant amplitude on the stripe models the spin-orbit torque related signal, whereas the Oersted signal is calculated with Ampere's law. Both curves are fitted simultaneously with the same conversion parameter η_{MOKE} in order to cancel the MOKE contribution from the two detected signals [10]. This is realized by means of a least-square algorithm, which minimizes the difference between the fit and data by adjusting the fitting parameters of the SOT amplitude V_{SOT} and conversion factor η_{MOKE} for a fixed magnetic field and current. The parameter η_{MOKE} occurs as a variable in both formulas and has units of µV/mT. It relates the SOT signal to the Oersted voltage by fitting both contributions simultaneously in order to obtain the SOFs in units of millitesla [11].

The spin-orbit related voltage from Eq. (3.32) can be expressed with the help of Eq. (3.31) to

$$V_{\mathrm{SOT}} = \frac{h_{\mathrm{SOT}}}{H_{\mathrm{ext}} + M_{\mathrm{eff}}} \quad x_0 \leq y \leq x_0 + w. \tag{3.34}$$

The broadening effect from the laser beam is considered by convolving the fitted data with a Gaussian beam profile with a diameter of 600 nm. Moreover, the method is self-calibrated since the SOT term is related on the Oersted field generated by the same current flow. Notably, it is crucial to determine the correct position of the edges since the logarithmic term in Ampere's law diverges at both edges. From the fit, both amplitudes V_{SOT} and V_{Oe} are determined in order to calculate the SOT field to

$$h_{\mathrm{SOT}} = \frac{V_{\mathrm{SOT}}}{\eta_{\mathrm{MOKE}}} \tag{3.35}$$

with the conversion factor $\eta_{\mathrm{MOKE}} = V_{\mathrm{Oe}}/h_z^{\mathrm{Oe}}$. Finally, a material specific spin-torque efficiency β_{SOT} with the unit nanometer can be defined as [11, 93]

$$\beta_{\mathrm{SOT}} = \frac{h_{\mathrm{SOT}}}{j_{\mathrm{ac}}}, \tag{3.36}$$

which relates the SOF to the current density.

3.7 Micromagnetic simulations

In order to reproduce the mode pattern in the Fe/GaAs measurements, micromagnetic simulations are performed using the MuMax3 package which is an open-source simulation program [94]. It enables the calculation of the space- and time-dependent magnetization dynamics by solving the LLG equation. Periodic boundary conditions are set in x direction for an infinitesimal long stripe along this direction. For a given microwave driving frequency, one line scan of $\mathbf{m}(t, y)$ across the stripe is taken where dynamic quantities, such as the precession amplitude and phase, are calculated on every point on the grid.

quantity	value
α	0.0036
$\mu_0 M_\mathrm{S}$	2.1 T
$\mu_0 M_\mathrm{eff}$	1.8 T
$\mu_0 H_\mathrm{uni}^{\parallel}$	81.4 mT
$\mu_0 H_4^{\parallel}$	34.1 mT
$\mu_0 H_\mathrm{uni}^{\perp}$	-46.1 mT
γ	185 GHz/T
A_ex	$13 \cdot 10^{-12}$ J/m

Figure 3.17: Material parameters for a Fe/GaAs(001) system which are used for the micromagnetic simulations.

The simulations verify the experimentally determined mode spectrum excited by both the out-of-plane driving field and the current flow. Therefore, a stripe with the dimension of 1400 µm×2.8 µm×3.5 nm is defined. The volume is divided into a three dimensional grid with cell numbers of $N_x = 2$, $N_y = 1024$ and $N_z = 1$, respectively. The stripe is assumed to be infinitely long along x and consists of only a single FM layer since the thickness is in the range of the exchange length. This is also valid for the cell size of about 2.8 µm/1024 ≈ 2.7 nm in lateral coordinate.

In the DE geometry for example, the initial magnetization is aligned parallel to the stripe in x direction. In the next step, all relevant magnetic fields are included: the externally applied field, uniaxial in- and out-of-plane field, fourfold anisotropy fields, spin-orbit fields and Oersted field generated from the current. Further, material dependent parameters are applied like the Gilbert damping parameter, saturation magnetization and exchange constants. The most important quantities used for the Fe/GaAs(001) system are summarized in Tab. 3.17.

The resulting magnetization profile across the stripe is saved after a measurement time of 10 ns which corresponds to 120 excitation cycles. The procedure is repeated for a set of different magnetic fields in order to observe the evolving mode spectra as a function of the applied field. The corresponding magnetization profiles are convolved with a 2D Gaussian beam profile to account for the experimental broadening of the laser beam.

3.8 Bolometric current calibration

The magnitude of the current density in a stripe is crucial for the calculation of the generated Oersted field. However, the power from a rf-signal generator is dissipated by devices and cables which makes it necessary to calibrate the cur-

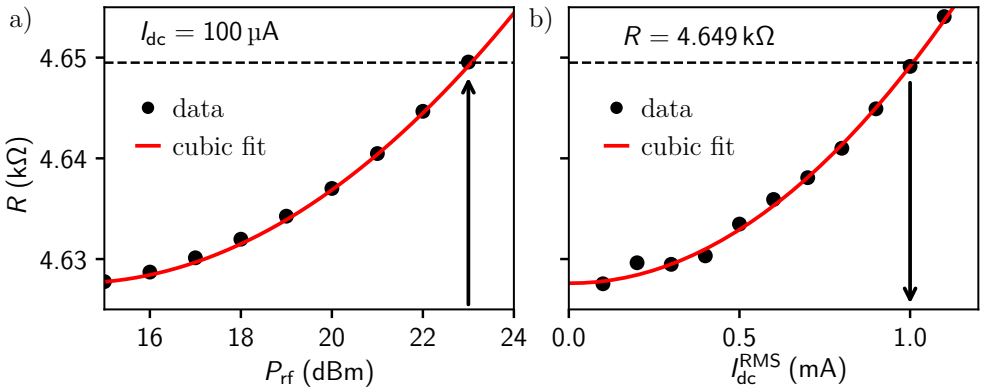

Figure 3.18: The resistance as a function of rf-output power a) and the applied dc-current b) follow a quadratic behavior indicating a bolometric heating effect. The applied rf-power corresponds to a certain resistance which is used to read out the dc-current of a $R - I_{dc}$ measurement.

rent properly. The bolometric effect is described by a temperature dependent resistance due to heating effects from an applied current [95]. Since the resistance is directly proportional to the temperature, it is possible to compare the Joule heating from a current with a very small well-defined applied dc-current in a separate measurement.

Fig. 3.18(a) shows the resistance for an applied rf-output power when an additional dc-current of 100 µA is fed through the device by two bias tees. The curve reveals a quadratic behavior for an increasing rf-power which is in accordance with the heating effect following a cubic function. A resistance of about 4.65 kΩ is received at an input power of 23 dBm. Fig. 3.18(b) shows the resistance as function of different applied dc-currents, where a current of 1 mA is obtained at the previously determined resistance. This is equal to the root-mean-square (rms) value of $I(t) = I_{RMS} \cdot \cos(\omega t)$ which leads to a final current of $I = I_{RMS} \cdot \sqrt{2} = 1.5\,mA$.

4

Experimental detection of spin-orbit torques in a Py/Pt bilayer

The conversion efficiency of charge into pure spin currents can be investigated in a Py/Pt stripe. The magnetization of a 4 nm thin Py layer is excited by the spin-transfer torque generated by a spin-polarized current in the platinum layer [36]. Two important parameters, the spin Hall angle and spin diffusion length, can be determined in a platinum thickness dependence by the introduced ST-FMR technique. Thereby, an interface-related spin Hall angle can also be quantified which can be compared with other measurement techniques. Experiments with samples from the same wafer were realized by optically detected modulation of damping (MOD) and spin-pumping inverse spin Hall effect (SP-ISHE) by Martin Decker in his thesis [37] and the results are summarized in Tab. 4.1.

Motivated by diverging results from SP-ISHE and MOD in Tab. 4.1, new devices are fabricated from the formaly measured Py/Pt wafer in order to review the results with the ST-FMR approach. Moreover, two additional techniques, namely the static equilibrium change method and electrically detected modulation of damping, are tested by assuming a transparent interface with a fixed Pt layer. Finally, a temperature dependence on the spin Hall angle is revised by ST-FMR and the equilibrium change method for a 8.4 nm thick Pt layer. All wafer properties can be found detailed in the work of Martin Decker [37]. Here, only features relevant for this thesis are listed. Two wafers were produced to guarantee several different Pt layers. However, the Py layer is slightly different between both wafers, thus a proper data evaluation of both wafers is needed.

	ISHE	MOD
$\theta_{\mathrm{SHA}}^{\mathrm{eff}}$	-	0.10 ± 0.01
λ_{Pt} (nm)	-	1.1 ± 0.1
$\theta_{\mathrm{SHA}}^{\mathrm{eff}}\lambda_{\mathrm{Pt}}$ (nm)	-	0.12 ± 0.01
$\theta_{\mathrm{SHA}}^{\mathrm{i}}$	0.31 ± 0.04	0.45 ± 0.05
$\lambda_{\mathrm{Pt}}^{\mathrm{i}}$ (nm)	1.7 ± 0.4	0.09 ± 0.01
$\theta_{\mathrm{SHA}}^{\mathrm{i}}\lambda_{\mathrm{Pt}}$ (nm)	0.54 ± 0.05	0.41 ± 0.02

Table 4.1: Summarized former results of the spin Hall angle, spin diffusion length and the product of them. The first three rows relate to a transparent interface whereas the last three are derived assuming an interface within the drift diffusion model (data taken from [37]).

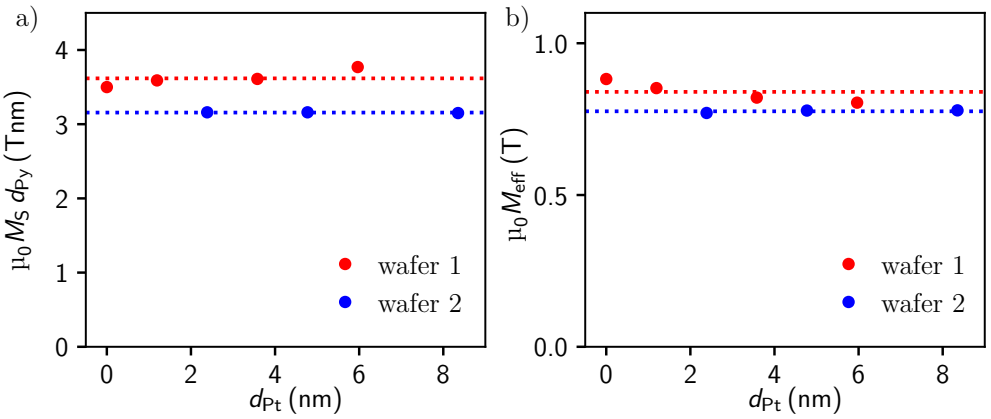

Figure 4.1: a) Two sets of MBE-grown Py/Pt wafers show a different saturation magnetization since the thickness of the Py layer is slightly different. b) This corresponds the derived effective magnetization carried out by a full-film FMR measurement with the Kittel formula.

4.1 Magnetic properties

The magnetic properties of the two wafers are already characterized in the PhD thesis of Martin Decker [37]. Nonetheless, the results are important for the evaluation of the measured data and briefly discussed in the following.

Fig. 4.1(a) shows the saturation magnetization M_S for a set of different platinum layers, which are measured by super conducting quantum interference device (SQUID) on an unprocessed piece of Py/Pt wafer. Two separated sets of data points are attributed to the two individual different wafers (red and blue) due to slightly different growth conditions between the wafers and perhaps difference in Py thickness. Nevertheless, a value of about $\mu_0 M_S = 0.85\,\mathrm{T}$ is obtained which agrees very well with the literature value of 1.0 T and confirms a good wafer quality [96].

In a next step, the samples are characterized by in-plane full-film FMR introduced in Sec. 3.2.3. A frequency dependence of the FMR spectrum is carried out to extract the effective magnetization M_{eff} and the Gilbert damping parameter α. The resonance field H_{res} and linewidth ΔH can be extracted from a fit with an anti-symmetric Lorentzian function with Eq. (3.4). The effective magnetization M_{eff} is determined by a fit of H_{res} as function of f with the Kittel formula from Eq. (2.43). There, the gyromagnetic ratio is fixed to $\gamma = 185\,\mathrm{GHz/T}$, which is observed by a separate measurement on a 20 nm thick Py film. The results are visualized in panel (b), where the same behavior is observed as for the saturation magnetization previously. The linewidth ΔH as a function of the frequency can be evaluated by a linear fit with an offset with Eq. (3.5). The Gilbert damping parameter α is obtained with the gyromagnetic ratio given above and depends on the platinum thickness since the spin-pumping

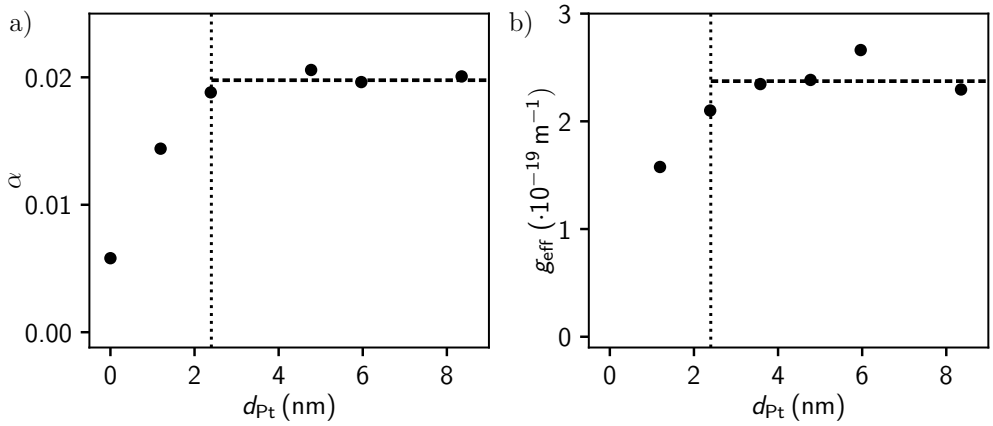

Figure 4.2: The Gilbert damping parameter (a) and spin-mixing conductance (b) increases with increasing platinum thickness and saturates at about 0.02 and $2.2 \cdot 10^{19}\,\mathrm{m}^{-1}$ respectively. Both values start to saturate above roughly 2.5 nm, which is indicated by the vertical dashed line.

into the Pt layer causes a linewidth broadening.

Fig. 4.2(a) shows an increase of the damping parameter from pure Py with $\alpha = 0.008$ to a saturated value of $\alpha \approx 0.02$ above a Pt thickness of about 2.5 nm, indicated by the vertical dashed line. The introduced spin-mixing conductance accounts for the interface contribution and links directly to the damping constant with Eq. (2.21). For this reason, an almost identical behavior is observed where the saturated level starts at about 4 nm, see panel (b).

4.2 Experimental results

With the magnetic wafer characterization, the conversion efficiency of a charge into a spin current can be investigated. Therefore, a $100 \times 20\,\mu\mathrm{m}^2$ Py/Pt stripe is patterned out of the wafer by EBL lithography where two bondpads at both ends ensure a direct injection of a charge current. The sample is measured in the electrical FMR setup introduced in Sec. 3.2.1. Here, the principle is recapped shortly: an in-plane polarized spin current from the Pt layer enters the ferromagnetic layer through the interface and excites the magnetization in the Py layer. The precession of $\mathbf{m}$ causes a change in the anisotropic magnetoresistance which is of the same frequency as the driving rf-current. This rectification leads to a dc-voltage which is built up along the sample and can be picked up by two bias tees before and after the sample holder.

4.2.1 Spin-transfer torque FMR

The measurement routine is as follows: an external magnetic field is continuously increased while the rectified dc-voltage is recorded by a nanovoltmeter. This is repeated for a set of rf-frequencies f for every sample thickness. Here,

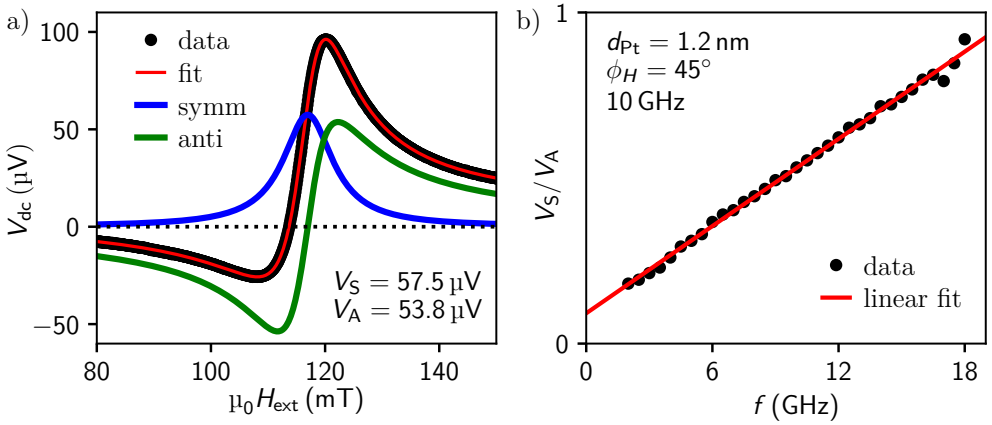

Figure 4.3: a) Typical measured dc-voltage signal for a frequency of 10 GHz at a magnetic field angle of 45° with the fitted symmetric and anti-symmetric Lorentzian line shapes. b) The ratio V_S/V_A of both voltages shows a linear dependence.

the magnetic field angle is fixed to $\phi_H = 45°$ in the following for all experiments since here the excitation efficiency is maximal providing a very clear signal. The detected dc-voltage for a single magnetic field sweep is a mixture of both symmetric and anti-symmetric Lorentzian line shapes, see Eq. (3.12).

Fig. 4.3(a) shows the raw data of a typical voltage (black dots) at a rf-frequency of 10 GHz. The data can be fitted by a combination of a symmetric and anti-symmetric Lorentzian functions (red line). The individual curves are displayed in blue and green for the symmetric and anti-symmetric part with their magnitudes, respectively. The resonance field H_{res} and linewidth ΔH can be extracted from the fit by using the same fit parameter in both Lorentzians. Panel (b) displays the ratio of both voltages magnitudes, V_S/V_A as function of the frequency for a 1.2 nm thin Pt sample indicating a linear dependence.

The spin Hall angle for a certain frequency is given by the ratio of the charge and spin current introduced in Eq. (3.15)

$$\theta_{\mathrm{SHA}}^{\mathrm{eff}} = \frac{V_S}{V_A} \frac{e\mu_0 M_S d_{Py} d_{Pt}}{\hbar} \sqrt{1 + \frac{\mu_0 M_{\mathrm{eff}}}{H_{\mathrm{res}}}} \tag{4.1}$$

with all characterized quantities. Notably, no interface contributions such as scattering are regarded, so this could be referred to as an effective spin Hall angle $\theta_{\mathrm{SHA}}^{\mathrm{eff}}$. The linear dependence of the voltage ratio on the frequency is countered by the increasing resonance field H_{res} in the square root since all other parameter are independent of f. For the evaluation process, a mean value between 6-12 GHz is taken with error bars from the standard deviation since low field losses play a major role below 6 GHz. Besides, the transmission of the radio-frequency decreases above 13 GHz, which reduces the signal strength and increases the noise. For every average SHA, about twelve data points are taken at steps of 0.5 GHz, which is sufficient to obtain a proper value.

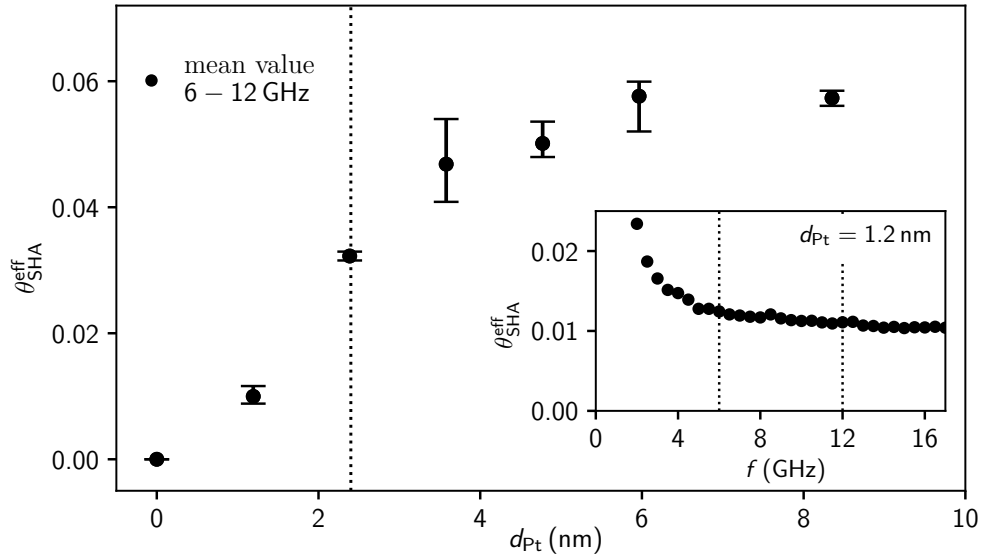

Figure 4.4: The averaged spin Hall angle over many different samples is plotted as a function of platinum layer thickness in a frequency range between $6 - 12\,\mathrm{GHz}$. The spin Hall angle increases up to about 0.06 for a platinum thickness larger than 4 nm where it saturates within the error bars. A final value is extracted to $\theta_{\mathrm{SHA}}^{\mathrm{eff}} = 0.057$ from the two thickest Pt samples. The inset shows the frequency dependence of the SHA for 1.2 nm thick platinum sample.

As an example, the inset of Fig. 4.4 shows the frequency dependence of the spin Hall angle for a 1.2 nm thick Pt sample. There, an effective SHA of 0.0117 ± 0.0004 is found for a frequency range between 6-12 GHz. This is repeated for other fabricated devices with the same platinum thickness, which results in other mean values for the particular layers. Fig. 4.4 shows these mean SHA values for the different layer with the corresponding error bars. The SHA increases from zero to a saturated level of $\theta_{\mathrm{SHA}}^{\mathrm{eff}} = 0.057 \pm 0.004$, which is taken from the mean value of the two thickest Pt layers. The large error results from the sum of each standard deviation of the two samples and is roughly 7 %. Nevertheless, the value matches the published results of 0.056 for the same Py/Pt system [36].

However, an interface-related SHA can account for the contributions by the boundary surface, which is considered by the spin-mixing conductance introduced in Eq. (2.23), to

$$(\eta_{\mathrm{DL}}\theta_{\mathrm{SHA}})^{\mathrm{norm}} = \eta_{\mathrm{DL}}\theta_{\mathrm{SHA}}\frac{h}{2e^2}\frac{\sigma_{\mathrm{Pt}}}{g_{\mathrm{eff}}^{\uparrow\downarrow}} = \theta_{\mathrm{SHA}}\,\lambda_{\mathrm{Pt}}\tanh\left(\frac{d_{\mathrm{Pt}}}{2\lambda_{\mathrm{Pt}}}\right). \tag{4.2}$$

It has been found that the conductivity of the thin Py/Pt bilayer depends not only on the respective bulk conductivity values but rather on the contribution from the interface scattering. A bulk platinum conductivity of $\sigma = 7.3 \cdot 10^6\,(1/\Omega\mathrm{m})$ is used in order to evaluate the data [37].

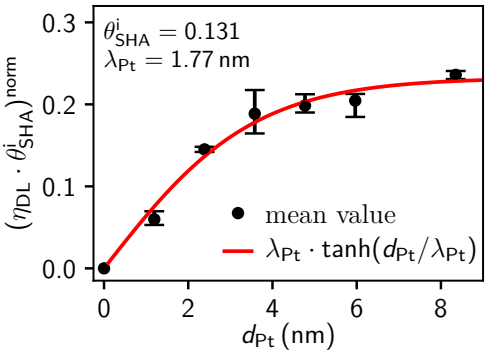

Figure 4.5: The effective spin Hall angle is normalized by the platinum conductivity and spin-mixing conductance. A fit with a tanh-function reveals the interface-related spin Hall angle and the spin diffusion length.

Fig. 4.5 shows the product of the normalized spin Hall angle and the spin efficiency η_{DL} as function of the Pt thickness. The same behavior as for the effective SHA is observed, where a saturated level above about 4 nm is found after a steady increase. The data can be fitted very well with the tanh-function from the Eq. (4.2). Thereby, an interface-related spin Hall angle of $\theta_{SHA} = 0.131$ and a spin diffusion length of $\lambda_{Pt} = 1.77\,nm$ are obtained. This mirrors the values derived by SP-ISHE, see Tab. 4.1, if the SHA is corrected to $\theta_{SHA} = 0.262$ by a factor of two explained later in more detail [40].

4.2.2 Electrical modulation of damping

However, the results are not really in accordance with the optically detected MOD experiments. For this reason, the MOD method is checked again by an electrically detected approach, introduced in Sec. 3.2.7. There, an additional applied dc-current causes a static damping-like torque acting on the magnetization which influences the linewidth of a typical FMR measurement.

Fig. 4.6 displays the linewidth ΔH as function of applied dc-current at a 8.35 nm thick platinum sample. A resonance field of 168.5 mT is found for a rf-frequency of 12 GHz and field angle $\phi_H = 45°$. The slope for positive and negative magnetic fields are $\mu_0 \Delta H / I_C = -0.0406$ and $0.0418\,T/A$, respectively.

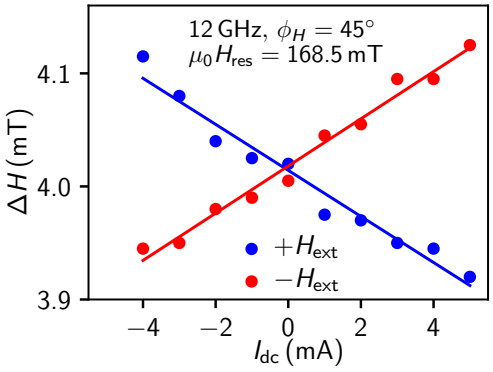

Figure 4.6: Electrical modulation of damping experiment carried out on a 8.35 nm thick platinum sample for field angles of 45° and -135°. A dc-current of several mA is additionally applied during an FMR measurement which changes the linewidth. The mean value of both slopes enables the calculation of the SHA.

The shift of ΔH is caused by the damping-like torque and is given by [36, 90]

$$\mu_0 \Delta H / j_c = \frac{2\pi f}{\gamma} \frac{\sin(\phi_H)}{\mu_0 (H_{res} + M_{eff}/2)} \frac{\hbar}{2e M_S d_{Py}} \cdot \theta_{SHA}^{eff} \tag{4.3}$$

with the spin Hall angle θ_{SHA}^{eff}. It is noted, that the saturation magnetization is inserted in units of A/m and the current density is calculated with the two bilayer model from Eq. (3.1). The mean value of the two slopes is calculated to 0.041 ± 0.005 T/A with an error of 12% from the sum of both linear fits. Finally, an effective SHA is obtained of $\theta_{SHA}^{eff} = 0.10 \pm 0.01$ by assuming a transparent interface. This value is exactly the same as $\theta_{SHA}^{eff} = 0.1$, determined by the optical MOD experiment on the same wafer, see Tab. 4.1. The spin Hall angle can be normalized by the spin-mixing conductance and platinum conductivity from previous values in ST-FMR measurements. Consequently, this gives a reasonable interface-related SHA of $\theta_{SHA}^{i} = 0.37 \pm 0.05$. The magnitude is smaller compared to the optical MOD of 0.45 but larger than 0.31 from the SP-ISHE and ST-FMR method.

4.2.3 Discussion of results

In the following, all derived values are reviewed to explain the reported differences between the SP-ISHE and MOD experiments. Nan et al. proposed an additional factor of two when using the ST-FMR method, since it underestimates the spin Hall angle and ignores the field-like torque contribution [40]. This assumption is based on the difference between the enhanced damping in MOD and the spin injection in SP-ISHE/ST-FMR experiments. For this reason, a factor of two is introduced to increase the damping-like torque. Thus, the previously derived effective SHA changes to $\theta_{SHA}^{eff} = 0.057 \cdot 2 = 0.11$ by assuming a transparent interface. This fits very well to the results from the electrical and optical MOD value of 0.10 in Tab. 4.1, respectively. Other reported values lie between 0.10-0.18 for the ST-FMR method including the additional factor [36, 97, 98].

For a non-transparent boundary, an interface-related SHA $\theta_{SHA}^{i} = 0.131 \cdot 2 = 0.26$ is obtained from the tanh-fit with the factor from above. This is in a good agreement to other publications on the same material system, where a value between 0.2-0.3 is found with the ST-FMR method [38–40]. The comparison of the four different measurement techniques on the same wafer was one of the basic ideas in this thesis. The two results, $\theta_{SHA}^{i} = 0.31$ for SP-ISHE and 0.45 for MOD, are confirmed by experiments using the ST-FMR method $\theta_{SHA}^{i} = 0.26$ and electrical MOD 0.37. The two results from modulation of damping lie within the error bars showing an good accordance by using the same excitation principle but rather a different detection technique. However, both values are much larger than the ST-FMR and SP-ISHE. This deviation could be based on the applied dc-current which causes a static damping-like torque on the

magnetization in contrast to the spin injection. Another explanation could be the different spin diffusion lengths between the two experiments. A relatively low value of only $\lambda_{\mathrm{Pt}} = 0.9\,\mathrm{nm}$ is reported for the optical MOD in contrast to $\lambda_{\mathrm{Pt}} = 1.7\,\mathrm{nm}$ for SP-ISHE, which agrees perfectly with the derived ST-FMR of 1.77 nm.

Moreover, the product of both quantities is introduced to account for the strong correlation between the two parameters and to compare the different techniques. The derived interface-related product

$$\theta^{\mathrm{i}}_{\mathrm{SHA}} \cdot \lambda_{\mathrm{Pt}} = 0.26 \cdot 1.77\,\mathrm{nm} = (0.46 \pm 0.08)\,\mathrm{nm} \tag{4.4}$$

lies between values of 0.41 nm and 0.54 nm for SP-ISHE and optical MOD experiments, respectively. An accordance can be also seen in the case of the other two methods within the error bars. The conversion of a charge into a spin current and vice versa is predicted by theory, which connects the ST-FMR and SP-ISHE with the conversion efficiency θ_{SHA}.

A spin diffusion length of $\lambda_{\mathrm{Pt}} = 1.77\,\mathrm{nm}$ is found which lies in the range of reported values between 0.7-3.7 nm [39, 97, 99–101]. This large variation comes from a strong correlation between the spin Hall angle and the diffusion length due to differences of the platinum growth [100, 102]. Therefore, a relation is proposed by Rojas-Sánchez [100] of $\theta^{\mathrm{eff}}_{\mathrm{SHA}} \cdot \lambda_{\mathrm{Pt}} = 18.8\,\mathrm{nm}$[1], where the SHA is given as a percentage. Our derived value of $\theta^{\mathrm{eff}}_{\mathrm{SHA}} \cdot \lambda_{\mathrm{Pt}} = 11.4\% \cdot 1.77\,\mathrm{nm} = 20.2\,\mathrm{nm}$ is close to the reported value.

In this work, a measured sample conductivity of $\sigma_{\mathrm{Pt}} = 3.21 \cdot 10^6\,\Omega\mathrm{m}^{-1}$ is used as a lower bound within the drift diffusion model. One issue for the diverging values of the spin diffusion length could be the platinum conductivity which relies strongly on the growth technique and layer thickness. In the following, two published results are discussed which classify our derived results with reported values. Sagasta et al. measured the SDL and SHA on spin valve devices by using spin absorption technique for a wide range of different growth techniques [103]. This was done on platinum samples with a wide range of different conductivities from the dirty to the super clean regime. A linear dependence between spin diffusion length and the Pt conductivity is proposed to $\lambda_{\mathrm{Pt}}/\sigma_{\mathrm{Pt}} = 6.25 \cdot 10^{-7}\,\mathrm{nm}\,\Omega\mathrm{m}$. A spin diffusion length of about $\lambda_{\mathrm{Pt}} = 2.0\,\mathrm{nm}$ is found for our used platinum conductivity, which is near the measured value of $\lambda_{\mathrm{Pt}} = 1.77\,\mathrm{nm}$. Further, they claimed an inverse dependence of the spin Hall angle on the conductivity. Here, the conductivity leads to a SHA of around $\theta^{\mathrm{eff}}_{\mathrm{SHA}} = 0.05$ which is also in good agreement with our value of 0.057. A strong variation of the platinum resistivity with thickness was discovered by Nguyen et al., where the Pt layer thickness is rescaled [104]. There, a model is used, where the spin relaxation is dominated by the Elliot-Yafet mechanism $\lambda_{\mathrm{Pt}} \propto \sigma_{\mathrm{Pt}}$ and

[1] does not hold for STT experiments if the transparent interface model is used and if $d_{\mathrm{Pt}} \gg \lambda_{\mathrm{Pt}}$ because then $\eta \approx 1$ and $\theta^{\mathrm{i}}_{\mathrm{SHA}}$ does not depend on the exact value of λ_{Pt} used [100].

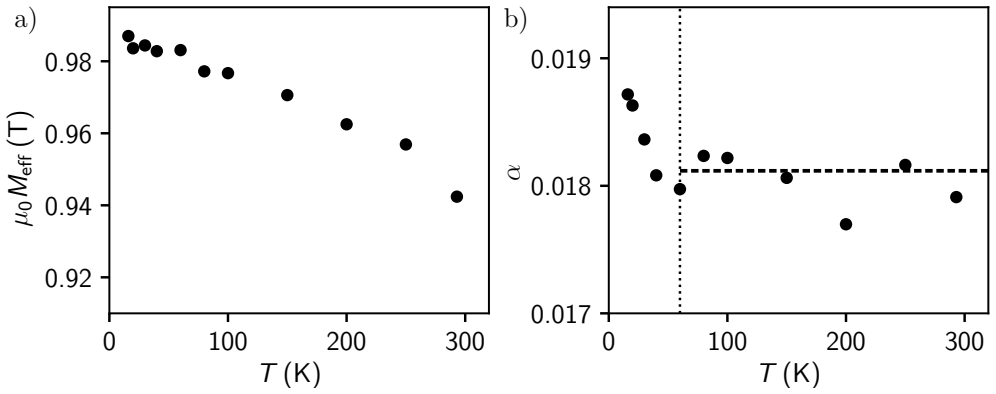

Figure 4.7: a) The effective magnetization M_{eff} is derived from the Kittel formula in a wide frequency range between 4-18 GHz for different temperatures. b) The Gilbert damping parameter is determined by a linear fit of the linewidth in the same frequency range.

the spin Hall effect is of intrinsic nature $\theta_{\mathrm{SHA}} = \sigma_{\mathrm{xy}}^{\mathrm{int}}/\sigma_{\mathrm{Pt}}$. The conductivity can be used to rescale the Pt thickness since $\lambda \cdot \theta_{\mathrm{SHA}}^{\mathrm{eff}} = \mathrm{const}$ holds. With the intrinsic spin Hall conductivity $\sigma_{\mathrm{xy}}^{\mathrm{int}} = 2.95 \cdot 10^5\,\Omega\mathrm{m}^{-1}$ and conductivity $\sigma_{\mathrm{Pt}} = 3.21 \cdot 10^6\,\Omega\mathrm{m}^{-1}$, a spin Hall angle of $\theta_{\mathrm{SHA}}^{\mathrm{eff}} = 0.09$ is calculated. This agrees with the MOD measurements and the ST-FMR method.

4.2.4 Temperature dependence of the torque ratio

Finally, temperature dependent measurements are carried out on a similar cryogenic setup. The measurement procedure is repeated on a 8.35 nm Pt sample for a set of different temperatures. The effective magnetization is determined by a Kittel fit of the resonance field as function of rf-frequency together with the Gilbert damping parameter from a linear fit of the linewidth at every temperature. Fig. 4.7(a) shows a steady increase of M_{eff} for decreasing temperatures down to a few Kelvin. The Gilbert damping parameter stays constant over a wide temperature range and increases below 50 K, see panel (b).

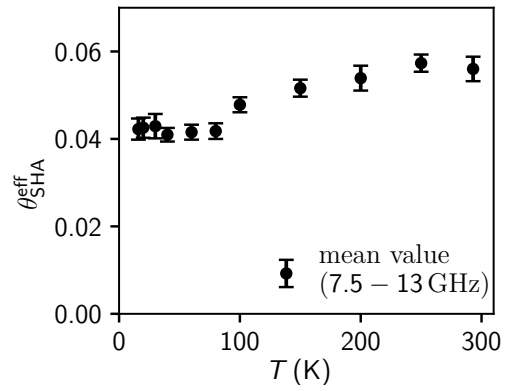

Figure 4.8: The spin Hall angle decreases towards lower temperatures for frequencies between 7.5 and 13 GHz. An effective SHA of $\theta_{\mathrm{SHA}}^{\mathrm{eff}} = 0.056$ is obtained at room temperature.

Fig. 4.8 shows the calculated spin Hall angle over the whole temperature range. Here, a mean value is taken for every data point in a frequency range between 7.5-13 GHz. The calculated effective spin Hall angle at room temperature is $\theta_{\mathrm{SHA}}^{\mathrm{eff}} = 0.056 \pm 0.003$, which is the same obtained with the other measurement setup as expected. The SHA decreases slightly towards lower temperatures and saturates at $\theta_{\mathrm{SHA}}^{\mathrm{eff}} = 0.042 \pm 0.001$ below 80 K. However, no temperature dependence at all is reported by Isasa et al. [105]. An explanation could be the temperature dependent spin diffusion length and platinum conductivity, which is not measured since only a single device was probed.

4.3 Static equilibrium change method

So far, all measurements are performed with an electrical detection method by means of the dc-voltage rectification. In the following, the magnetization is probed by an optical MOKE technique introduced in Sec. 3.6. The magnetization is excited adiabatically from the equilibrium position by a torque in the kHz frequency range. Here, a device with 8.4 nm platinum is measured as in the former temperature measurements.

A line scan across the stripe for two opposite magnetic fields separates the Kerr signal into an Oersted and a spin-orbit torque related signal. As a recap, the sign of the SOT contribution changes for opposing magnetic fields due to the damping-like torque $\mathbf{m} \times \boldsymbol{\sigma}$. The Oersted field contribution is independent of the magnetic field reversal. Thus, the SOT signal is received by processing the two sets of Kerr data with Eq. (3.33), where the voltage difference corresponds to the spin-orbit field and the Oersted contribution to the sum of both line

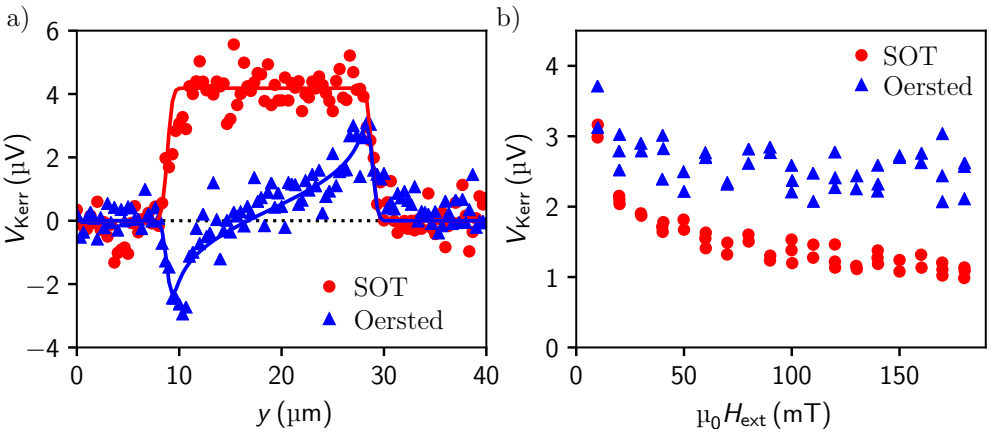

Figure 4.9: a) Subtracting both Kerr signals for positive and negative fields leads to the pure SOT-related signal (red). The Oersted contribution is received by adding both voltages (blue). Both curves can be fitted in order to extract the corresponding magnitudes. b) The field dependence of the SOT signal shows a decrease for higher magnetic field whereas the voltage related to the Oersted field contribution is constant.

scans.

Fig. 4.9(a) shows the two obtained curves for a 20 µm wide stripe with an applied magnetic field of ±20 mT and an ac-current density of $j = 5.3 \cdot 10^{10}\,\mathrm{A/m^2}$. The SOT signal (red dots) has a constant amplitude over the whole stripe width where the magnetization is tilted out of the film plane due to a homogeneous out-of-plane SOF. In contrast, the voltage of the Oersted field (blue triangles) shows an exponential increase from the center towards the edges in opposite directions. Both curves can be fitted well with the corresponding fit functions from Eq. (3.34) and (3.31). The resulting magnitudes of the SOT and Oersted voltage are displayed in Fig. 4.9(b) for a wide range of magnetic fields. The Oersted field related voltage remains constant since it depends only on the current. The SOT-related signal decreases slightly for higher fields due to the larger in-plane applied fields, which reduces the out-of-plane tilt. The increase at zero field is caused by the magnetization not being aligned along the long axis of the stripe due to a too small field strength. Nevertheless, all values can be represented by a mean value properly.

The spin-orbit field h_{SOT} is extracted directly from the fit for the current density of $j_{\mathrm{ac}} = 5.3 \cdot 10^{10}\,\mathrm{A/m^2}$ and visualized in Fig. 4.10(a). Obviously, the same decrease of amplitude occurs, but not as pronounced as for the SOT-related voltage. The SOF magnitude is on the order of several hundreds of microtesla which is sufficient for an in-plane magnetized sample to exhibit a sizable *oop* tilt of the magnetization. A spin-orbit field of $h_{\mathrm{SOT}} = (337 \pm 66)\,\mu\mathrm{T}$ is obtained over the whole field range. Further, a spin-torque efficiency β_{SOT} is introduced from Eq. (3.36), where the SOF is normalized to the current density in order to compare the results with other material systems. A value of $\beta_{\mathrm{SOT}} = (5.6 \pm 1.0)\,\mathrm{nm}$ is found for the used bilayer system. This is smaller than

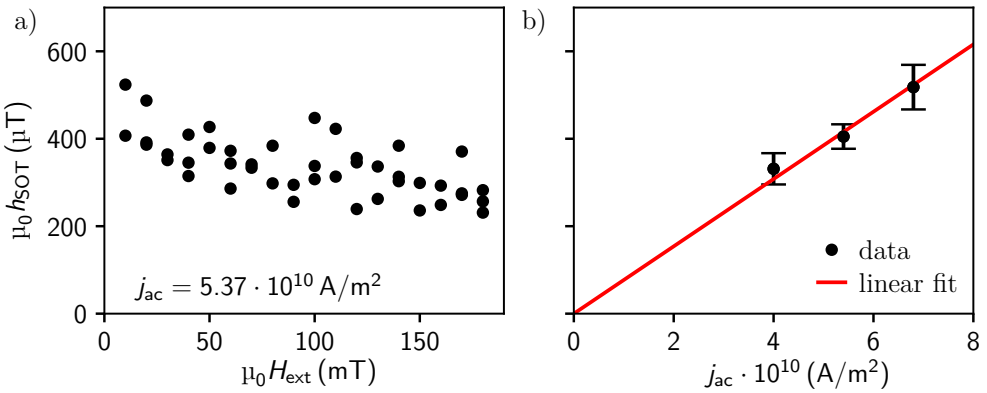

Figure 4.10: a) The spin-orbit field is slightly decreasing towards higher fields for a current density of $j_{\mathrm{ac}} = 5.3 \cdot 10^{10}\,\mathrm{A/m^2}$. A mean value of $h_{\mathrm{SOT}} = (337 \pm 66)\,\mu\mathrm{T}$ over the whole magnetic field range is obtained. b) The spin-orbit field shows a linear dependence on the current density, where the previous field dependent measurements are summarized for a certain current density giving the individual error bars.

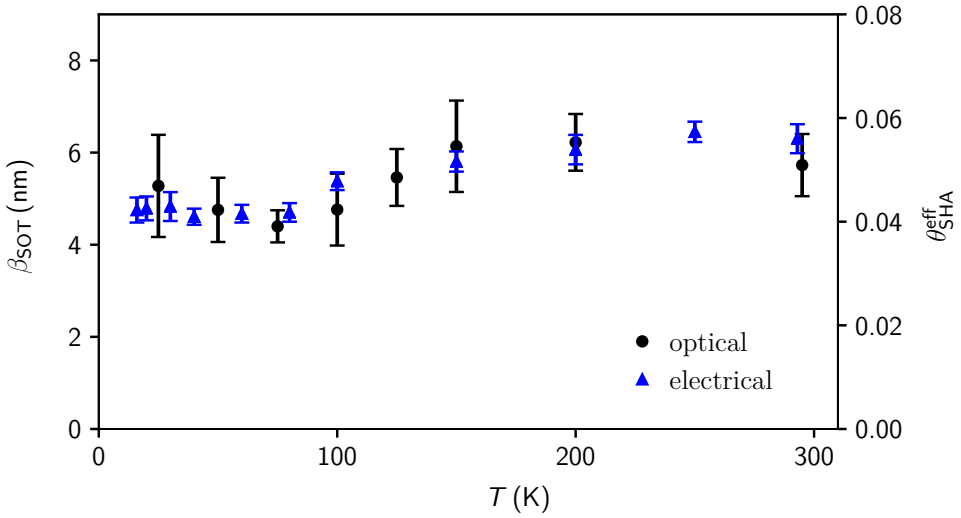

Figure 4.11: The temperature dependence of the spin-orbit torque coefficient obtained optically β_{SOT} (black dots) and electrically derived spin Hall angle $\theta^{\mathrm{eff}}_{\mathrm{SHA}}$ (blue triangles) is the same within the error bars.

the reported value of 12.7 nm for a Py(2 nm)/Pt(5 nm) bilayer [10]. Moreover, for *oop* magnetized samples, as for example Ta/CoFeB/MgO, the efficiency increases to $\beta_{\mathrm{SOT}} = 10 - 30\,\mathrm{nm}$ [106].

Fig. 4.10(b) illustrates the linear dependence of h_{SOT} on the current density. The data points represent mean values at a certain current density for a set of different magnetic fields in order to get reasonable error bars. A linear fit through the origin results in a slope of $h_{\mathrm{SOT}}/j_{\mathrm{ac}} = 7.7 \cdot 10^{-15}\,\mathrm{Tm}^2/\mathrm{A}$. This coincides well with the slope of $9.1 \cdot 10^{-15}\,\mathrm{Tm}^2/\mathrm{A}$ reported for Py(2 nm)/Pt(5 nm) [10]. However, the two values are much smaller compared to a Ta/CoFeB/MgO system with a slope of $30 \cdot 10^{-15}\,\mathrm{Tm}^2/\mathrm{A}$ due to the *oop*-magnetization of this sample [107].

In addition, a temperature dependence on the same device is carried out where a cryogenic head provides temperatures down to a few Kelvin with liquid helium. The measuring procedure is repeated at certain temperatures where a mean value over a range of magnetic fields is taken at a slightly higher current density of $j_{\mathrm{ac}} = 5.6 \cdot 10^{10}\,\mathrm{A/m}^2$. Fig. 4.11 shows the spin-orbit torque efficiency (black dots) as a function of temperature. β_{SOT} decreases at room temperature from 5.6 nm down to smaller values at about 150 K. It increases below 50 K with larger error bars, where a saturated level can be supposed. The temperature dependence looks very similar to the data obtained from ST-FMR measurements in Fig. 4.8, which is discussed in the following.

The spin Hall angle $\theta^{\mathrm{eff}}_{\mathrm{SHA}}$ is related to the spin-torque efficiency parameter β_{SOT} via [36, 90]

$$\theta^{\mathrm{eff}}_{\mathrm{SHA}} = \frac{2e}{\hbar}\mu_0 M_{\mathrm{S}} d_{\mathrm{Py}}\,\beta_{\mathrm{SOT}}. \tag{4.5}$$

This leads to a spin Hall angle $\theta_{\mathrm{SHA}}^{\mathrm{eff}} = 0.11$ for the measured spin-orbit efficiency of $\beta_{\mathrm{SOT}} = 5.6\,\mathrm{nm}$ and $\mu_0 M_{\mathrm{S}}\, d_{\mathrm{Py}} = 3.21 \cdot 10^{-9}\,\mathrm{Tm}$ at room temperature. Further, it is exactly the same value to the electrically measured ST-FMR value of $\theta_{\mathrm{SHA}}^{\mathrm{eff}} = 0.11$ for the very same sample.

5

Electrical detection of spin-orbit fields in the Fe/GaAs system

In this chapter, the introduced Fe/GaAs(001) system is investigated by means of the SOT-FMR technique, where the arising Dresselhaus- and Bychkov-Rashba-like SOFs from the interface are detected electrically. The magnetization in the iron layer is driven by spin currents generated from the spin accumulation at the interface. A rectified dc-voltage builds up along the device, which can be recorded during a magnetic field sweep as explained in Sec. 3.2.4. The obtained voltage curve is evaluated by a fit of two Lorentzian lineshapes and the corresponding magnitudes as function of magnetic field angle give access to the underlying spin-orbit fields.

First, the Fe/GaAs(001) wafer is characterized by various techniques to determine the magnetic properties. Second, the dragging effect due to the anisotropy requires the calculation of the magnetization angle ϕ_M and the susceptibility χ. These two quantities are required in order to determine the in- and out-of-plane Dresselhaus- and Bychkov-Rashba-like spin-orbit fields.

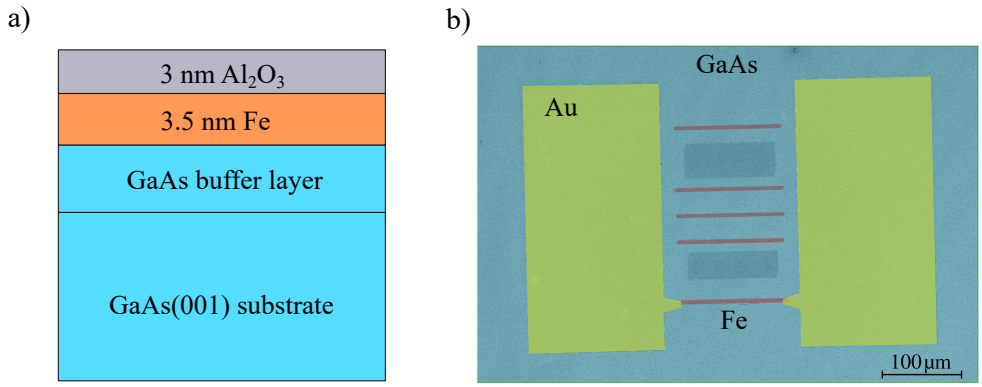

Figure 5.1: a) A stack of the single crystalline Fe/GaAs(001) heterostructure shows C_{2v}-symmetry at the interface between the Fe and GaAs buffer layer. b) One SOT-FMR device, consisting of a narrow Fe stripe and two bondpads, is patterned by EBL along the four main crystallographic axes of the GaAs(001) substrate. Here, only one chosen stripe is connected at the edge out of several wires with varying width.

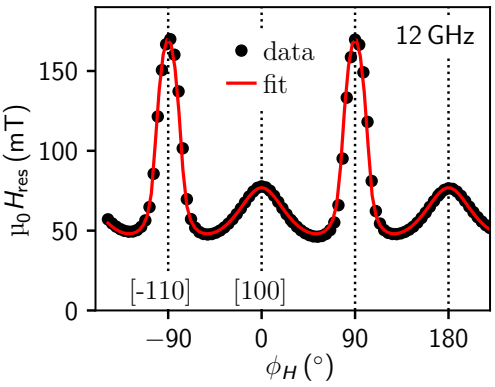

Figure 5.2: The dependence of the resonance field on the magnetic field angle shows a pronounced uniaxial and fourfold anisotropy in a full-film FMR measurement on an unstructured piece of the wafer. Three anisotropy fields of $\mu_0 H_{\text{eff}} = 1.9\,\text{T}$, $\mu_0 H_{\text{uni}} = 47\,\text{mT}$ and $\mu_0 H_4 = -36\,\text{mT}$ are obtained by an angular fit.

5.1 Sample layout and magnetic characterization

Fig. 5.1(a) shows the stack of a 3.5 nm thin, single crystalline Fe film, which is evaporated at room temperature on a freshly prepared GaAs(001) substrate in a metal MBE chamber. The epitaxial growth of iron which is deposited on the GaAs(001) substrate in a III-V MBE system, is ensured by a several nanometer thick GaAs buffer layer since lattice constant of iron is almost half of GaAs. Subsequently, a thin aluminum layer of three nanometers protects the wafer from oxidization. The whole layer growth was monitored by RHEED[1] to guarantee an epitaxial growth of iron. The Fe/GaAs interface exhibits C_{2v}-symmetry [108], where Dresselhaus- and Bychkov-Rashba-like SOFs arise, see Sec. 2.4.1. Devices are fabricated by electron beam lithography, where $100\times2.8\,\mu\text{m}^2$ Fe stripes are patterned along the main four crystallographic axes of GaAs(001). Fig. 5.1(b) shows a Fe stripe, which is contacted by two bondpads on each side for the current-induced SOT-FMR geometry.

Two experiments are carried out in order to characterize the magnetic properties of the Fe/GaAs(001) wafer. First, a $3\times3\,\text{mm}^2$ piece of the wafer is measured by SQUID to determine the saturation magnetization M_S. A value of $\mu_0 M_S = 2.1\,\text{T}$ is obtained for a 3.5 nm thick sample, which is close to the bulk value of iron as expected [109]. In the next step, the bare film is analyzed by the full-film FMR technique, introduced in Sec. 3.2.3. Basically, the magnetization is excited by a driving field from a CPW embedded in a sample holder. The absorbed rf-power is recorded during a steady increase of the magnetic field. The transmitted power is converted by a Schottky diode into a voltage.

Fig. 5.2 shows the resonance field H_{res} as a function of the in-plane magnetic field angle ϕ_H giving access to the anisotropy fields. These can be identified by a fit, which is explained later in more detail. The fitted uniaxial and fourfold anisotropy fields together with the effective magnetization are extracted to $\mu_0 H_{\text{uni}} = 47\,\text{mT}$, $\mu_0 H_4 = -36\,\text{mT}$ and $\mu_0 M_{\text{eff}} = 1.9\,\text{T}$, respectively.

[1] reflection high-energy electron diffraction

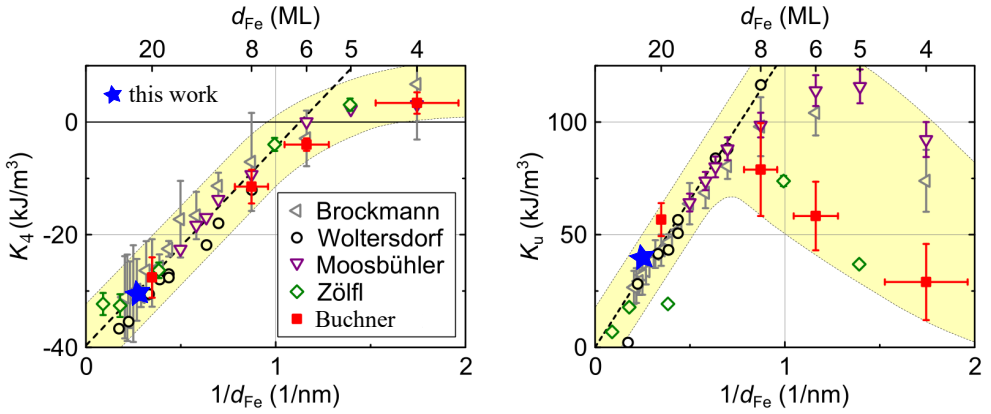

Figure 5.3: Survey of Fe films grown by MBE as a function of inverse film thickness: the measured anisotropy constants (blue stars) confirm the measured values for the four-fold (a) and uniaxial (b) anisotropy, respectively (image taken from [47]).

The anisotropy constants of both fields H_4 and H_{uni} are derived to

$$K_{4/\text{uni}} = \frac{1}{2} H_{4/\text{uni}} \cdot \mu_0 M_S, \tag{5.1}$$

with the saturation magnetization $\mu_0 M_S = 2.1\,\text{T}$. In Fig. 5.3, the two derived values (blue stars) are located at an inverse thickness of $1/d_{Fe} = 0.28\,\text{nm}^{-1}$. The received values of $K_4 = -30.0\,\text{kJ/m}^3$ and $K_{\text{uni}} = 39.3\,\text{kJ/m}^3$ are in good agreement with other Fe layers grown by MBE, which were summarized in [47].

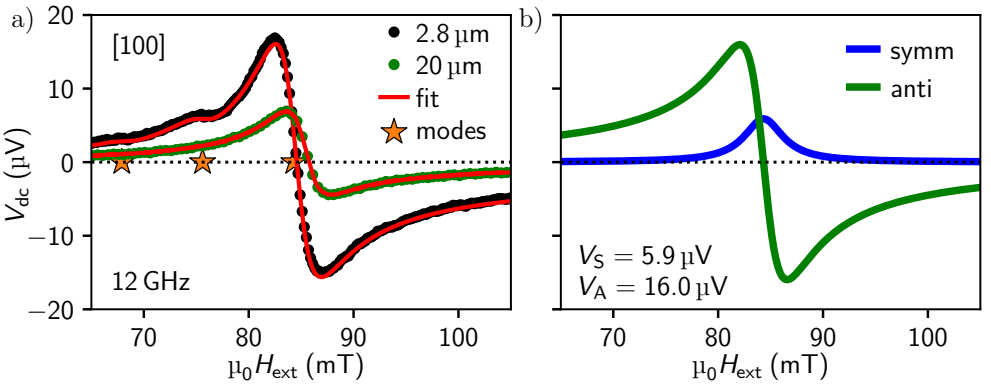

Figure 5.4: a) Typical dc-voltage measurement for a 2.8 and 20 µm wide stripe detected by SOT-FMR technique as a function of applied external field. The two spectra are recorded at 12 GHz and at a field angle of 5° with a rf-current flow along the [100] axis. b) The fitted curve consists of a symmetric and an anti-symmetric curve with the two voltage magnitudes $V_{S,A}$.

5.2 Electrical detection principle

In the following, all measurements are carried out on stripes with a current-induced SOT-FMR geometry. Thin aluminium bonds between the chip carrier and sample provide a direct injection of a rf-current, see Fig. 5.1(b). As a recap, a dc-voltage builds up along the device due to rectification, which can be picked up by two bias tees before and after the sample holder in the rf-circuit. The recorded signal during a magnetic field sweep can be decomposed into a symmetric and anti-symmetric Lorentzian line shape. The important quantities, as the resonance field H_{res}, linewidth ΔH, symmetric and anti-symmetric voltage amplitudes $V_{\mathrm{S,A}}$, are derived for a fixed rf-frequency, -power and magnetic field angle.

Fig. 5.4(a) shows two measurements on a 2.8 µm (black dots) and a 20 µm (green dots) wide Fe stripe. Both devices are patterned along the [100] axis, where the angle for an applied magnetic field is set to zero along this direction. Here, a microwave signal of 12 GHz with 23 dBm output power is applied at a field angle of $\phi_H = 5°$ through a 100 µm long stripe in both cases. Obviously, the narrow stripe experiences a larger current density, which leads to a higher signal amplitude. The spectra of the 20 µm wide stripe comprises a single mode, which is known as the FMR mode and conforms very well with the fit by a single Lorentzian function. In contrast, a pronounced dip towards lower fields is observed in the data of the 2.8 µm wide Fe stripe. The reduction of the stripe width causes a shift of higher spin wave modes down to lower magnetic fields and away from the first mode. The thickness-to-width ratio explains this shift of higher modes if the width gets smaller than ten micrometers for a 3.5 nm thin Fe film. Nevertheless, the received dc-voltage can be fitted by a combination of two additional Lorentzian curves. The resulting fitting curve

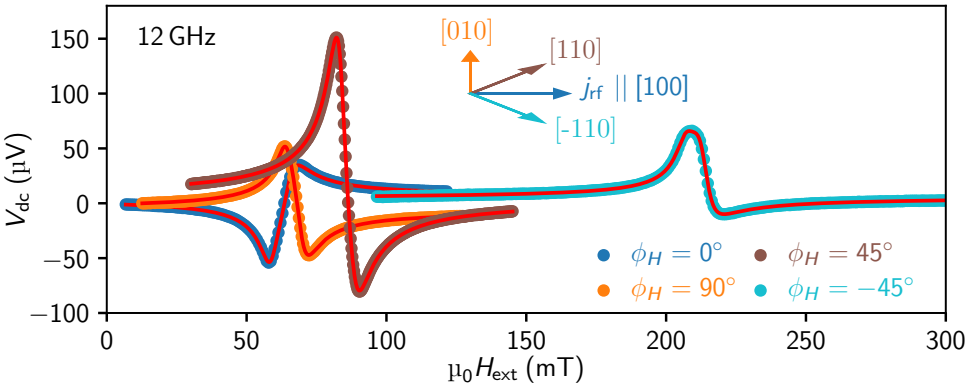

Figure 5.5: Four voltage spectra at different magnetic field angles ϕ_H are recorded for a [100] patterned device with an rf-current flow in the same direction. The origin of the difference in resonance field H_{res} is based on the anisotropy energy along the four crystallographic axes of GaAs(001).

can be decomposed into a symmetric (blue line) and anti-symmetric (green line) Lorentzian, where both amplitudes $V_{\mathrm{S,A}}$ are extracted as shown in panel (b).

5.3 Calculation of magnetization angle and susceptibility

In this section, the influence of the anisotropy fields on the magnetization dynamics is examined, which is crucial for the calculation of the spin-orbit field later. For this reason, a closer look is taken on the detected dc-voltage spectra along the four main crystallographic axes, since the Fe/GaAs(001) system exhibits large anisotropy fields.

Fig. 5.5 shows four measurements for a [100] patterned sample, where the magnetic field is applied along the four main crystallographic axes of GaAs(001). Evidently, the resonance field H_{res} depends on the magnetic field angle ϕ_H due to the crystalline anisotropy in the iron and varies in a wide field range between 60 to 220 mT. The hard axis points along [-110] and shows the largest H_{res} due to the pronounced uniaxial anisotropy. The four-fold term causes two easy axes along the [100] and [010] directions. Overall, the combination of both uniaxial and four-fold anisotropies leads to a pronounced hard axis along [-110] and two easy axes in [100] and [010] direction, introduced in Sec. 2.4.1. Notably, [110] is the easy axis of the uniaxial anisotropy, which is shifted upwards in fields by the four-fold contribution and exhibits the highest signal amplitude.

The measurements can be expanded to a full angle rotation in steps of 2° for an adequate resolution. The left side of Fig. 5.6 visualizes the rectified dc-voltage mapped as a function of H_{ext} and magnetic field angle ϕ_H. Notably, large amplitudes are located around the [100] and [010] easy axes compared to the signal strength near the hard axis in [-110] direction. The distribution

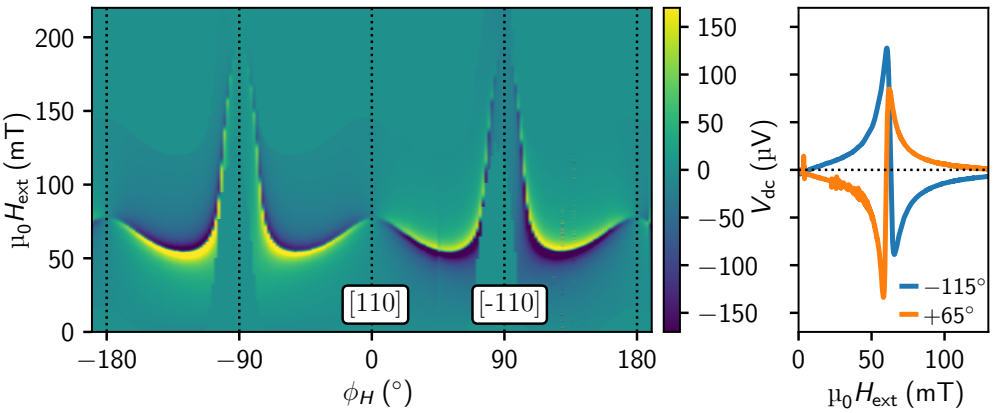

Figure 5.6: Left: The measured dc-voltage spectrum is plotted in colorcode with the resonance field and the magnetic field angle. The color indicates the amplitude of the signal, which changes sign between negative and positive applied magnetic fields angles. Right: Two voltage spectra shifted by 180° show the sign change of the Lorentzian line.

of the magnetic field angle is not uniform since the region around the hard axis is smaller compared to a pronounced valley for [100] and [010]. This can be explained by the dragging effect, which occurs for materials like Fe with a large anisotropy. The magnetization tends to align with the easy axis by saving crystallographic energy, whereas the magnetization is drawn away along the hard axis. This issue makes it necessary to evaluate the data with the magnetization angle. A sign change between negative and positive magnetic fields can be observed in the Lorentzian lineshape due to the sign change of magnetic field angle. This is highlighted on the right side of the figure by two voltage spectra, which are shifted by 180°.

The magnetization angle ϕ_M has to be calculated for every field angle ϕ_H, which is realized by minimizing the anisotropy energy terms from Eq. (2.4). This results with some trigonometry to [86]

$$E_{\mathrm{ani}} = -H_{\mathrm{res}}\cos(\phi_M - \phi_H) - \frac{H_4^{\parallel}}{16}\left[3 + \cos(4\phi_M)\right] - \frac{H_{\mathrm{uni}}^{\parallel}}{2}\cos^2(\phi_M - \phi_{\mathrm{uni}}), \quad (5.2)$$

with a uniaxial angle ϕ_{uni}. The magnetization angle ϕ_M is derived by fitting the angular dependence of H_{res} with the anisotropy fields and the effective

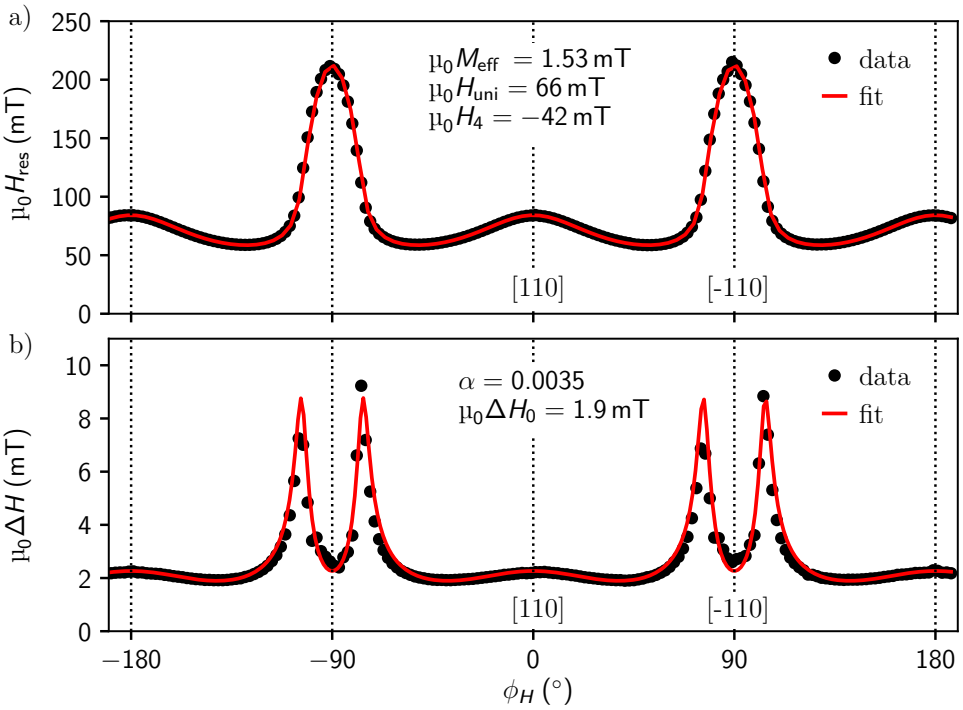

Figure 5.7: a) The resonance field as a function of magnetic field angle can be fitted to obtain the effective magnetization and the uniaxial and four-fold anisotropy fields. This is realized by minimizing the anisotropy energy, where the magnetization angle is first derived due to the dragging effect from the large anisotropy in Fe. b) The Gilbert damping parameter and the linewidth offset can extracted from a fit of the angular dependence of the linewidth ΔH.

magnetization as free parameters. A calculated resonance field $H_{\mathrm{res}}^{\mathrm{cal}}$ is obtained for every angle ϕ_M at 12 GHz. The procedure is the following: a least-squares algorithm minimizes the difference between measured and calculated resonance field by changing the two anisotropy fields and the effective magnetization until a global minimum is found for all magnetic field angles.

Fig. 5.7(a) shows the angular dependence of H_{res} together with the fitted parameters of $\mu_0 M_{\mathrm{eff}} = 1.53\,\mathrm{T}$, $\mu_0 H_{\mathrm{uni}} = 66\,\mathrm{mT}$ and $\mu_0 H_4 = -42\,\mathrm{mT}$. Both anisotropy fields are in the range of previously determined values by full-film FMR except the effective magnetization showing a large deviation. This issue can be explained by additional demagnetization fields due to the confinement in the fabrication process, where an elongated FM film is patterned into a narrow stripe. The susceptibility χ from Eq. (2.38) and (2.45) is derived as follows: for every angle ϕ_M, the susceptibility is calculated for a wide range of magnetic fields H' around the derived resonance field $H_{\mathrm{res}}^{\mathrm{cal}}$. The resulting curve can be decomposed into a real and imaginary part. The full width at half maximum of the resulting anti-symmetric Lorentzian lineshape corresponds to the linewidth

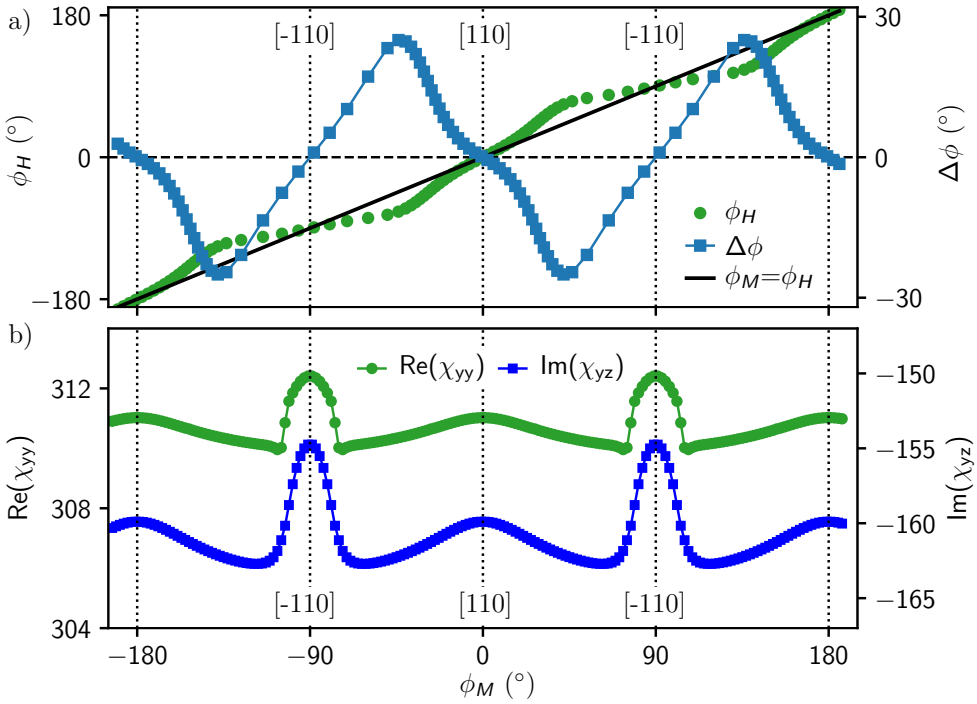

Figure 5.8: a) The applied magnetic field angle ϕ_H is plotted as a function of the calculated magnetization angle ϕ_M (green). There is only a concordance between both angles at the easy and hard axes of the uniaxial anisotropy. The deviation is up to 30° along the [100] and [010]. A linear dependence (black) and the angle difference (blue) highlight this issue. b) The calculated susceptibilities $\mathfrak{Re}(\chi_{y'y'})$ and $\mathfrak{Im}(\chi_{y'z'})$ relate to the in-plane and out-of-plane contributions. Both sets of data show almost the same angular dependence, however, differ in sign and magnitude.

ΔH. The magnitudes of the real and imaginary part at a particular angle ϕ_M leads to the susceptibility $\mathfrak{Re}(\chi_{y'y'})$ and $\mathfrak{Im}(\chi_{y'z'})$ of the individual diagonal and off-diagonal elements, respectively. Fig. 5.7(b) shows the angular dependence of the linewidth, where a least-sqaure algorithm minimizes the difference between measured and calculated ΔH by changing the damping parameter and the linewidth offset. Thereby, a Gilbert damping of $\alpha = 0.0035$ is received together with a linewidth offset of $\Delta H_0 = 1.9\,\mathrm{mT}$ due to inhomogeneous broadening. The two parameters are used to classify the wafer quality and to confirm a proper growth of the magnetic layer.

Fig. 5.8(a) displays the calculated magnetization angle ϕ_M against the field angle ϕ_H (green), where a black line indicates the case for $\phi_M = \phi_H$. The difference $\Delta\phi$ between both angles reaches values up to 30° (blue) along the [100] and [010] directions due to the dragging effect. In the other two crystallographic directions, the difference is zero since the magnetization points along the easy and hard axes of the uniaxial anisotropy, respectively. In Fig. 5.8(b), the *ip* and *oop* susceptibilities $\mathfrak{Re}(\chi_{y'y'})$ and $\mathfrak{Im}(\chi_{y'z'})$ are derived which exhibit the same behavior in terms of ϕ_M but differ in magnitude and sign.

5.4 Determination of spin-orbit fields by SOT-FMR

Next, the derived magnetic quantities and voltage amplitudes are assembled in order to determine the spin-orbit fields in the Fe/GaAs(001) heterostructure. The SOFs are determined by a careful analysis of the normalized voltage magnitudes as a function of the angular magnetization angle ϕ_M. The procedure will be explained in detail for the in-plane part with the anti-symmetric voltage and repeated for the out-of-plane case. All samples are glued on the holder in such way, that the stripe axis aligns with the external field at an angle of $\phi_H = 0°$. This defines the current in the same direction and the sample labeling is addressed by the crystallographic axes along the stripe direction. All measurements are carried out at room temperature and at magnetic field angles between -200 and +200° in steps of 5°. The rf-frequency is fixed to 12 GHz with an rf-output power of 23 dBm if nothing else is stated. The current flow through the sample is calibrated by the bolometric method, introduced in Sec. 3.8.

5.4.1 In-plane SOFs

The anti-symmetric voltage amplitude is linked to the in-plane spin-orbit fields given in Eq. (3.19). The *ip*-related voltage magnitude V_A is normalized by the real part of the diagonal component of the susceptibility $\mathfrak{Re}(\chi_{y'y'})$ and the AMR voltage $V_\mathrm{AMR} = I\Delta R/(2M_\mathrm{S})$. For every sample, V_AMR is individually derived with the calibrated current and anisotropic magneto resistance ΔR from Eq. (3.6). As an example for a [110] device, values of $\Delta R = 10.0\,\Omega$, $I_\mathrm{rf} = 1.80\,\mathrm{mA}$ and $\mu_0 M_S = 2.1\,\mathrm{T}$ are used.

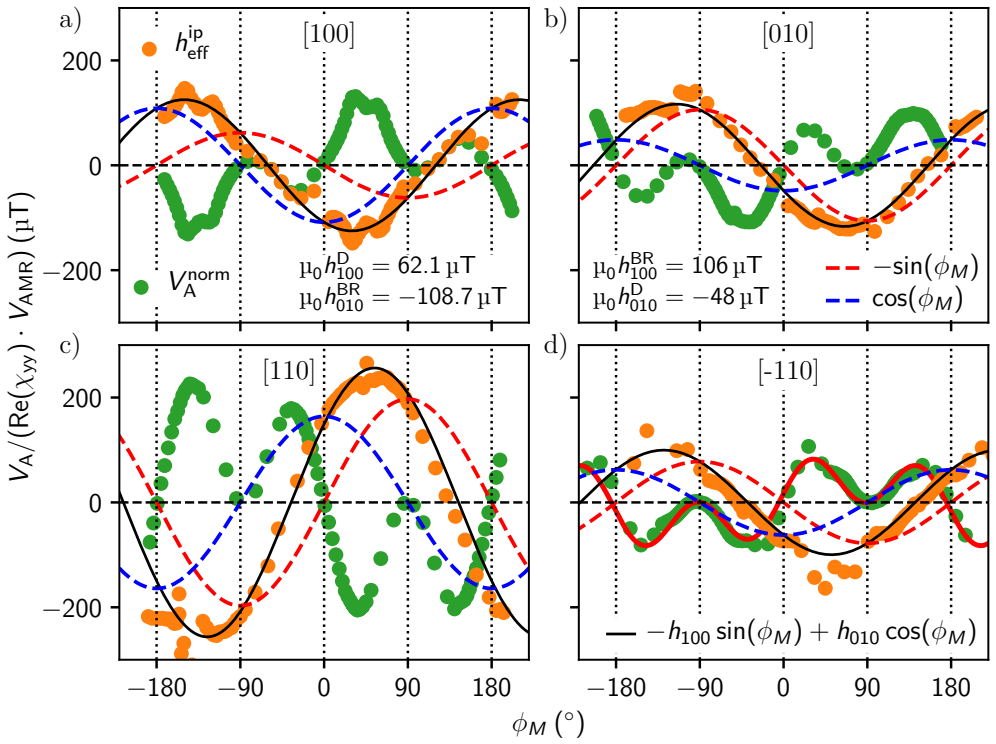

Figure 5.9: The normalized anti-symmetric voltage (green dots) is plotted as a function of magnetization angle ϕ_M for the four main crystal axes of GaAs(001). The orange data points represent voltage dependence without the $\sin(2\phi_M)$-term. The current flow is along the stripe in the marked direction at $\phi_M = 0°$. The two devices along [100] (a) and [010] (b) exhibit the same magnitude but different sign. The largest amplitude is obtained in the [110] (c) sample and the smallest along [-110] (d). The blue, red and black lines are the cosine, sine and combination of the two functions extracted from the orange data points.

Fig. 5.9 shows the normalized voltage $V_{\mathrm{A}}^{\mathrm{norm}}$ (green dots) as function of the magnetization angle ϕ_M along four crystal directions of GaAs(001). Comparing the magnitudes in the four panels, the [110] device exhibits the largest amplitude, whereas the [-110] stripe shows the lowest value. This is already predicted in Fig. 2.5 due to an amplified or suppressed spin-orbit coupling along these two directions. For [100] and [010], the magnitudes are similar, which can be explained by the shared easy axis. At $\phi_M = 0$ and thus the current collinear with magnetic field ($\mathbf{I} \parallel \mathbf{H}_{\mathrm{ext}}$), the voltage drops to zero in all cases, since the AMR is minimal in the microwave frequency range. This issue can be understood by regarding the contributing components of the precessional motion $\Delta\mathbf{m}_{y,z}$ with respect to the current along the stripe direction. If the current and $\Delta\mathbf{m}_{y,z}$ are oriented perpendicular to each other, the detected dc-voltage drops to zero.

The angular dependence is governed by a combination of a $\sin(2\phi_M)$ contribution together with a $\sin(\phi_M)$- and a $\cos(\phi_M)$-function. The first corresponds to the induced AMR effect in Eq. (3.16), while the latter two terms originates

Axis	c	term
[100]	-1	$\sin(2\phi_M)$
[010]	1	$\sin(2\phi_M)$
[110]	1	$\cos(2\phi_M)$
[-110]	-1	$\cos(2\phi_M)$

Table 5.1: Dependence of the pre-factor c and the trigonometric function for the main four crystallographic axes to be calculated for the SOFs [8].

from the spin-orbit fields, which leads to unequal amplitudes of both maxima and minima. This can be summarized to the expression [88]

$$V_{\mathrm{A}}^{\mathrm{norm}} \approx c \cdot \sin(2\phi_M) \cdot \left[-h_{100}\sin(\phi_M) + h_{010}\cos(\phi_M)\right], \tag{5.3}$$

with a pre-factor c and the trigonometric functions. Here, two spin-orbit fields h_{100} and h_{010} are introduced. These fields are oriented with respect to the current and stripe direction. The sign or pre-factor c of the $2\phi_M$-dependent term in Eq. (5.3) is different along the four crystallographic axes of GaAs(001), which is summarized in Tab. 5.1 from [8]. For a [100] stripe, the normalized voltage reads

$$V_{\mathrm{A}}^{\mathrm{norm}} = \frac{V_{\mathrm{A}}^{[100]}}{\mathfrak{Re}(\chi_{y'y'}) \cdot V_{\mathrm{AMR}}} = -\sin(2\phi_M)\left[-h_{100}^{\mathrm{ip}}\sin(\phi_M) + h_{010}^{\mathrm{ip}}\cos(\phi_M)\right]. \tag{5.4}$$

An effective in-plane field $h_{\mathrm{eff}}^{\mathrm{ip}}$ is introduced by dividing the normalized voltage $V_{\mathrm{A}}^{\mathrm{norm}}$ by the $\sin(2\phi_M)$ term. This effective field is also shown in Fig. 5.9 as orange dots. The magnitude $h_{\mathrm{eff}}^{\mathrm{ip}} = 125.2\,\mu\mathrm{T}$ is extracted by a fit (black line) of the combination of a sine and cosine function mentioned earlier. The maximum is located at roughly 60° with respect to the [100] direction and thus corresponding to a dominant sine contribution.

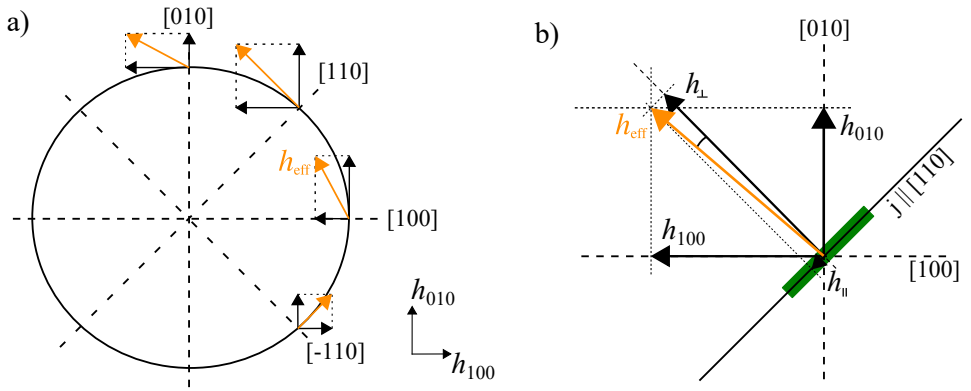

Figure 5.10: a) Sketch of the in-plane SOFs for the main four crystallographic directions. The sign of the fields dictates the counter-clockwise rotation of the SOFs. b) Calculation of the parallel and perpendicular SOFs with respect to the stripe direction for a [110] patterned device.

In case of a [100] and [010] oriented stripe, the Bychkov-Rashba- and Dresselhaus-like SOFs can be assigned to the perpendicularly and parallelly oriented SOF with respect to the stripe or equally the current direction, respectively. The Rashba SOF is related in both cases to the sine (red dashed line) and the Dresselhaus field to the cosine (blue dashed line) function. The formerly introduced fields h_{100}^{ip} and h_{010}^{ip} are swapped between the two axes since both fields are linked to the crystallographic axes. For the [100] patterned stripe, see panel (a), a Dresselhaus-like field of $h_{100,\parallel}^{\mathrm{D}} = -62.1\,\mu\mathrm{T}$ and a Bychkov-Rashba-like SOF of $h_{010,\perp}^{\mathrm{BR}} = 108.9\,\mu\mathrm{T}$ are found. This is also valid for the [010] stripe, where the two SOFs of $h_{010,\parallel}^{\mathrm{D}} = -48.6$ and $h_{100,\perp}^{\mathrm{BR}} = 106.1\,\mu\mathrm{T}$ are extracted. However, this procedure is no longer possible along the other two remaining axes due to a collinear orientation of both Bychkov-Rashba and Dresselhaus fields, see Fig. 2.4. Nevertheless, the data can be fitted by the former combination of a sine and cosine function in order to determine the effective fields.

Fig. 5.10(a) visualizes the fitted in-plane SOFs h_{100}^{ip} and h_{010}^{ip} along the four GaAs(001) axes with the resulting effective fields. The dominant Rashba fields for the [100] and [010] axes tilt $h_{\mathrm{eff}}^{\mathrm{ip}}$ at an angle of about 60° away from the current direction. In case of [110] and [-110], the angle is roughly 90° with respect to the stripe direction. This corresponds to a dominant perpendicular field in all devices and confirms the calculated two-fold distribution of the spin-orbit coupling as the superposition of two vector fields in Fig. 2.5(a).

Besides, it is possible to determine the parallel and perpendicular oriented SOFs for the [110] and [-110] devices with respect to the stripe direction. Fig. 5.10(b) sketches the calculation of the SOFs for a [110] patterned sample. With the help of the three formerly derived fields h_{100}^{ip}, h_{100}^{ip} and $h_{\mathrm{eff}}^{\mathrm{ip}}$, the parallel and perpendicular fields can be obtained to $h_{\parallel}^{\mathrm{ip}} = 23.2\,\mu\mathrm{T}$ and $h_{\perp}^{\mathrm{ip}} = 255.3\,\mu\mathrm{T}$ with some trigonometry. For [-100], the spin-orbit fields are $h_{\parallel}^{\mathrm{ip}} = 17.3\,\mu\mathrm{T}$ and $h_{\perp}^{\mathrm{ip}} = 69.6\,\mu\mathrm{T}$. The perpendicular field is about eleven ([100]) and four ([-

axis	$h_{\parallel}^{\mathrm{ip}}$	$h_{\perp}^{\mathrm{ip}}$	$\lvert h_{\perp}^{\mathrm{ip}}/h_{\parallel}^{\mathrm{ip}}\rvert$	$h_{\mathrm{eff}}^{\mathrm{ip}}$	j_{rf}	$h_{\mathrm{eff}}^{\mathrm{ip}}/j_{\mathrm{rf}}$
	(μT)	(μT)		(μT)	(10^{11} A/m^2)	(10^{-15} Tm^2/A)
[100]	-62.1	108.7	1.8	125.2	1.33	0.94
[010]	-48.6	106.1	2.2	116.7	1.62	0.72
[110]	-23.2	255.3	11.0	256.4	1.80	1.39
[-110]	-11.3	99.1	8.9	99.7	1.98	0.50

Table 5.2: The summarized in-plane SOFs are determined by fitting the normalized anti-symmetric voltage with the angular magnetization angle dependence for the four crystallographic directions of GaAs(001). The current in the sample is calibrated for each device individually with the bolometric method. The error from the fit is less than 4% and not considered in the following.

110]) times larger than the parallel ones. This matches very well to the more dominant perpendicular distribution in the other two samples. Obviously, the effective field is larger along [110] than [-110], however, both fields are roughly perpendicular to the current direction with a deviation of about 5°.

The three derived fields for the individual axes are collected in Tab. 5.2 together with the calibrated current density for each device. The Bychkov-Rashba field dominates the spin-orbit interaction by a factor of about two, since $h_{\perp}^{\mathrm{ip}}$ is roughly two times larger than $h_{\parallel}^{\mathrm{ip}}$ for the [100] and [010] devices. For the [100] and [010] oriented stripes, the magnitudes of $h_{\mathrm{eff}}^{\mathrm{ip}}$ are almost equal as expected from theory and Fig. 2.5b). Obviously, the magnitude of the stripe [110] is 2.5 times larger than the [-110] stripe, since the in-plane fields are amplified in the first and reduced in the latter case. The calculated SOFs are plotted in Fig. 2.5(a), where the lowest amplitude of the two-fold anisotropy is located at [-110]. Finally, the effective fields can be divided by the current densities, where an even more pronounced distribution is revealed. An average value of $h_{\mathrm{eff}}^{\mathrm{ip}}/j = (0.91 \pm 0.31) \cdot 10^{-15}\,\mathrm{Tm^2/A}$ is found, which matches very well to $0.8 \cdot 10^{-15}\,\mathrm{Tm^2/A}$ from published results for the same material system [8].

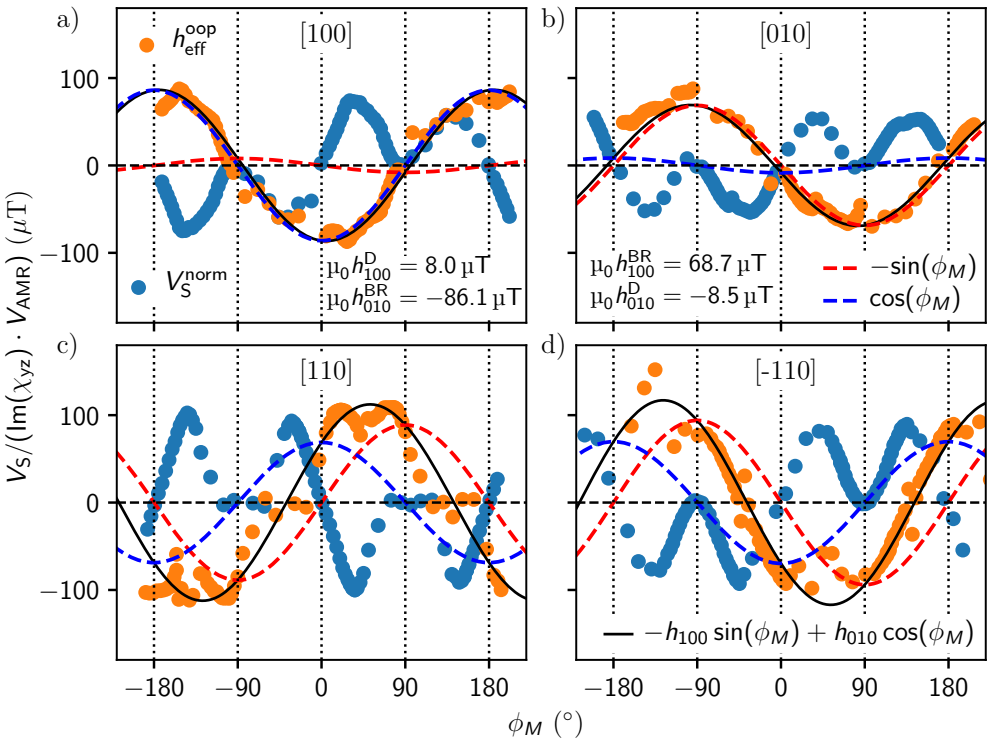

Figure 5.11: The normalized symmetric voltage (blue) is plotted against the magnetization angle ϕ_M for current along all four crystal axes. The magnitude of the effective field (orange dots) is derived by a fit of a sine and cosine function which corresponds to the $-h_{100}$ and h_{010} SOFs, respectively. The blue, red and black lines are the cosine, sine and combination of the two functions extracted from the orange data points.

5.4.2 Out-of-plane SOFs

The symmetric voltage can be determined by the same procedure in order to evaluate the out-of-plane SOFs. For this case, the symmetric amplitude V_S is normalized by the imaginary part of the off-diagonal susceptibility $\mathfrak{Im}(\chi_{y'z'})$ and the AMR voltage. An expression for a [100] device from Eq. (3.18) reads

$$V_S^{\text{norm}} = \frac{V_S^{[100]}}{\mathfrak{Im}(\chi_{y'z'}) \cdot V_{\text{AMR}}} = -\sin(2\phi_M)\left[-h_{100}^{\text{oop}}\sin(\phi_M) + h_{010}^{\text{oop}}\cos(\phi_M)\right] \tag{5.5}$$

with the individual pre-factor c and the trigonometry term from Tab. 5.1.

Fig. 5.11 shows the normalized voltage V_S^{norm} (blue dots) for the four crystallographic directions. Again, the normalized voltage can be divided by the $2\phi_M$-dependent term in order to remove the AMR contribution. The obtained effective field $h_{\text{eff}}^{\text{oop}}$ (orange dots) can be fitted by the combination of a sine and cosine function. Thereby, for the [100] sample the two spin-orbit fields $h_{100,\parallel}^{\text{oop}} = 8.0\,\mu\text{T}$ and $h_{010,\perp}^{\text{oop}} = -86.1\,\mu\text{T}$ are obtained as the amplitude of the fitted cosine (blue) and sine (red) function. The magnitude of the effective field is $h_{\text{eff}}^{\text{oop}} = 86.5\,\mu\text{T}$ and the maximum is located near $\phi_M = 0°$, which means a dominant sine function and perpendicular SOF. This corresponds to a ten times larger h_{010}^{oop} compared to h_{100}^{oop}. As in the in-plane case, the parallel and perpendicular fields can be derived for the out-of-plane fields. The parallel and perpendicular fields can be derived by repeating the former trigonometry fitting procedure. For [110], we found values of $h_{\parallel}^{\text{oop}} = 14.3\,\mu\text{T}$ and $h_{\perp}^{\text{oop}} = 68.9\,\mu\text{T}$ together with $h_{\parallel}^{\text{oop}} = 17.3\,\mu\text{T}$ and $h_{\perp}^{\text{oop}} = 69.6\,\mu\text{T}$ for a [-110] device. Thus, the orthogonally oriented field is always about four to five times larger than the parallel field. This was also observed for the in-plane part.

The three fields for each of the four devices are collected in Tab. 5.3 together with the individual calibrated current densities. Obviously, the dominating contribution is again the perpendicular SOF, which is about a factor of roughly ten larger than the parallel SOFs for [100] and [010] and about a four to five times larger in case of [110] and [-110]. For the [010] device, the value of $h_{\perp}^{\text{oop}}$ does not fit to the rest of the data, since a similar values should be expected

axis	$h_{\parallel}^{\text{oop}}$	$h_{\perp}^{\text{oop}}$	$\lvert h_{\perp}^{\text{oop}}/h_{\parallel}^{\text{oop}}\rvert$	$h_{\text{eff}}^{\text{oop}}$	j_{rf}	$h_{\text{eff}}^{\text{oop}}/j_{\text{rf}}$
	µT	µT		µT	$10^{11}\,\text{A/m}^2$	$10^{-15}\,\text{Tm}^2/\text{A}$
[100]	8.0	-86.1	10.7	86.5	1.33	0.65
[010]	-8.5	68.7	8.1	69.2	1.62	0.43
[110]	-14.3	68.9	4.8	112.3	1.80	0.62
[-110]	-17.3	-69.6	4.0	117.0	1.98	0.59

Table 5.3: Summarized out-of-plane SOFs determined from the angular fitting procedure for all directions.

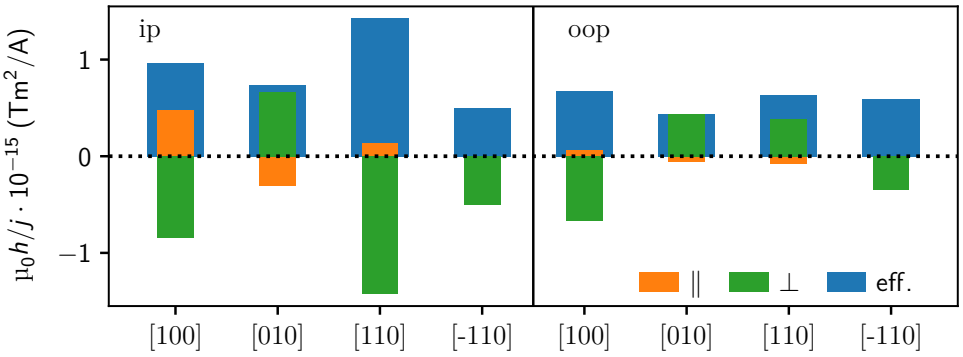

Figure 5.12: Spin-orbit fields normalized to the current density for the in-plane (left) and out-of-plane (right) fields along the four crystallographic axes.

due to the shared easy axis. The much lower $h_{\perp}^{\mathrm{oop}}$ leads to a smaller ratio and normalized effective field. For all devices, the resulting direction of the effective field is orthogonal to the stripe orientation. This is the cosine part h_{010}^{oop} for [100] and the sine part h_{100}^{oop} for a [010] device. Overall, the effective fields are shifted by about 5-8.5° from the perpendicular stripe direction as for the in-plane data.

The magnitude of the effective field $h_{\mathrm{eff}}^{\mathrm{oop}}$ shows a completely different behavior compared to the in-plane configuration. Both [110] and [-110] devices have larger magnitudes than the [100] and [010] directions. These converge to a mean value of $h_{\mathrm{eff}}^{\mathrm{oop}}/j = (0.57 \pm 0.09) \cdot 10^{-15}\,\mathrm{Tm}^2/\mathrm{A}$ after normalization with the individual current densities. The magnitude of the out-of-plane fields is still smaller than for the in-plane fields for all directions except for the [-110] axis.

5.5 Discussion of results

Fig. 5.12 shows a bar plot, which summarizes the derived results of all SOFs for the largest applied rf-current. A huge difference of the effective *ip* SOFs is observed for the different crystal directions due to the amplified or suppressed combination of Dresselhaus- and Bychkov-Rashba-like SOFs. The field $h_{\mathrm{eff}}^{\mathrm{ip}}$ along the two [100] and [010] orientations have equal magnitude since both devices have the same strength in spin-orbit coupling. The fields obtained for the [110] and [-110] axes are larger and smaller due to the mentioned sum or difference of the SOFs, respectively. The in-plane distribution is in perfect agreement to the theoretically predicted behavior with a strength ratio of $\alpha_{\mathrm{BR}}/\beta = 2$ of the Bychkov-Rashba and Dresselhaus coefficient, respectively. In all cases, a fit function with h_{100} and h_{010} is used with the adapted susceptibilities and parameters from the table. Further, the parallel and perpendicular fields are the same for a [100] device and swapped in the case of [010] since the stripe is rotated by 90°. The fields for [110] and [-110] are derived with the previously shown trigonometry. A cross correlation of the Dresselhaus- and

Bychkov-Rashba-like SOFs between the [100] and [010] direction is clearly seen as explained earlier. The perpendicular Bychkov-Rashba field dominates the in-plane SOFs in both devices by a factor of 1.8 and 2.2 in the [100] and [010] device, respectively. A much larger ratio of roughly ten is found along the last two directions, however, the two SOFs are collinear which makes it impossible to distinguish the two contributions. Overall, this leads to the conclusion that the interface-like SOF is mainly Rashba-like as already predicted in earlier work [8]. The right side in Fig. 5.12 shows the normalized *oop* SOF, which is more or less constant except for a much smaller value for the [010] sample which cannot be explained without any further experiments.

The *ip*/*oop* ratio between the effective fields is calculated to 1.45, 1.68, 2.28 and 0.85 for the crystal directions of [100], [010], [110] and [-110], respectively. In the following, the axes are always considered in this order. The distribution of this ratio is similar to the ip SOFs, since there the out-of-plane fields are more or less constant for all orientations. Interestingly, the sum of the first two and last two SOFs is exactly 3.13 in both cases. This indicates a strong connection between the two four-fold easy axes and the two uniaxial axes as expected. The SOFs of [110] and [-110] are enhanced and decreased by 0.72 from their mean value of 1.56. This is exactly the same as the average of [100] and [010].

A set of measurements for varying rf-output powers at 12 GHz are carried

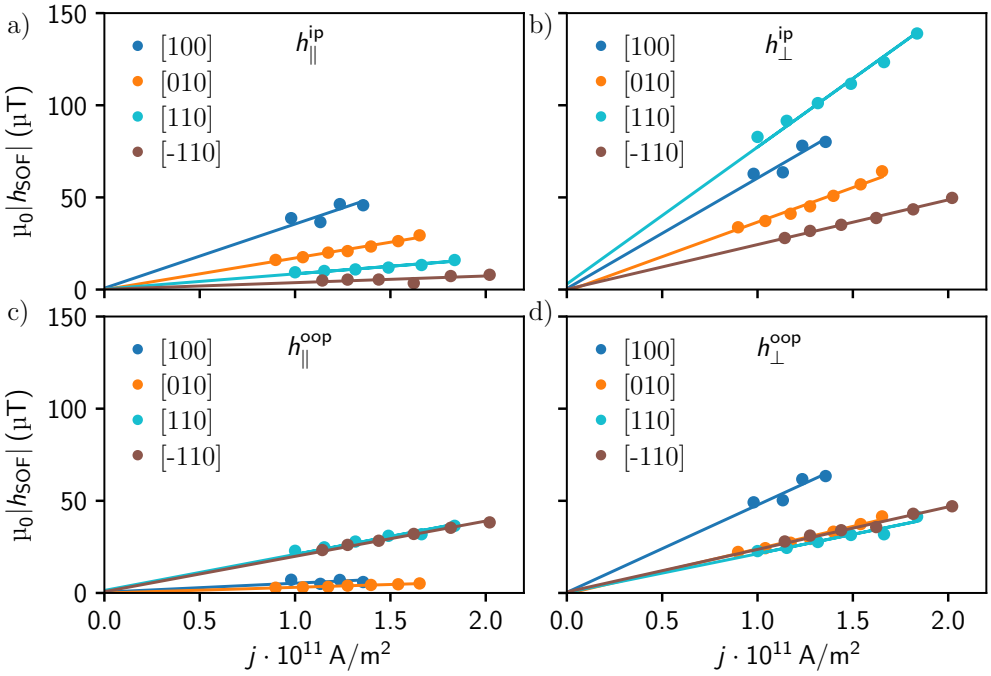

Figure 5.13: Derived spin-orbit fields for a set of different current densities for all four devices. The upper two panels correspond to in-plane and the lower two subplots to the out-of-plane fields. The parallel oriented SOFs are on the left side and the field perpendicular with respect to the stripe or current direction on the right side.

out in order to demonstrate the linear dependence of the SOFs on the current density. The spin-orbit fields are derived by the former method at least for four different powers along the four principal axes.

Fig. 5.13(a,b) show the absolute amplitude of the two in-plane fields and (c,d) for the two out-of-plane SOFs. All data sets agree perfectly with a linear dependence through the origin. The slope of the in-plane field is between $h^{\mathrm{ip}}/j_{\mathrm{rf}} = 0.036 - 0.35 \cdot 10^{-15}\,\mathrm{Tm}^2/\mathrm{A}$ between all devices, which was already observed in Tab. 5.2. Obviously, the largest slope is found along the [110] axis of $h_{\perp}^{\mathrm{ip}}/j_{\mathrm{rf}} = 0.74 \cdot 10^{-15}\,\mathrm{Tm}^2/\mathrm{A}$. The ratio between the perpendicularly and parallelly oriented $h^{\mathrm{ip}}/j_{\mathrm{rf}}$ is 1.7, 2.2, 9.0 and 6.7 along [100], [010], [110] and [-110], respectively. As expected, both [100] and [010] share the same value within the error bars, whereas the latter two are much larger. The amplitude of the in-plane fields agree well with previously reported measurements on the same material system [8]. A slightly higher $h^{\mathrm{SOF}}/j_{\mathrm{rf}} = 1.6 \cdot 10^{-15}\,\mathrm{Tm}^2/\mathrm{A}$ is found for a similar Fe(2 nm)/(Ga,Mn)As(20 nm) system in [89].

In panel (c), the slopes are split up between lower values for the [100] & [010] devices and larger ones for [110] & [-110]. This changes for the perpendicular case in d), when all values are located closely together except a much larger value for [100]. This inconsistency between the two configurations is unexpected and cannot be explained so far. The obtained slope ratios are 9.7, 7.9, 1.1 and 1.2 between perpendicular and parallel. This is opposite compared to the in-plane fields, where the first two directions are larger than [110] and [-110]. Nevertheless, the *oop* effective fields from Tab. 5.3 can be considered as constant within the error bars.

Overall, the magnitudes of in-plane spin-orbit fields are larger than the out-of-plane fields. A closer look can be taken on the individual *ip*/*oop* ratio of the two SOFs for each device. In the parallel case, the [100] direction has the largest ratio of 7.1 together with the [010] direction with a value of 5.6. This is quite different to values of only 0.4 and 0.2 for the [110] and [-110] directions, which correlates to the difference between the two easy axes and the other two direction. In contrast, the ratio of the perpendicular fields shows three scattered values around 1.3 and a much larger value of 3.5 for the [110] device due to the amplified SOFs in the in-plane case. Finally, the linear dependence of the SOFs on the current density is proven together with a proper interpretation of the obtained values along the different crystallographic axes.

In addition, the effective SOFs can be normalized with regard to the thickness of the ferromagnetic layer. Here, the [110] direction is taken into account with values of $h_{\mathrm{eff}}^{\mathrm{ip}}/j_{\mathrm{rf}} = 1.42$ and $h_{\mathrm{eff}}^{\mathrm{oop}}/j_{\mathrm{rf}} = 0.55 \cdot 10^{-15}\,\mathrm{Tm}^2/\mathrm{A}$ for the in-plane and out-of-plane normalized effective SOFs, respectively. The resulting value for the 3.5 nm thin Fe film is obtained to

$$h_{\mathrm{eff}}/j_{\mathrm{rf}} \cdot d_{\mathrm{FM}} = (0.2 - 0.5) \cdot 10^{-14}\,\frac{\mathrm{Tm}^2 \cdot \mathrm{nm}}{\mathrm{A}}. \tag{5.6}$$

Values with prefactors of $10^{-14}\,(\mathrm{Tm}^2 \cdot \mathrm{nm})/\mathrm{A}$ of other material systems are reported, as for example, 1.5 for CoFeB/Pt [11], 3.0 for Co/Pt [9], 2.7 for CoFeB/Ta [9, 106], 16.4 for CoNiPt/Mn [110] and 1.0 for Fe/(Ga,Mn)As [89].

6

Optical detection of spin-orbit fields in the Fe/GaAs system

Now, the same samples are investigated by the new optical approach to quantify SOFs. The magnetization dynamics are excited in the same way as for the electrical measurements. A TRMOKE microscope is used to detect the out-of-plane tilt of the magnetization, which is explained in Sec. 3.3. Due to the confinement by a narrow stripe, higher modes appear for lower externally applied fields and are well separated by equal distance in magnetic field. By mapping the Kerr signal as a function of lateral space coordinate and magnetic field, a 2D mode pattern occurs which can be reproduced by micromagnetic simulations. By changing the initial in-plane and out-of-plane SOFs of the simulations, both SOFs can be derived by an algorithm which tries to fit the measured pattern.

6.1 Static equilibrium change method

Before determining the spin-orbit fields with the help of standing spin waves (SSW), we try to determine the fields by the magnetometer technique intro-

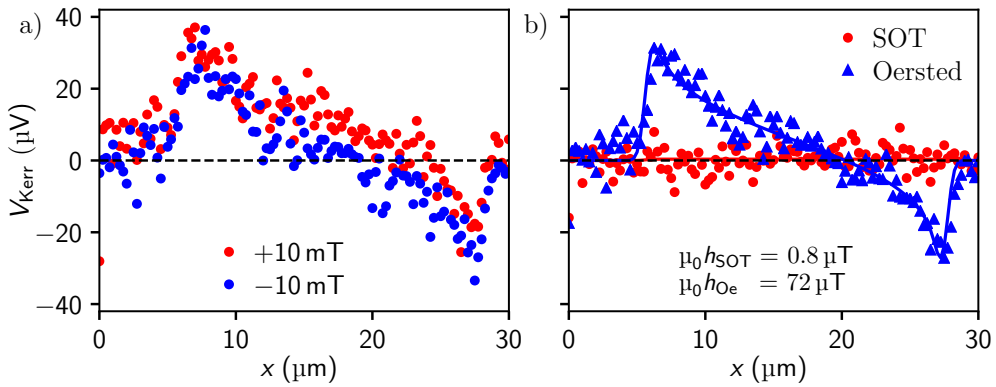

Figure 6.1: a) Static magnetization measurement for two oppositely applied fields of ±10 mT showing a mainly Oersted field dominated Kerr spectrum across the stripe. b) A negligible SOT signal is observed for a 20 µm wide stripe due to the large in-plane effective field originating from the Fe film which suppresses a detectable *oop* tilt of the magnetization.

duced in Sec. 3.6 and already utilized for the Py/Pt bilayers in Sec. 4.3. A $100\times20\,\mu m^2$ sample is fabricated to ensure a more detailed analysis across the stripe width. The magnetization is excited by an in-plane ac-current of several kHz which tilts the magnetization out-of-plane due to a damping-like torque. The resulting equation for the spin-orbit field is already given by Eq. (3.34) and (3.35) as

$$h_{\mathrm{SOT}} = \frac{V_{\mathrm{SOT}}}{\eta_{\mathrm{MOKE}}} = \frac{1}{\eta_{\mathrm{MOKE}}} \frac{h_{\mathrm{SOT}}}{H_{\mathrm{ext}} + M_{\mathrm{eff}}} \quad x_0 \leq y \leq x_0 + w. \tag{6.1}$$

The measurement is visualized in Fig. 6.1(a) where the Kerr signal is recorded during a line scan across the stripe. The process is repeated for two opposite magnetic fields of $\pm10\,\mathrm{mT}$ which are aligned parallel to the current and stripe direction. As seen in panel b), both voltages are either summed up to get the Oersted field contribution or subtracted for the SOT signal. The two resulting curves can be fitted simultaneously in order to obtain the spin-orbit field h_{SOT}. The Oersted field $h_z^{\mathrm{Oe}}(y)$ is calculated by Eq. (3.30) with the known ac-current and stripe width. Fig. 6.1(b) shows a room temperature measurement for a current density of $3.3 \cdot 10^{10}\,\mathrm{A/m^2}$ where a SOF of only $(0.8 \pm 0.5)\,\mu\mathrm{T}$ is found together with an Oersted field of $(72 \pm 0.5)\,\mu\mathrm{T}$. The small SOF can be explained by the strong in-plane magnetization of the Fe with a large M_{eff} contributing in Eq. (6.1). Thus, there is no measurable *oop* tilt of the magnetization which makes it impossible to extract h_{SOF} by this method.

6.2 Dynamic determination by standing spin waves - DE geometry

The excitation frequency is increased up to the GHz range where the magnetization can be stimulated in a more efficient way. Further, the magnetic

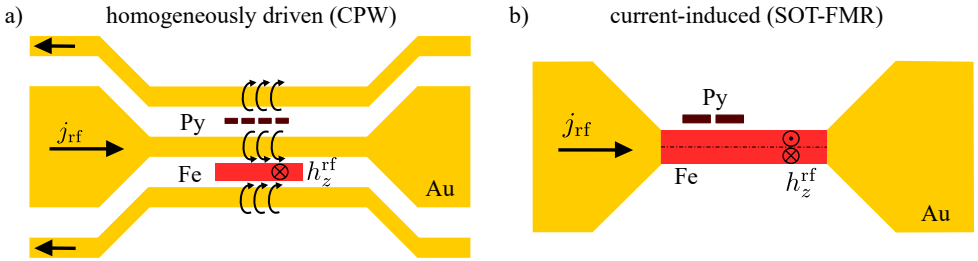

Figure 6.2: Two geometries are used, where the sample is either patterned in the gap of CPW (a) or attached to two bondpads (b). In the first case, the magnetization is driven by a homogeneous out-of-plane Oersted field. In the second geometry, the rf-current through the sample induces an Oersted field as well as spin-orbit fields from the interface. Small stripes of permalloy are added next to the Fe stripe to determine the correct rf-to-laser phase ψ.

precession in FMR leads to a larger signal-to-noise ratio and makes it easier to detect it optically. As introduced in Sec. 2.6, standing spin waves evolve in a narrow Fe stripe. The magnetic field is always applied parallel to the stripe and current direction. The wave vector **k** is perpendicular to the stripe due to the translational symmetry along the stripe and thus SWs in the Damon-Eshbach geometry are excited.

6.2.1 Sample layout

Fig. 6.2 sketches the two different sample layouts used in the following measurements. The first geometry is shown in panel a), where a $20\times2.8\,\mu m^2$ long stripe is placed in the gap of a co-planar waveguide by EBL. The CPW driving field is out-of-plane and homogeneous across the whole stripe width. In the second layout in displayed, in panel b), a $100\times2.8\,\mu m^2$ long stripe is attached to two bondpads for current injection, which induces an anti-symmetric Oersted field in the lateral stripe dimension in addition to two SOFs. These arise from the C_{2v}-interface of Fe/GaAs and act homogeneously on the in- and out-of-plane magnetization component. Small $10\times1\,\mu m^2$ permalloy wires are placed next to the Fe stripes in order to determine the phase between rf-excitation and laser pulses. The Py wire is kept short enough to avoid cross talk. Further, a relatively thick 20 nm Py film guarantees no additional modes and provides a good

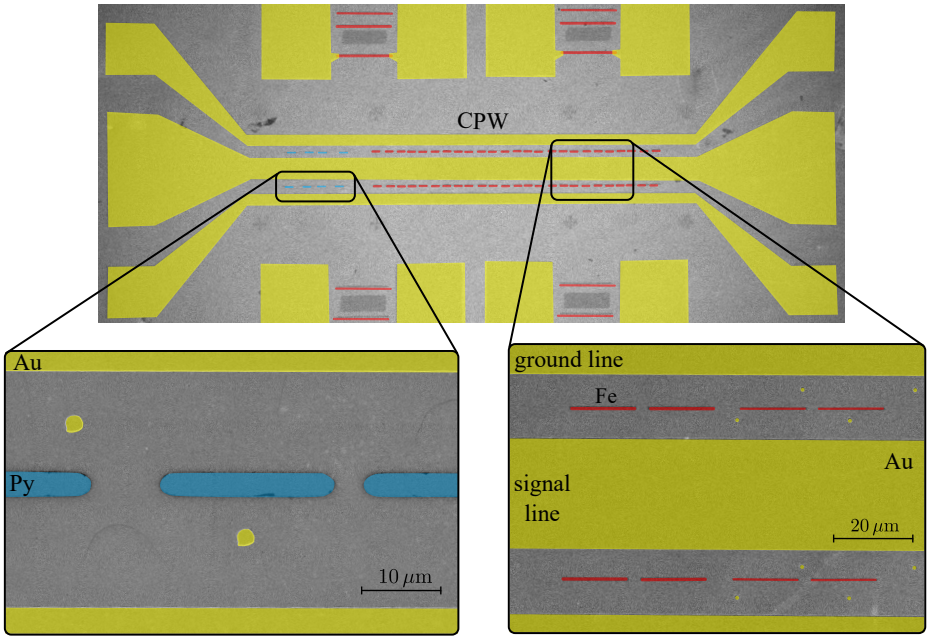

Figure 6.3: Detailed image of the CPW geometry reveals FM stripes in the gap of the CPW which can be excited by the homogeneous out-of-plane Oersted field.

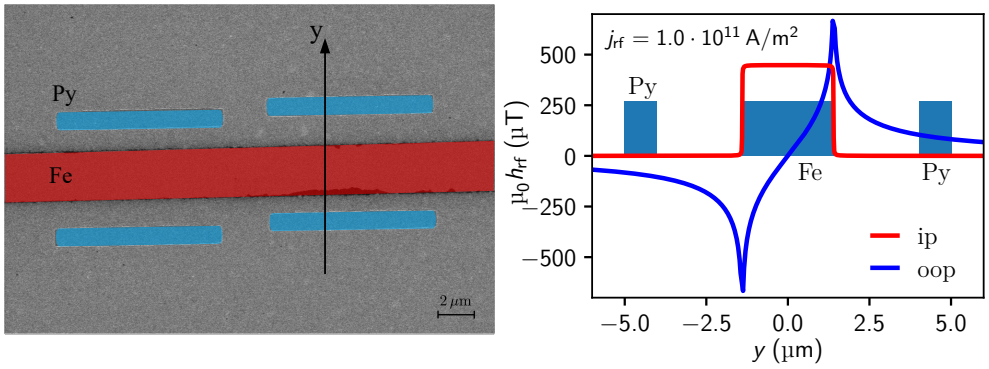

Figure 6.4: a) Several $10\times1\,\mu m^2$ Py wires are located next to the Fe stripe at a distance of about 1.2 µm by EBL. b) A current density of $1.0 \cdot 10^{11}$ A/m^2 generates *ip* and *oop* Oersted fields displayed across the stripe width. An *oop* field of 190-260 µT is reached at the position of the Py stripe. This field strength can be compared to a sample in the gap of a CPW [37].

signal strength.

Fig. 6.3 shows the Py (blue) and Fe(red) stripes in the gap of the CPW as a SEM image.

6.2.2 Phase determination

An important issue is the knowledge of the exact phase of the magnetization precession since it is crucial for the magnetization dynamics in the optical approach. An arbitrary phase in the TRMOKE setup, between the rf-generator and laser pulse, which is modified by cables and other microwave devices prevents a knowledge of the phase at the sample position. To circumvent this problem, the phase is determined in the following way: the Oersted field, created from the Fe stripe or CPW, excites the magnetization in the Py wire. In case of the CPW, the phase properties of the detected anti-symmetric Lorentzian is well-definded. It is known, that a homogeneous out-of-plane driving field in Py shows an anti-symmetric lineshape with a phase of $\psi = 0°$ [37]. This knowledge can then be transferred to determine the phase in the Fe stripe.

Fig. 6.4 shows both wires structured along the y axis where the Py wire is placed at a distance of 1.2 µm away from the iron wire. The rf-current through the Fe stripe creates an Oersted field which points out-of-plane at the position of the Py stripe and gains an additional phase of 90° due to a shift from *ip* to *oop*. The driving field strength in the Py element can be calculated by Biot-Savarts law where values up to 260 µT are achieved for a current density of $1.0 \cdot 10^{11}$ A/m^2. This is comparable to spin-pumping experiments with a CPW current density of $3 \cdot 10^9$ A/m^2 [37].

The driving phase can be determined by the spin wave spectroscopy mode of the TRMOKE microscope explained in Sec. 3.4.1. A laser beam, focused on the

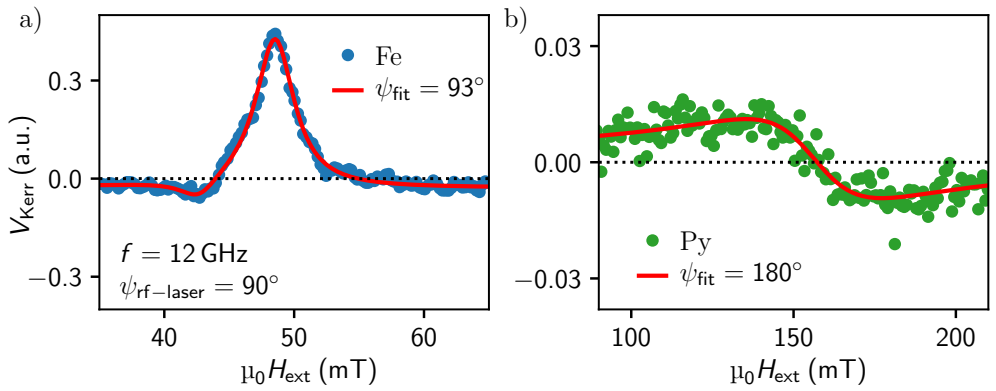

Figure 6.5: a) Recorded Kerr signal at the center of a Fe stripe for an initial rf-phase of $\psi = 90°$ illustrating a symmetric Lorentzian line shape with a fitted phase of 93°. b) Magnetic signal on the Py wire which is excited by the *oop* Oersted field from the rf-current in the Fe stripe. For the same ψ, an anti-symmetric Lorentzian with a fitted phase of 180° is obtained.

middle of the stripe of Py or Fe, leads to the Kerr signal during a steady increase of externally applied field. The rf-frequency, initial rf-laser phase, rf-output power and position are fixed for the whole recoding time. Fig. 6.5(a) shows the obtained Kerr voltage for iron at 12 GHz with a fixed initial phase of $\psi = 90°$. The line shape is almost purely symmetric and can be fitted to obtain a phase of 93°. Panel b) shows the magnetic response on the small Py wire as green data points for the same initial phase. The spectrum is completely different and shows an anti-symmetric Lorentzian with a fitted phase of $\psi = 180°$. The shift of 90° accords well with the change from an *ip* to *oop* driving field. Both

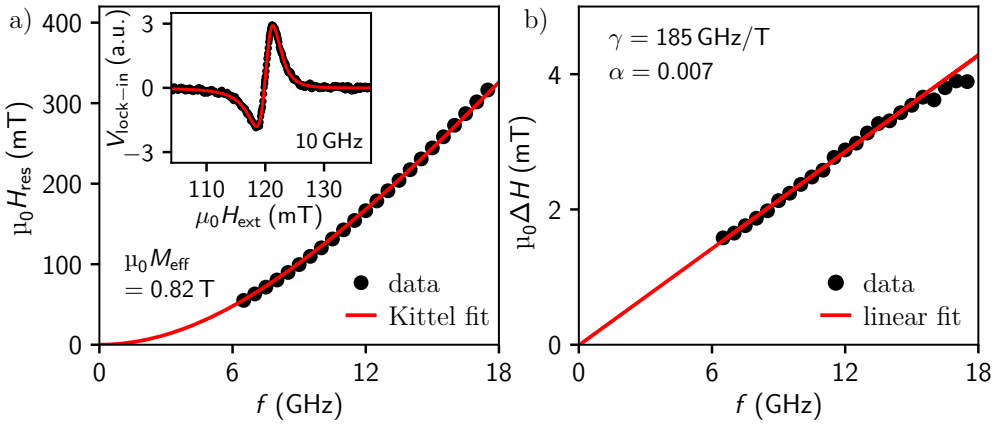

Figure 6.6: a) The frequency dependence of the resonance field of a Py(20 nm)/GaAs wafer can be well fitted by the Kittel formula. The inset shows an example of the measured anti-symmetric lock-in signal for a driving frequency of 10 GHz. b) The linewidth as a function of f is used to determine a Gilbert damping parameter of $\alpha = 0.007$ by a linear fit.

curves also reveal different amplitudes and field strengths of their resonance peaks. This is based on the smaller excitation efficiency from the Oersted field and the different magnetic properties of both materials.

Since the Py wire has not the expected linewidth, a piece of Py(20 nm)/ GaAs wafer grown in the same process step is investigated by full-film FMR. Fig. 6.6(a) shows a frequency dependence of the resonance field resulting in an effective magnetization of $\mu_0 M_{\text{eff}} = 0.82\,\text{T}$. This values indicates a good wafer quality since the saturation magnetization for Py is about 1.0 T. Fig. 6.6(b) displays a small Gilbert damping parameter of $\alpha = 0.007$ and a negligible offset by fitting the linewidth linearly as a function of frequency. This also hints at good magnetic properties of the used Py. The linewidth around 12 GHz is only about 2.5 mT, which is much smaller than observed in the optical measurements in the case before. Therefore, this cannot explain the broad linewidth of the Py wire. Some possible explanations could be the reduction of the dimension from a film to a narrow stripe, a non-homogeneous mode spectrum in the Py stripe or influences from the much thicker Py stripe (20 nm) compared to the etched Fe stripe (3.5 nm). Nevertheless, the initial phase is not so important for the experiments, since two 90° shifted phases provide the necessary information for determining the SOFs with two mode patterns. Moreover, the initial phase can be fitted by micromagnetic simulations, where any desired phase can be picked in the evaluation process.

6.2.3 Homogeneous excitation of SSWs

After defining the absolute phase of the GHz-laser system, the SSWs are created at first by a homogeneous out-of-plane field from a CPW. For symmetric reasons, this only allows to excite modes with even mode number with respect to the lateral stripe direction. The geometry is the same as before, see Fig. 6.2(a). The following measurements are carried out to check and verify this new approach before determining the spin-orbit fields. Further, it allows to determine important magnetic parameters, which are needed later for micromagnetic simulations.

6.2.3.1 Characterization of DE-CPW SSWs

As a reminder from Sec. 2.6.2, the precession of $\mathbf{m}$ in a confined stripe forms standing spin waves in y direction. There are only even modes allowed with odd mode numbers $n = 1, 3, 5, ...$ The anti-symmetric modes cannot be excited with a homogeneous driving field.

First, the mode spacing is investigated to ensure that neighboring modes can be distinguished and are well separated in magnetic field. For that purpose, the TRMOKE operates again in the spectroscopy mode where the laser beam records the Kerr signal at the center during a monotonic increase of applied

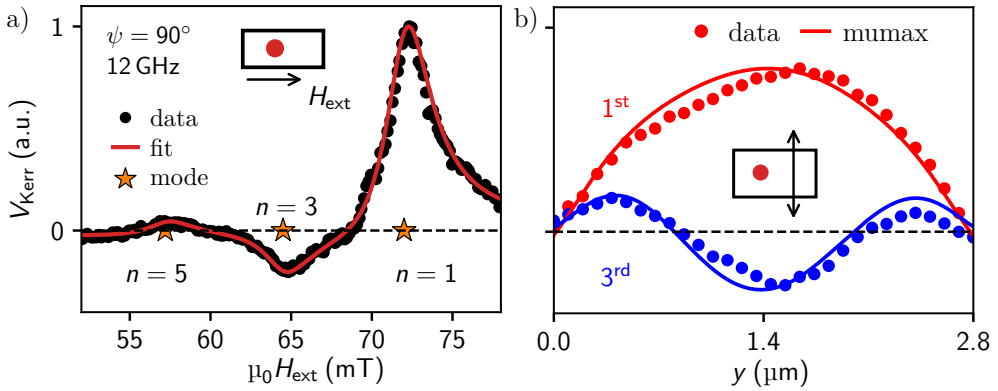

Figure 6.7: a) The recorded Kerr signal from the middle of a [110] oriented stripe sitting in the gap of a CPW can be fitted by three single Lorentzian line shapes to determine the position of the modes (orange stars). A spacing between neighboring modes of about 7.5 mT is found. Further, the linewidth of each mode is fitted to 1.5 mT which corresponds to a Gilbert damping parameter of 0.0036. b) A line scan across the stripe displays the Kerr signal of the first and third mode at the particular magnetic fields. The solid line indicates the calculated shape of both eigenmodes.

magnetic field similar as for the determination of the phase. Fig. 6.7(a) shows the Kerr signal for $\psi = 90°$, which can be fitted by three individual Lorentzian functions with three resonance fields corresponding to the first, third and fifth mode at 72, 64.5 and 57.2 mT, respectively. The gap between even modes is about 7.5 mT which is large enough for a well-defined separation of modes and a proper disentanglement in the experiments. It is noteworthy that for all three modes the same linewidth is assumed and the received ΔH from the fit is 1.5 mT. This relates to a Gilbert damping parameter of 0.0036, which is exactly the same as found in electrical measurements.

The SSWs can be displayed by a map of lateral space coordinate and magnetic field when the TRMOKE operates in the imaging mode, see Sec. 3.4.2. In contrast to the former method, the magnetic field is now fixed at a certain resonance field. The laser beam moves across the stripe in distinct steps with the

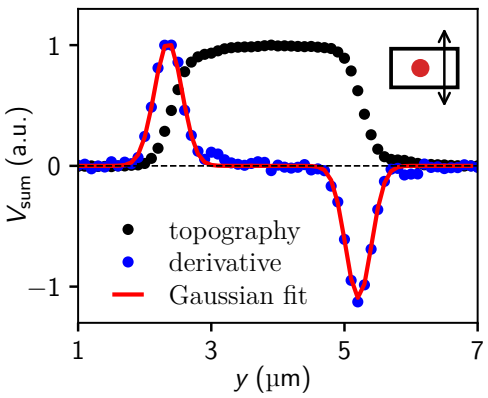

Figure 6.8: The topographic signal (black) shows the reflectivity of the sample with curved edges due to the finite spot of the laser beam. Therefore, the derivative of this signal (blue) is fitted by two Gaussian line shapes detecting both edges for later data analysis.

help of the piezo stage while both Kerr and topographic signals are recorded. Fig. 6.7(b) shows the Kerr voltage which exhibits one peak in the center region and two nodes at the edges of the first mode (shown in red). At lower field, the third mode appears (blue). The topographic signal is used to determine both edges of the stripe, which define a boundary in the pattern since the unimportant areas next to the Fe stripe contain no further information and increase the computational time for the simulation. Both edges on every single line scan are identified to eliminate drifts during a longer measurement time of typically several hours. This is realized in Fig. 6.8, where two Gaussian line shapes are fitted to the two peaks of the derivatives of the topographic signal. In addition, the Kerr signal was normalized with regard to the topography signal from the blank GaAs(001) wafer beside the stripe. Thereby, any changes in the laser beam intensity or sample reflectivity can be excluded.

The eigenmodes can be calculated by micromagnetic simulation which are displayed as solid lines in Fig. 6.7(b). Note, that a signal is observed at the position where the odd modes are expected. The second mode, for example, is not excited, however, a signal at this magnetic field is still observable. This comes from a linewidth broadening and the overlap of the first and third mode. Beside a little shift due to misalignment during sample fabrication, all data are in good agreement.

6.2.3.2 Mode pattern

The SW imaging mode in combination with a field-sweep is facilitated to map m_z along the width of the stripe, i.e. along the y axis. Fig. 6.9(a) visualizes the modes in a 2D pattern at a fixed phase of 90° and rf frequency of 12 GHz along a [110] patterned stripe where the color code denotes the Kerr signal strength. A piezo stage moves the sample under the microscope giving insight into the evolution of the eigenmodes with the change in magnetic field. After every scan at a fixed position on the stripe, the magnetic field is increased in steps of 0.25-0.5 mT.

The first mode can be clearly seen as a red colored area positioned at a resonance field of about 72 mT. The color of the broad and laterally elongated region around it corresponds to a positive Kerr voltage arising from the peak in the center. This coincides with the previous studies on SW spectroscopy and electrical anisotropy measurements. The blue colored area is linked to a negative anti-node in the center which is flanked by two positive anti-nodes at the sides. The distance between first and third mode is roughly 8 mT which was derived previously. Here, the recording time of a single line scan is about four minutes and a single data point is measured with an integration time of three seconds. The measurement time was chosen to guarantee a good signal-to-noise ratio while diminishing drifting, which occurs for very long measurements. No additional data processing filters are used.

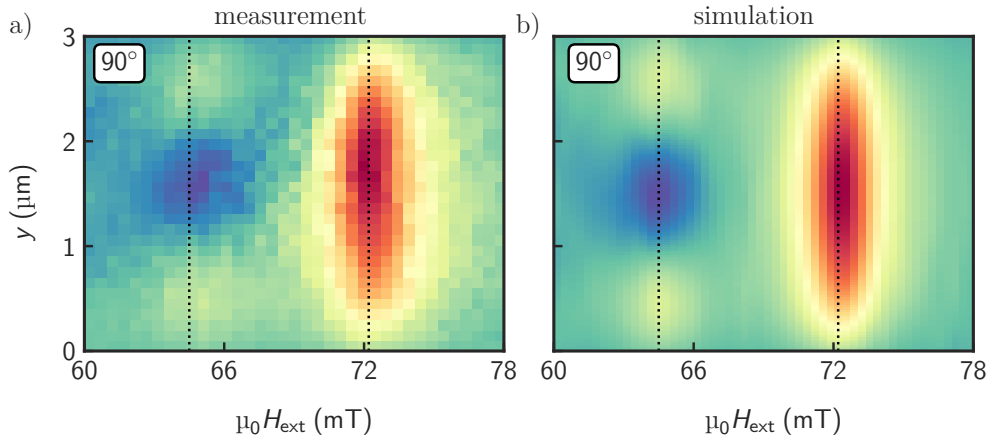

Figure 6.9: a) Recorded Kerr signal for line scans in a range of different fields with $\psi = 90°$. The first (red, 72 mT) and third (blue, 64 mT) mode is clearly observable, since these modes are the only ones which are excited by the homogeneous excitation from the CPW (dashed lines). A 2D color plot with field and space coordinate as the x and y-axis, respectively, gives a good insight into the magnetic mode pattern with the Kerr voltage as colorcode. The measured data can be well reproduced by MuMax3 simulations (b).

The image of the measured TRMOKE pattern can be reproduced very well by a micromagnetic simulation with MuMax3 as introduced in Sec. 3.7. Fig. 6.9(b) shows the simulated data for the same frequency, phase and stripe orientation. A homogeneous oop driving field h_z of several Oersted excites the magnetization. In addition, necessary fields such as the uniaxial and four-fold anisotropy, and magnetic properties as the effective and saturation magnetization are included in the simulation. With the given material parameters from Tab. 3.17, it is possible to reproduce the field positions as well as mode spacing in a very good way. Note that both graphs are normalized with regard to their maximum amplitudes and a Gaussian smearing is applied to account for the broadening of the laser spot.

In conclusion, these tools allow the excitation and efficient optical probing of SSWs. Further, micromagnetic simulations reproduce the data with the given parameters in great accordance, which is further exploited in the following study of current-induced SOFs.

6.2.4 Current-driven standing spin waves

In order to investigate the spin-orbit fields originating at the interface of a Fe/GaAs system, the sample layout must be changed to a stripe attached to two contacts as seen in Fig. 6.2(b). Fig. 6.10 indicates the three generated fields by an rf-current through the device which are explained in the following. By sending an rf-current through a Fe/GaAs stripe, two effective, current-indeuced magnetic fields, namely Dresselhaus- and Rashba-like SOF, are generated from

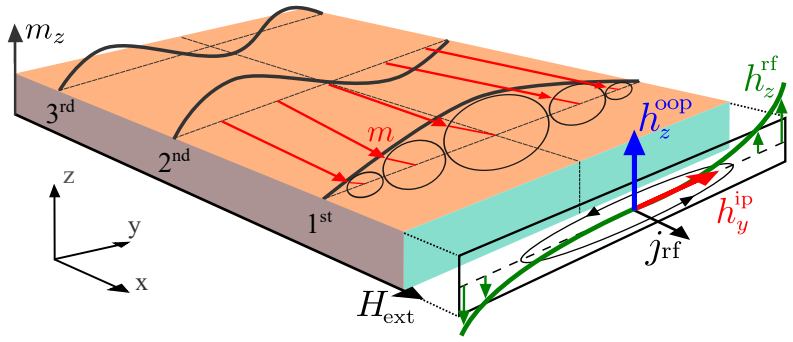

Figure 6.10: Excitation of standing spin waves by a current j_{rf}. In the cross section of the stripe, the involved fields h_y^{ip}, h_z^{oop} and h_z^{rf} are shown.

the bulk inversion asymmetry and the C_{2v}-interface, respectively. Both in-plane h_y^{ip} and out-of-plane h_z^{oop} contributions are homogeneous across the stripe. Additionally, the rf-current causes an anti-symmetric Oersted field h_z^{rf} which increases in opposite direction towards both edges. Due to this field, odd modes with even mode number n arise and, thus, both types of modes are present having a drastic influence on the mode pattern.

6.2.4.1 Characterization of the current-driven SSWs

First, the new excitation method is investigated with respect to its induced changes. This is done in the spectroscopy mode which reveals the previously mentioned formation of odd modes. Fig. 6.11 shows the normalized Kerr voltage with respect to the topographic signal on the GaAs substrate. This map is similar to the data from the previous geometry, however, an additional dent appears below the first mode. The anti-symmetric contribution from the current-induced Oersted field lowers and increases the modes on the different halves of the stripe. This changes also the resonance position and another mode spectrum is obtained, which has to be evaluated in the following.

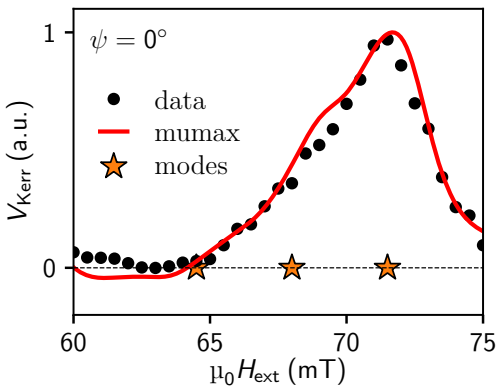

Figure 6.11: Dependence on the magnetic field reveals almost the same behavior as for homogeneous excitation. The data can be fitted by a combination of three Lorentzian functions for each of the first three modes.

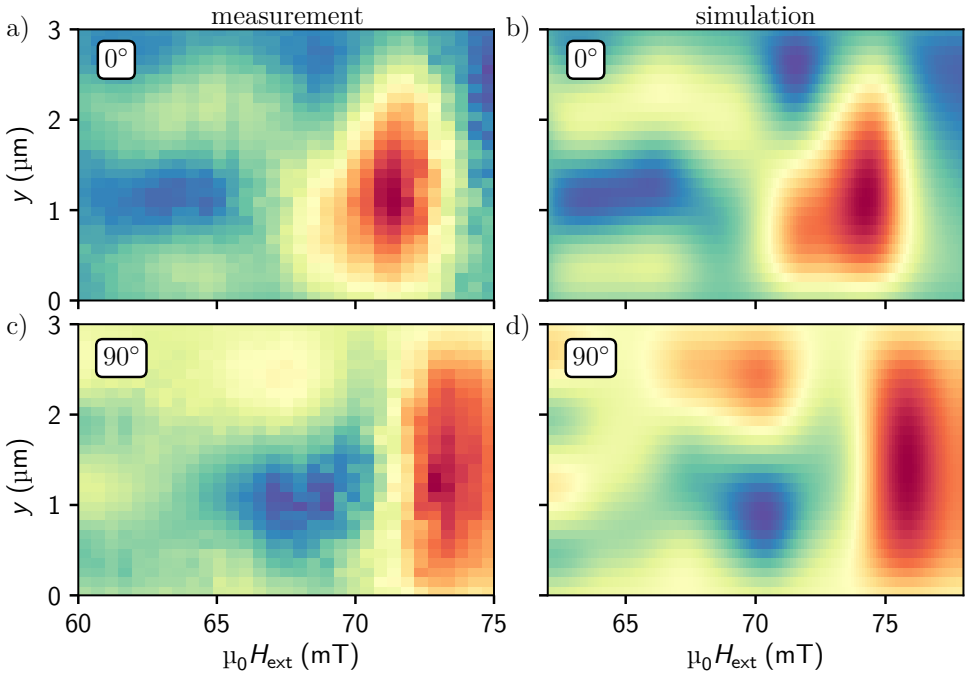

Figure 6.12: a, c) Recorded Kerr signal at two different phases of applied rf-current shows a completely different mode pattern for the [110] crystal direction. b, d) Measured data is fitted with MuMax3 in order to extract both in-plane and out-of-plane SOFs acting on the magnetization. The colorcode indicates the normalized amplitude of the extrema over all pictures.

6.2.4.2 Current-induced mode pattern

It was shown previously, that the odd modes together with SOFs changes the modes in such a way that the whole mode pattern has to be taken into account for the data evaluation. The imaging mode can record the same 2D colored pattern to investigate the strength of the SOFs. Fig. 6.12(a,c) show the measured Kerr signal for two different phases of $\psi = 0$ and 90°, respectively, and a current density of $j = 1.5 \cdot 10^{11}\,\mathrm{A/m^2}$ at 12 GHz along a [110] orientated stripe. The image looks, compared to the homogeneous excitation image in Fig. 6.9, drastically altered by the appearance of even modes. Comparing panel a) to the CPW pattern in Fig. 6.9(a), the first mode in both images appear as a antinode peak (red color), whereas both phases differ by 90°. This shift relates to the *oop* driving field from the CPW which was already observed in Sec. 6.2.2.

A closer look on the current-induced mode pattern reveals a displacement of the first and third modes towards the lower edge due to the influence of the anti-symmetric Oersted field. This causes an enhancement of the pattern at the bottom half of the stripe. The third mode gains only a little shift to the lower side since the amplitude decreases to lower magnetic fields. Obviously, the first two modes merge to a red triangularly shaped area where the highest amplitude is located at a field between both modes. This is not equal to the

field position determined by CPW measurement, which can be attributed to the effect from the second mode. In panel c), showing a phase of 90°, the pattern reveals more features where the second and fourth mode is visible as blue colored areas together with a big red area above the first mode. Around the first mode, a pronounced negative and positive area of signal is developed. In between, no signal is present and the anti-symmetric modes as well as odd modes are better distinguishable.

The two maps can be reproduced by MuMax3 simulation where the three current-induced fields are added to the code. The Oersted field created by the current density is computed by Biot-Savart's law taken into account the stripe width and applied rf-current. The amplitudes of in-plane and out-of-plane fields are set to several microtesla initially. The first simulated maps already reveal the magnetic mode pattern with the initially guessed parameters very well. Nevertheless, a least square algorithm tries to minimize the difference between data and simulation by changing the two SOFs simultaneously. The simulated pattern for one phase is compared pixel by pixel with the measured data for the same phase between rf-current and magnetization precession. For this reason, it is very important to align both images properly. The algorithm slightly changes both SOFs, repeats the simulation with the new fields and again compares both images. The matching parameter is either smaller or larger as the previously derived percentage. In the beginning, this is done three times with only very small deviations from the initial value giving a rough trend which makes it easier to find the proper values. In every iteration step, the algorithm tries to minimize the difference between both images until a threshold of minimal difference is found.

This happens after about 20 runs, some convergence criterium is fulfilled and only minor changes of the SOFs are observed within the last five iterations. For a [110] device with a current density of $1.0 \cdot 10^{10}\,\mathrm{A/m^2}$, the *ip* and *oop* SOFs are determined to 56.4 µT and 10.0 µT, respectively. The final value is averaged over the last five iterations of the algorithm, where the deviation is less than 1%. Fig. 6.12(b,d) shows the resulting simulated images which clone the measured data very well. The measurements are repeated for all four patterned stripes

axis	$h_\perp^{\mathrm{ip}}$	$h_\perp^{\mathrm{oop}}$	$h_\perp^{\mathrm{ip}}/h_\perp^{\mathrm{oop}}$	j_{rf}	$h^{\mathrm{ip}}/j_{\mathrm{rf}}$	$h^{\mathrm{oop}}/j_{\mathrm{rf}}$
	µT	µT		$10^{11}\,\mathrm{A/m^2}$	$10^{-15}\,\mathrm{Tm^2/A}$	
[100]	55.3	9.07	6.4	1.0	0.55	0.09
[010]	42.4	7.06	6.0	1.0	0.42	0.07
[110]	56.4	10.0	5.6	1.0	0.56	0.10
[-110]	29.4	7.52	3.9	1.0	0.29	0.08

Table 6.1: Summary of the in- and out-of-plane SOFs for the four crystallographic orientations derived by MuMax3 simulations.

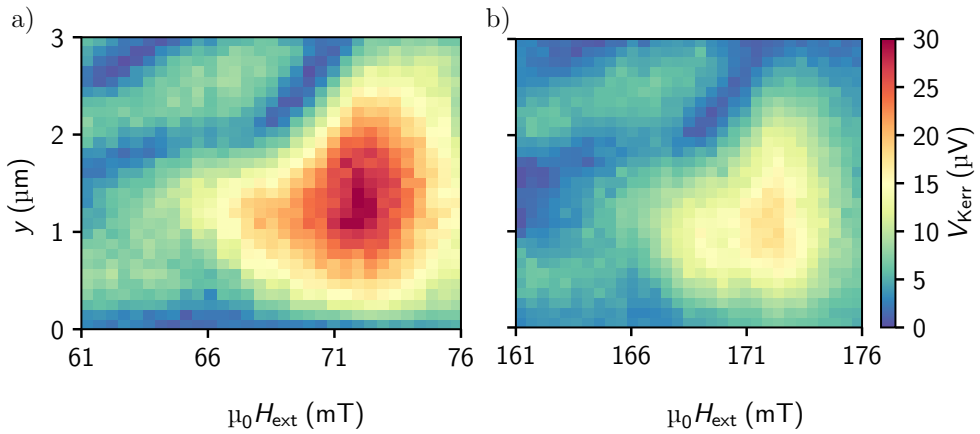

Figure 6.13: The Kerr signal on a [110] (a) and [-110] (b) patterned stripe normalized on the current density.

along the main crystal axes of the GaAs wafer together with accompanying micromagnetic simulations. Here, h^{ip} denotes the in-plane SOFs orientated perpendicularly with respect to the current or stripe direction.

The derived in- and out-of-plane SOFs for the four crystallographic axes are summarized in Tab. 6.1 together with the current density from the micromagnetic simulation. Throughout all devices, the in-plane SOFs are roughly six times larger than the *oop* fields for the same direction except of a ratio of only four along the [-110] direction. The fields of the devices patterned along [100] and [010] can be addressed solely to the Bychkov-Rashba fields, which are orientated perpendicular with respect to the current direction.

Fig. 6.13 shows absolute Kerr intensity of the 0° and 90° phase for the [110] (a) and [-110] (b) oriented stripe. Here, a larger signal is observed around the first mode as red colored area due to the amplified Bychkov-Rashba and Dresselhaus fields. The out-of-plane SOFs are evenly spread around $h_{\perp}^{\mathrm{oop}} = (0.09 \pm 0.01) \cdot 10^{-15}\,\mathrm{Tm^2/A}$.

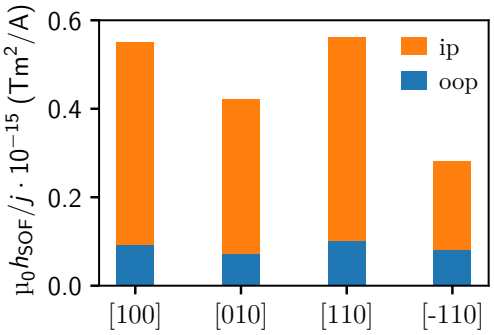

Figure 6.14: The simulated in- and out-plane SOFs normalized by the current density.

6.2.4.3 Discussion of results

The two different detection approaches can be compared in terms of *ip* and *oop* spin-orbit fields. However, as mentioned previously, the Bychkov-Rashba and Dresselhaus field can only be distinguished along the [100] and [010] direction. In the following, the *ip* fields are normalized by the current density along these direction.

From the SOT-FMR values in Tab. 5.2, the Bychkov-Rashba SOFs are $h_{\perp}^{\mathrm{ip}}/j_{\mathrm{rf}} = 0.82$ and $0.65 \cdot 10^{-15}\,\mathrm{Tm}^2/\mathrm{A}$ for the [100] and [010] patterned stripe, respectively. The optically detected fields in the same stripes are $h_{\perp}^{\mathrm{ip}}/j_{\mathrm{rf}} = 0.58$ and $0.42 \cdot 10^{-15}\,\mathrm{Tm}^2/\mathrm{A}$, which are around 30% smaller than the electrical detected ones. Additionally, a the [100] sample with both techniques shows a 20% larger magnitude confirming the previous tendency of the SOT-FMR measurement. The two directions should be equally from the theoretical consideration of spin-orbit interaction. An explanation could be different samples since the tendency is observed by two different techniques.

Mumax3 simulations are limited to perpendicularly orientated fields with respect to the longitudinal stripe axis. Nevertheless, it is possible to determine the Dresselhaus fields parallel to the stripe by the following assumption: the resulting SOF along [110] can be regarded as the sum of Bychkov-Rashba and Dresselhaus field. In contrast, the difference of both is observed in the [-110] direction as already pictured in Fig. 2.4. From the *ip* data in Tab. 6.1, a Dresselhaus field can be calculated to $h_{\parallel}^{\mathrm{ip}} = 13.5\,\mu\mathrm{T}$ by using the Bychkov-Rashba field $h_{\perp}^{\mathrm{ip}} = 42.4\,\mu\mathrm{T}$ of the [010] stripe. This leads to a ratio of $h_{\perp}^{\mathrm{ip}}/h_{\parallel}^{\mathrm{ip}} \approx 3.1$ which is larger than the ratio of 2.0 detected electrically.

The mean value of the electrically derived fields normalized by current density is $h_{\perp}^{\mathrm{oop}}/j = (0.57 \pm 0.09) \cdot 10^{-15}\,\mathrm{Tm}^2/\mathrm{A}$, see Tab. 5.3. This is slightly smaller than previously reported fields on the same material system, which can be explained by slightly different interface properties for different samples [8]. The optically observed fields reach only values of around $h_{\perp}^{\mathrm{oop}}/j = (0.09 \pm 0.01) \cdot 10^{-15}\,\mathrm{Tm}^2/\mathrm{A}$. One reason could be the four times smaller susceptibility of the out-of-plane contribution compared to the *ip*, and thus a smaller impact on the mode pattern. This is also observed in a larger variance of the *oop* field within the last five iterations of the algorithm before the convergence criterium. Concluding, the constant *oop* field is confirmed by the simulations, however the magnitude deviates from the SOT-FMR results. All fields normalized by the current density is visualized in Fig. 6.14.

6.2.4.4 Evaluation of the eigenmodes

After determining the important SOFs, the focus is placed on the evaluation of the mode profile with respect to the spatial coordinate. Thereby, a closer look can be taken on the fields contributing to the development of the mode

[!b]

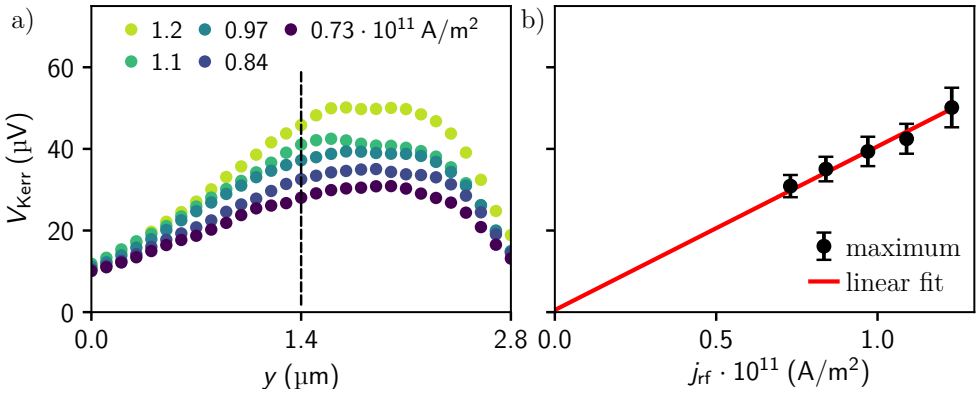

Figure 6.15: a) On a [110] oriented stripe the Kerr signal of the first mode increases for higher current densities and shows an asymmetry due to the antisymmetric Oersted field. b) The maximal Kerr amplitude with error bars as a function of applied current density follows a linear dependence.

spectrum.

Fig. 6.15(a) shows the dependence of the Kerr amplitude with respect to the current density. A linear behavior is expected from former electrical measurements. The mode amplitude is enhanced towards the left half of the stripe. In order to extract the maximum amplitude, each curve is fitted by simulation with error bars for each current density, see panel b). The data is fitted by a linear regression through the origin and a slope of $(40 \pm 1) \cdot 10^{-17}\,\mathrm{Vm^2/A}$ is read out. Within the error bars, the fit can confirm the linear dependence on the current density.

Fig. 6.16 shows the first three eigenmodes versus y for both phases which illustrates the underlying physics in a very good way. The first and third mode

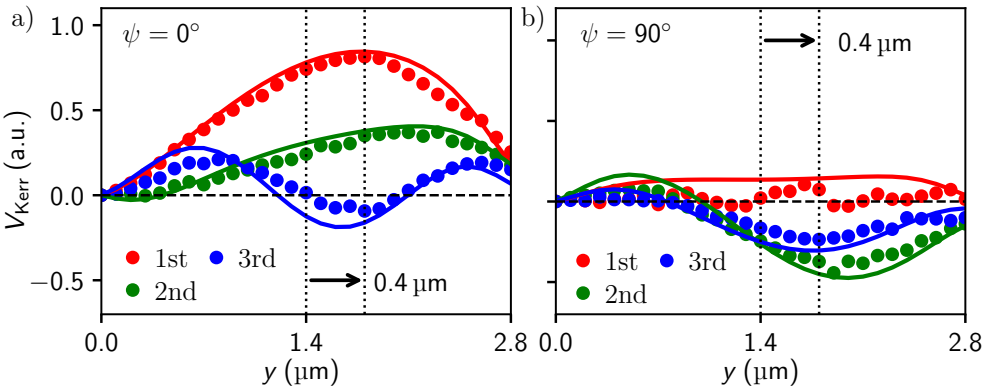

Figure 6.16: The eigenmodes can be displayed with respect to the lateral space coordinate across the stripe width for $\psi = 0°$ (a) and 90° (b) phase. The measured data matches quite well with micromagnetic simulations and reveals a shift of the maximal amplitude to the right edge of about 0.4 µm.

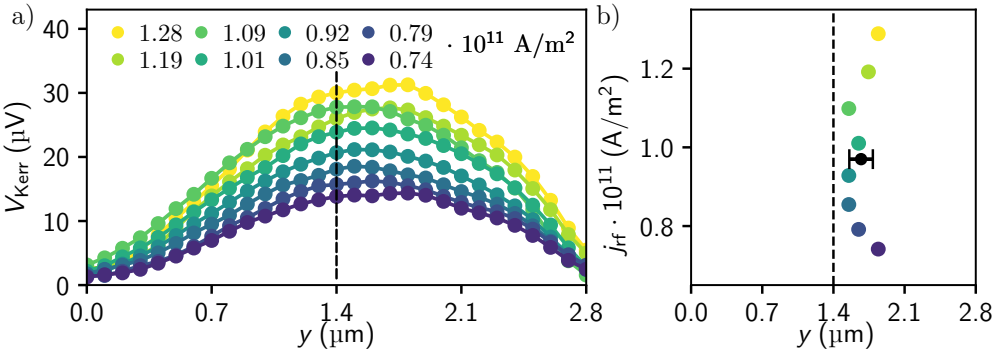

Figure 6.17: a) The Kerr signal for the first mode increases for higher current densities along a [110] oriented stripe as expected. b) The space coordinate of each maximum scatters around a mean value of $(1.67 \pm 0.12)\,\mu m$ (black dot) resulting in a shift of $0.27\,\mu m$ to the right edge of the stripe.

are more visible for a phase of 0° in contrast to the second mode, which is more pronounced at $\psi = 90°$. In both images, all three modes reveal a shift to the right edge of the stripe of about $(0.4 \pm 0.1)\,\mu m$. This shift arises solely by the Oersted field which is discussed later in more detail.

The lateral position of the eigenmodes is investigated in a [110] oriented stripe where the Kerr signal of the first mode is evaluated. Fig. 6.17(a) shows a strong dependence of the amplitude of the Kerr signal on the applied current as in former measurements. Obviously, the signal amplitudes increases for higher rf-currents. The y-coordinate of the maximal Kerr signal can be plotted as a function of current, which can be evaluated as a shift from the center of the stripe at $1.4\,\mu m$, as can be seen Fig. 6.17(b). The values scatter around a mean value of $(1.13 \pm 0.12)\,\mu m$. This leads to a displacement of $(0.27 \pm 0.12)\,\mu m$ which confirms the previous value from the eigenmodes.

This shift can be verified by micromagnetic simulations where the SOFs are increased linearly with the current density. Fig. 6.18 shows that the lateral position of the maximal amplitude is constant for different current densities as expected. The same value of displacement can be reproduced to be about

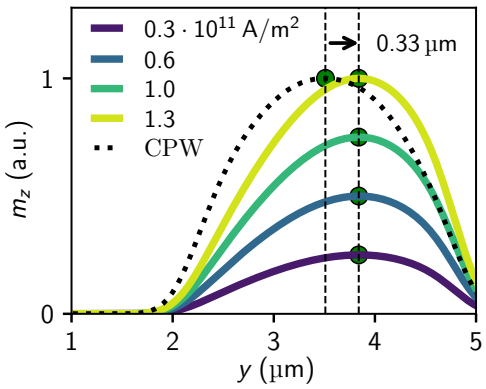

Figure 6.18: Current density dependence on a simulated [110] orientated stripe with different excitation power and adapted SOFs. The black line indicates the reference homogeneous excitation by the *oop* field from the CPW. Clearly, a shift due to the current-induced SOFs of $0.33\,\mu m$ can be seen.

0.33 µm which is in good agreement with the measurement.

6.3 Standing spin waves in the BV geometry

Now, the external field is rotated perpendicular, but still in-plane to the stripe axis where spin waves are excited in the so-called backward volume geometry. As introduced in Sec. 3.5.2, the developed modes look completely different. Here, all modes are concentrated in the middle of the stripe and forming a crescent-shaped mode pattern towards higher fields. At first, the transition from Damon-Eshbach to backward volume geometry is discussed by a sweep of magnetic field angle.

As a first step, the magnetic Kerr signal is recorded at the stripe center by means of the SW spectroscopy technique. Fig. 6.19(a) shows the Kerr signal with increasing magnetic field beginning in the DE geometry at $\phi_H = 0°$ as the darkest spectrum. Then, the angle of the applied field is rotated in steps of about 15° up to $\phi_H = 90°$ which corresponds to the BV case. By doing so, the resonance position of each spectrum moves to lower field (50 mT) and then up to 175 mT, marked as yellow line. This change of resonance is mainly due to the anisotropy, which exhibits an easy axis along [110] and a hard axis along the [-110] direction. This was discussed in detail in the electrical SOT-FMR section. Fig. 6.19(b) visualizes the resonance position as a function of the magnetic field angle where the color of the data points corresponds to the angle of the spectra in the left image. This angular dependence can be fitted, as shown in Sec. 5.3, in order to determine the anisotropy constants where

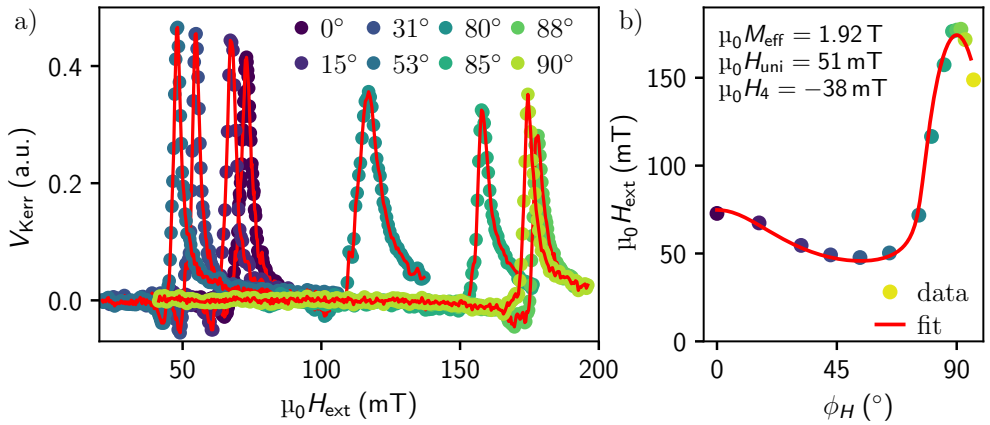

Figure 6.19: a) Several Kerr spectra at different magnetic field angles ranging from the parallel ($\phi_H = 0°$, DE) to the perpendicular ($\phi_H = 90°$, BV) geometry where the current is always applied along the [110] direction. b) The resonance position moves from smaller (easy axis, $\phi_H = 45°$) to higher fields (hard axis, $\phi_H = 90°$). An angular fit determines the anisotropy fields which fits very good with previous full-film FMR experiments.

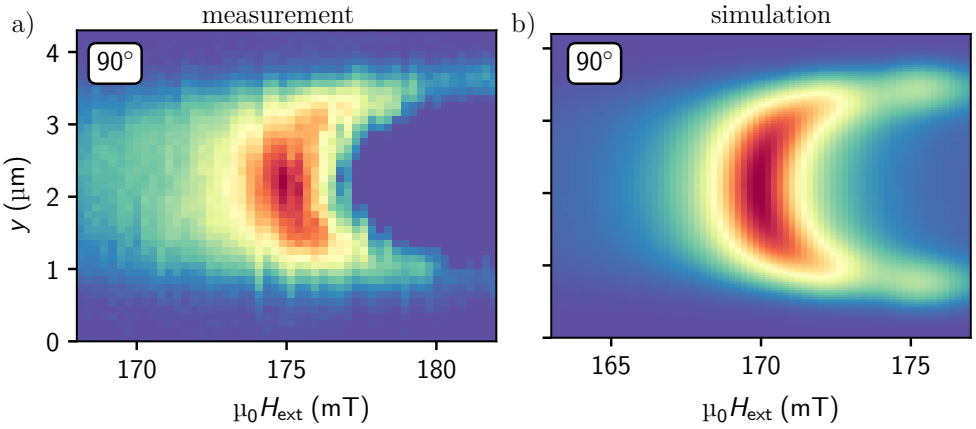

Figure 6.20: a) The mode pattern for a perpendicularly magnetized stripe shows a crescent-shape with a distinct maximum at the middle of the stripe. All modes are merged to one single resonance at about 175 mT due to the almost horizontal dispersion relation at $k = 0$. The magnetic field angle corresponds to the hard axis for a current direction along the [110] orientation. b) A micromagnetic simulation reveals additional edge modes for higher fields.

values of $\mu_0 H_{\text{eff}} = 1.92\,\text{T}$, $\mu_0 H_{\text{uni}} = 51\,\text{mT}$ and $\mu_0 H_4 = -38\,\text{mT}$ are received, which confirms the previous values derived by full-film FMR characterization measurements in a very accurate way.

The mode pattern is constructed by several line scans and fields around 175 mT both along the [-110] hard axis while the current and stripe direction is along [110]. For this perpendicularly magnetized stripe, the SSWs are driven by the homogeneous *oop* Oersted field from a CPW in order to excite only even modes.

In Fig. 6.20(a), the familiar crescent-shaped mode can be seen which were already introduced in Sec. 3.5.2 by numerical calculations. All modes are located near one certain field value. Both tips of the crescent-shaped mode are pointing towards higher fields and the signal increases from the left side towards the maximum and falls to negative values on the right. Due to the negative dispersion at $\mathbf{k} = 0$, the modes are bundled so closely to each other that no mode spacing can be found. Fig. 6.20(b) shows the equivalent mircomagnetic simulation which verifies the experimental data very well. Notably, edge mode are more prominent than in the experiment. The reason could an influenced signal due to close vicinity to the edge. Further, a small deviation from the 90° field angle can change the mode drastically. Nevertheless, the data can be qualitatively well recapped.

A closer look on the received pattern can be taken by plotting separate line scans along H_{ext} and y axis. Fig. 6.21(a) displays the signal the magnetization during a magnetic field sweep at the center of the stripe. The Kerr signal is well fitted by a single Lorentzian line shape indicating the appearance of a single

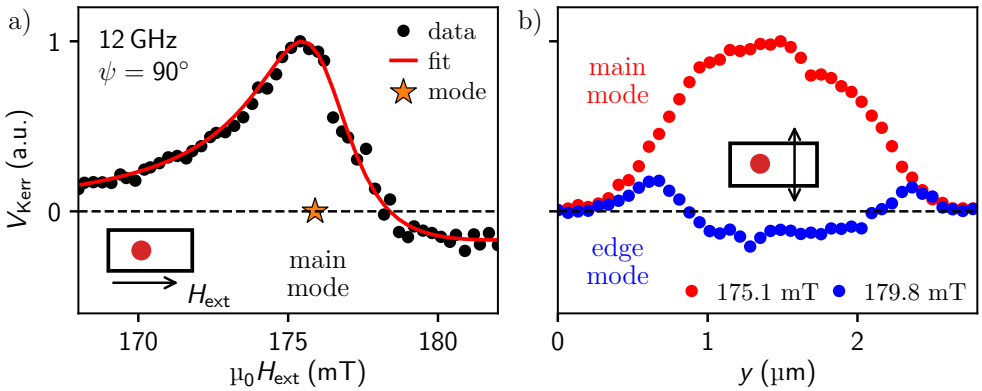

Figure 6.21: a) The field dependence of the Kerr voltage at the center of the stripe shows one broad peak. Again, the current flows along [110] and the magnetic field is perpendicular, i.e. the hard axis. b) In lateral dimension, the main mode is clearly visible together with a not very pronounced edge mode towards higher fields.

mode. However, the broad linewidth confirms the previous statement, that in the Lorentzian lineshape of the mode maybe composed of several merging modes. In particular, the fitted linewidth of 1.94 mT is larger than the value along [100] longitudinally magnetized sample of 1.82 mT. In the following, we will denote the merged mode as the main mode. Fig. 6.21(b) illustrates the two diverse mode profiles as lateral coordinate at certain fields, namely the large main mode at around 175 mT and one edge mode at about 180 mT. As previously seen, the main mode contains a large positive amplitude in the center of the stripe whereas the edge mode has two maxima towards both edges and negative values in the middle.

Finally, the magnetization is again driven by a rf-current which induces the

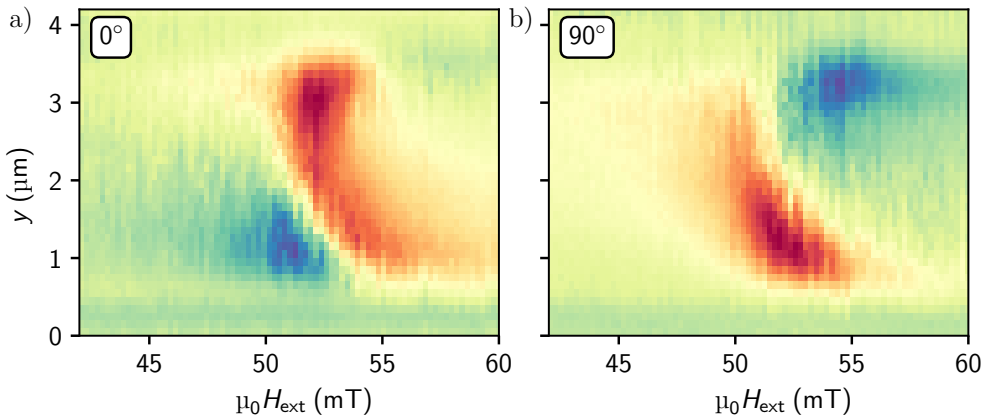

Figure 6.22: The current-induced mode pattern for a perpendicularly magnetized stripe is completely different compared to the DE geometry. A [100] oriented stripe shows a splitting of the crescent-shaped mode for both phases of $\psi = 0°$ (a) and 90° (b).

same three contributions acting on the magnetization as for the DE case.

Fig. 6.22 shows the mode pattern of the Kerr signal for two phases of 0 and 90° on a [100] orientated stripe. The Oersted field splits the crescent-shape mode into two parts with opposite amplitude. The SOFs increase the *oop* magentization in one area which is either the upper or lower half of the stripe for $\psi = 0$ and 90°, respectively. However, these pictures cannot be reproduced by micromagnetic simulations. The algorithm diverges while trying to find an accordance between measured data and simulated pattern. With a variation of initial start parameters of the code or a slightly different magnetization angle, it is still not possible to reproduce the mode pattern by simulations.

The simulated image for the BV geometry with the previously derived SOFs along the same orientation is also completely different to measured data. Within this thesis, it was not possible to find a solution that the Mumax3 simulation can reproduce the mode pattern obtained by measurements for this configuration.

7
Summary

Current-induced spin-orbit fields are acting as torques on the magnetization, which arises either from spin currents or spin accumulations depending on the material system. The torques are studied in Py/Pt and Fe/GaAs systems by different techniques at room temperature. Two main principles are utilized in order to detect the precession amplitude of the magnetization: electrically by the dc-voltage rectification (ST-/SOT-FMR) or optically by the Kerr effect (TRMOKE). Fabricated nanostructures in the micrometer range are excited either directly by injecting a microwave current or externally by an *oop* rf-driving field from a CPW. The electrical current modifies the magnetization precession by a spin-transfer or spin-orbit torque depending on their origin. The torques are generated by a spin-polarized current from a normal metal layer or a spin accumulation at the interface.

In the first experiment, reported results on a Py/Pt bilayer are reviewed by the ST-FMR technique together with electrical modulation of damping and equilibrium change method. Two quantities, the spin Hall angle and spin diffusion length, are determined for a fixed ferromagnet of 4 nm Py and varying Pt layer thickness between 0 and 8.4 nm. The ST-FMR is widely used as a standard method for investigating current-induced magnetization precession profiles, however, can only be applied to certain material system since it overestimates the spin Hall angle for involved field-like torques. A main difference between the discussed methods is the influence on the magnetization by injecting a spin current (ST-FMR, SP-ISHE) and the modification of the linewidth due to an additional dc-current (MOD).

First, a transparent interface is regarded leading to an effective spin Hall angle due to the neglected Py/Pt interface contribution. The conversion efficiency of a charge into a spin current increases with increasing platinum thickness until a saturation level above 6 nm of $\theta_{\mathrm{SHA}}^{\mathrm{eff}} = 0.11$ for ST-FMR is reached. This agrees very well to $\theta_{\mathrm{SHA}}^{\mathrm{eff}} = 0.10$ from electrical MOD experiments on the same device, which is exactly the reported value for optical MOD measurements on the same wafer [37]. In addition, the spin Hall angle results are repeated by the optical equilibrium change method, where the spin Hall angle is derived by the spin-orbit efficiency parameter to $\theta_{\mathrm{SHA}}^{\mathrm{eff}} = 0.11$. Thus, all three different measurement technique provide the same results as expected, since the samples originate from a single set of wafers.

Next, the contribution of the bilayer interface is considered, which is governed by the spin-mixing conductance. The measurements are repeated for a set of varying platinum layers, since the spin-mixing conductance exhibits are strong dependence on the normal metal thickness. First, it increases linearly until about 4 nm, where it saturates to about $g_{\mathrm{eff}}^{\uparrow\downarrow} = 2.2 \cdot 10^{19}\,\mathrm{m}^{-1}$. The interface-related spin Hall angle, normalized by the spin-mixing conductance, is obtained by a $\tanh(d_{\mathrm{Pt}}/\lambda_{\mathrm{Pt}})$-fit to $\theta_{\mathrm{SHA}}^{\mathrm{i}} = 0.26$ together with a spin diffusion length of $\lambda_{\mathrm{Pt}} = 1.77\,\mathrm{nm}$. The SHA is close to reported values of $\theta_{\mathrm{SHA}}^{\mathrm{i}} = 0.31$ by SP-ISHE measurements. A spin diffusion length of $\lambda_{\mathrm{Pt}} = 1.7\,\mathrm{nm}$ agrees also very well and confirms the link between both methods. However, the results differ to $\theta_{\mathrm{SHA}}^{\mathrm{i}} = 0.45$, which is obtained by optical modulation of damping. Nevertheless, the electrically detected MOD value can be calculated to 0.37 by assuming the same interface contribution. This is appropriate considering the effect by te interface and measuring the same sample. The magnitude of the interface-like SHA by ST-FMR agrees well with published results for similar Py/Pt bilayers, where values of $\theta_{\mathrm{SHA}}^{\mathrm{i}} = 0.2 - 0.3$ are reported [38–40]. A large variance in the SDL is observed due to the different growth technique of platinum and the Pt grain size is strongly related with the spin Hall conductivity and the interface transmittance. Finally, several temperature dependent measurements with ST-FMR and static equilibrium method reveal a similar behavior down to a few Kelvin within the error bars. The slight decrease can be explained by a change of the spin diffusion length and conductivity. Concluding, the spin-orbit field and the spin Hall angle are strongly related, since both originates from the same spin Hall effect.

The goal of the second experiment is the detection and quantization of spin-orbit fields in a thin, micrometer wide stripe of Fe/GaAs(001) along the four crystallographic axes. On the one hand, this was performed electrically by the SOT-FMR technique. On the other hand, a new approach was developed in order to determine the SOF optically. Basically, the interface provides a C_{2v}-symmetry which induces Bychkov-Rashba-like SOFs together with Dresselhaus fields from the bulk. These originate from a spin accumulation at the interface and drive the magnetization precession in the ferromagnetic layer. These fields are explored in two different ways:

(i) A rectified dc-voltage, built up along the stripe due to anisotropic magneto resistance and rf-current, can be decomposed into a symmetric and antisymmetric Lorentzian line shape. The two voltages amplitudes are evaluated with respect to the angle of the magnetization due to the dragging effect from the strong anisotropy in iron. The behavior of the two voltage magnitudes with respect to the magnetization angle follows a combination of a sine and cosine functions. The parallel and perpendicular SOFs can be derived with respect to the current or stripe direction. The comparison of in-plane SOFs reveal a mainly Bychkov-Rashba dominated interface for

[100] and [010] directions, which is roughly twice the Dresselhaus-like contribution. The effective *ip* SOFs are up to two times larger than the out-of-plane fields and exhibit a pronounced angular dependence. The largest magnitude is along the [110] axis due to the two-fold symmetry in contrast to a relative constant magnitude for the *oop* fields. The normalized perpendicular SOFs with respect to the current densities are $h_{\perp}^{\mathrm{ip}}/j_{\mathrm{rf}} = (0.5 - 1.4)$ and $h_{\perp}^{\mathrm{oop}}/j_{\mathrm{rf}} = (0.35 - 0.65) \cdot 10^{-15}\,\mathrm{Tm}^2/\mathrm{A}$. Overall, a larger *ip* value is observed as expected from previously measured data in wider stripes [8].

(ii) A new optical approach is developed to quantify the SOFs in order to confirm the electrical results. A TRMOKE microscope is used to resolve the developed standing spin waves generated by the combination of two SOFs and the Oersted field from a rf-current. The inhomogeneous driving torques cause a distinct mode pattern in the Fe stripe, where the polar component of the magnetization is probed by the TRMOKE. The mode profile across the stripe is received for different magnetic fields in the DE geometry. A homogeneous driving field is used to determine the important quantities as the mode spacing and resonance fields. The measured data is verified by micromagnetic simulations, which reproduce the measured data with high accuracy. Additionally, this approach is self-calibrated since the dynamic mode pattern can be compared with the homogeneous pattern as a reference. The SOFs in the micromagnetic simulations are tuned to reproduce the measured pattern. The strength of the SOFs is quantified by an algorithm which tries to minimize the difference between measured and simulated mode map. A similar distribution of the in-plane SOFs is found for the four crystallographic axes, where the [110] again shows the largest magnitude and [-110] the lowest. In addition, the out-of-plane SOFs scatter around a constant value despite a large spike for the [110] device which cannot be explained. Nevertheless, normalized SOFs of $h_{\perp}^{\mathrm{ip}}/j_{\mathrm{rf}} = (0.29 - 0.56)$ and $h_{\perp}^{\mathrm{oop}}/j_{\mathrm{rf}} = 0.09 \cdot 10^{-15}\,\mathrm{Tm}^2/\mathrm{A}$ are extracted from the simulations for the in-plane and out-of-plane fields, respectively.

The two methods are compared with respect to their SOF magnitudes along the [100] and [010] directions. Optically, only the Bychkov-Rashba-like fields are accessible and an assignment of the two SOFs can only be made for [100] and [010] devices. The electrically detected fields are roughly two and seven times larger than the optical ones for the in-plane and out-of-plane orientation, respectively. In addition, the optically derived ratio of $h_{\perp}^{\mathrm{ip}}/h_{\perp}^{\mathrm{oop}}$ is about three times larger than the electrical ratio. These deviations could be explained by the local and non-local measuring procedure and the current calibration with two different setups but have to be evaluated further. Nevertheless, the same distribution along the four crystallographic axes can be observed, where the [110] device exhibits the largest magnitude and [-110] the smallest. Within the time frame of this thesis, it was not possible to investigate the open questions

arising from the difference of the two methods.

Concluding, it was shown that spin-orbit fields can be measured by an electrical and optical approach on the very same sample design. The new method provides a elegant tool to quantify the SOFs by a TRMOKE and micromagnetic simulations.

Bibliography

[1] J. Fabian, A. Matos-Abiague, C. Ertler, P. Stano, and I. Žutić. *Semiconductor spintronics.* Acta Phys. Slov. **57**, 565 (2007).

[2] S. A. Wolf, A. Y. Chtchelkanova, and D. M. Treger. *Spintronics: A retrospective and perspective.* IBM Journal of Research and Development **50**, 101–110 (2006).

[3] D. Apalkov, B. Dieny, and J. M. Slaughter. *Magnetoresistive Random Access Memory.* Proceedings of the IEEE **104**, 1796–1830 (2016).

[4] S. Bhatti, R. Sbiaa, A. Hirohata, H. Ohno, S. Fukami, and S. Piramanayagam. *Spintronics based random access memory: A review.* Materials Today **20**, 530–548 (2017).

[5] K. Ando, S. Fujita, J. Ito, S. Yuasa, Y. Suzuki, Y. Nakatani, T. Miyazaki, and H. Yoda. *Spin-transfer torque magnetoresistive random-access memory technologies for normally off computing (invited).* Journal of Applied Physics **115**, 172607 (2014).

[6] E. Saitoh, M. Ueda, H. Miyajima, and G. Tatara. *Conversion of spin current into charge current at room temperature: Inverse spin-Hall effect.* Applied Physics Letters **88**, 182509 (2006).

[7] S. Karube, K. Kondou, and Y. C. Otani. *Experimental observation of spin-to-charge current conversion at non-magnetic metal/Bi2O3 interfaces.* Applied Physics Express **9**, 033001 (2016).

[8] L. Chen, M. Decker, M. Kronseder, R. Islinger, M. Gmitra, D. Schuh, D. Bougeard, J. Fabian, D. Weiss, and C. H. Back. *Robust spin-orbit torque and spin-galvanic effect at the Fe/GaAs (001) interface at room temperature.* Nature Communications **7**, 13802 (2016).

[9] K. Garello, I. M. Miron, C. O. Avci, F. Freimuth, Y. Mokrousov, S. Blügel, S. Auffret, O. Boulle, G. Gaudin, and P. Gambardella. *Symmetry and magnitude of spin-orbit torques in ferromagnetic heterostructures.* Nature Nanotechnology **8**, 587 (2013).

[10] X. Fan, J. Wu, Y. Chen, M. J. Jerry, H. Zhang, and J. Q. Xiao. *Observation of the nonlocal spin-orbital effective field.* Nature Communications **4**, 1799 (2013).

[11] X. Fan, H. Celik, J. Wu, C. Ni, K.-J. Lee, V. O. Lorenz, and J. Q. Xiao. *Quantifying interface and bulk contributions to spin-orbit torque in magnetic bilayers.* Nature Communications **5**, 3042 (2014).

[12] L. Chen, M. Gmitra, M. Vogel, R. Islinger, M. Kronseder, D. Schuh, D. Bougeard, J. Fabian, D. Weiss, and C. H. Back. *Electric-field control of interfacial spin–orbit fields.* Nature Electronics **1**, 350–355 (2018).

[13] L. Chen, S. Mankovsky, S. Wimmer, M. A. W. Schoen, H. S. Körner, M. Kronseder, D. Schuh, D. Bougeard, H. Ebert, D. Weiss, and C. H. Back. *Emergence of anisotropic Gilbert damping in ultrathin Fe layers on GaAs(001).* Nature Physics **14**, 490–494 (2018).

[14] S. Blundell. *Magnetism in Condensed Matter.* Oxford University Press, USA, 2000.

[15] W. F. Brown. *Domains, micromagnetics, and beyond: Reminiscences and assessments.* Journal of Applied Physics **49**, 1937–1942 (1978).

[16] P. Yu, X. F. Jin, J. Kudrnovský, D. S. Wang, and P. Bruno. *Curie temperatures of fcc and bcc nickel and permalloy: Supercell and Green's function methods.* Physical Review B **77**, 054431 (2008).

[17] G. Woltersdorf. *Spin-pumping and two-magnon scattering in magnetic multilayers.* Simon Fraser University, PhD thesis, 2004.

[18] G. Wastlbauer and J. A. C. Bland. *Structural and magnetic properties of ultrathin epitaxial Fe films on GaAs(001) and related semiconductor substrates.* Advances in Physics **54**, 137–219 (2005).

[19] B. Heinrich, J. F. Cochran, A. S. Arrott, S. T. Purcell, K. B. Urquhart, J. R. Dutcher, and W. F. Egelhoff. *Development of magnetic anisotropies in ultrathin epitaxial films of Fe(001) and Ni(001).* Applied Physics A **49**, 473–490 (1989).

[20] L. F. Yin, D. H. Wei, N. Lei, L. H. Zhou, C. S. Tian, G. S. Dong, X. F. Jin, L. P. Guo, Q. J. Jia, and R. Q. Wu. *Magnetocrystalline anisotropy in Permalloy revisited.* Phys. Rev. Lett. **97**, 067203 (2006).

[21] T. L. Gilbert and J. M. Kelly. *Conference on magnetism and magnetic materials.* Pittsburgh, PA 253 (1955).

[22] G. Bertotti, I. D. Mayergoyz, and C. Serpico. *Nonlinear magnetization dynamics in nanostructures.* Elsevier, 2009.

[23] W. M. Saslow. *Landau-Lifshitz or Gilbert damping? That is the question.* Journal of Applied Physics **105**, 07D315 (2009).

[24] L. Berger. *Emission of spin waves by a magnetic multilayer traversed by a current.* Phys. Rev. B **54**, 9353–9358 (1996).

[25] J. C. Slonczewski. *Current-driven excitation of magnetic multilayers.* Journal of Magnetism and Magnetic Materials **159**, 1–7 (1996).

[26] P. M. Haney, H.-W. Lee, K.-J. Lee, A. Manchon, and M. D. Stiles. *Current-induced torques and interfacial spin-orbit coupling.* Phys. Rev. B **88**, 214417 (2013).

[27] M. Obstbaum. *Inverse spin Hall effect in metallic heterostructures.* Universität Regensburg, PhD thesis, 2015.

[28] Y. K. Kato, R. C. Myers, A. C. Gossard, and D. D. Awschalom. *Observation of the spin Hall effect in semiconductors.* Science **306**, 1910–1913 (2004).

[29] M. I. Dyakonov and V. I. Perel. *Current-induced spin orientation of electrons in semiconductors.* Physics Letters **A**, 459–460 (1971).

[30] J. E. Hirsch. *Spin Hall effect.* Phys. Rev. Lett. **83**, 1834–1837 (1999).

[31] L. Liu, O. J. Lee, T. J. Gudmundsen, D. C. Ralph, and R. A. Buhrman. *Current-Induced switching of perpendicularly magnetized magnetic layers using spin torque from the spin Hall effect.* Phys. Rev. Lett. **109**, 096602 (2012).

[32] I. M. Miron, K. Garello, G. Gaudin, P.-J. Zermatten, M. V. Costache, S. Auffret, S. Bandiera, B. Rodmacq, A. Schuhl, and P. Gambardella. *Perpendicular switching of a single ferromagnetic layer induced by in-plane current injection.* Nature **476**, 189–193 (2011).

[33] L. Liu, C.-F. Pai, Y. Li, H. W. Tseng, D. C. Ralph, and R. A. Buhrman. *Spin-torque switching with the giant spin Hall effect of tantalum.* Science **336**, 555–558 (2012).

[34] E. M. Hankiewicz, J. Li, T. Jungwirth, Q. Niu, S.-Q. Shen, and J. Sinova. *Charge Hall effect driven by spin-dependent chemical potential gradients and Onsager relations in mesoscopic systems.* Phys. Rev. B **72**, 155305 (2005).

[35] M. D. Stiles and A. Zangwill. *Anatomy of spin-transfer torque.* Phys. Rev. B **66**, 014407 (2002).

[36] L. Liu, T. Moriyama, D. C. Ralph, and R. A. Buhrman. *Spin-torque ferromagnetic resonance Induced by the spin Hall effect.* Phys. Rev. Lett. **106**, 036601 (2011).

[37] M. M. Decker. *Spin current induced control of magnetization dynamics.* Universität Regensburg, PhD thesis, 2018.

[38] C.-F. Pai, Y. Ou, L. H. Vilela-Leao, D. C. Ralph, and R. A. Buhrman. *Dependence of the efficiency of spin Hall torque on the transparency of Pt/ferromagnetic layer interfaces.* Phys. Rev. B **92**, 064426 (2015).

[39] W. Zhang, W. Han, X. Jiang, S.-H. Yang, and S. S. P. Parkin. *Role of transparency of platinum-ferromagnet interfaces in determining the intrinsic magnitude of the spin Hall effect.* Nature Physics **11**, 496 (2015).

[40] T. Nan, S. Emori, C. T. Boone, X. Wang, T. M. Oxholm, J. G. Jones, B. M. Howe, G. J. Brown, and N. X. Sun. *Comparison of spin-orbit torques and spin pumping across NiFe/Pt and NiFe/Cu/Pt interfaces.* Phys. Rev. B **91**, 214416 (2015).

[41] V. Edelstein. *Spin polarization of conduction electrons induced by electric current in two-dimensional asymmetric electron systems.* Solid State Communications **73**, 233–235 (1990).

[42] A. G. Aronov and Y. B. Lyanda-Geller. *Nuclear electric resonance and orientation of carrier spins by an electric field.* Soviet Journal of Experimental and Theoretical Physics Letters **50**, 431 (1989).

[43] Y. K. Kato, R. C. Myers, A. C. Gossard, and D. D. Awschalom. *Current-induced spin polarization in strained semiconductors.* Phys. Rev. Lett. **93**, 176601 (2004).

[44] A. Y. Silov, P. A. Blajnov, J. H. Wolter, R. Hey, K. H. Ploog, and N. S. Averkiev. *Current-induced spin polarization at a single heterojunction.* Applied Physics Letters **85**, 5929–5931 (2004).

[45] Y. Bychkov and E. Rashba. *Properties of a 2D electron gas with lifted spectral degeneracy.* Soviet Journal of Experimental and Theoretical Physics Letters **39**, 78 (1984).

[46] K. Shen, G. Vignale, and R. Raimondi. *Microscopic theory of the inverse Edelstein effect.* Phys. Rev. Lett. **112**, 096601 (2014).

[47] M. Buchner. *Ferromagnet/semiconductor interfaces: spin injection and anisotropic polar magneto-optic Kerr effect.* Universität Regensburg, PhD thesis, 2017.

[48] S. Hunklinger. *Festkörperphysik*, vol. 2. Aufl. München: Oldenbourg Wissenschaftsverlag, 2009.

[49] T. Hupfauer. *Transportanisotropien an Fe/GaAs-Grenzflächen.* Universität Regensburg, PhD thesis, 2015.

[50] R. Moosbühler. *GaAs(001)-Oberflächen-Rekonstruktionen und epitaktische Fe-Schichten auf GaAs(001): Wachstum und magnetische Anisotropie.* Universität Regensburg, PhD thesis, 2003.

[51] G. Bayreuther, M. Dumm, B. Uhl, R. Meier, and W. Kipferl. *Magnetocrystalline volume and interface anisotropies in epitaxial films: Universal relation and Néel's model.* Journal of Applied Physics **93**, 8230–8235 (2003).

[52] G. Bayreuther, J. Premper, M. Sperl, and D. Sander. *Uniaxial magnetic anisotropy in Fe/GaAs(001): Role of magnetoelastic interactions.* Phys. Rev. B **86**, 054418 (2012).

[53] R. Moosbühler, F. Bensch, M. Dumm, and G. Bayreuther. *Epitaxial Fe films on GaAs(001): Does the substrate surface reconstruction affect the uniaxial magnetic anisotropy?* Journal of Applied Physics **91**, 8757–8759 (2002).

[54] M. Gmitra and J. Fabian. *First-principles studies of orbital and spin-orbit properties of GaAs, GaSb, InAs and InSb zinc-blende and wurtzite semiconductors.* Phys. Rev. B **94**, 165202 (2016).

[55] S. D. Ganichev, M. Trushin, and J. Schliemann. *Spin polarisation by current.* ArXiv **1606**, 1–10 (2016).

[56] P. Gambardella and I. M. Miron. *Current-induced spin-orbit torques.* Phil. Trans. R. Soc. A **369**, 3175–3197 (2011).

[57] F. T. Vas'ko and N. A. Prima. *Spin splitting in the spectrum of two-dimensional electrons due to the surface potential.* Journal of Experimental and Theoretical Physics Letters **30**, 541 (1979).

[58] E. I. Rashba. *Properties of semiconductors with an extremum loop. 1. Cyclotron and combinational resonance in a magnetic field perpendicular to the plane of the loop.* Sov. Phys. Solid State **2**, 1224–1238 (1960).

[59] G. Dresselhaus. *Spin-orbit coupling effects in zinc blende structures.* Phys. Rev. **100**, 580–586 (1955).

[60] U. Rössler and J. Kainz. *Microscopic interface asymmetry and spin-splitting of electron subbands in semiconductor quantum structures.* Solid State Communications **121**, 313–316 (2002).

[61] E. L. Ivchenko and G. E. Pikus. *New photogalvanic effect in gyrotropic crystals.* Journal of Experimental and Theoretical Physics Letters **27**, 604 (1978).

[62] J. B. Miller, D. M. Zumbühl, C. M. Marcus, Y. B. Lyanda-Geller, D. Goldhaber-Gordon, K. Campman, and A. C. Gossard. *Gate-controlled spin-orbit quantum interference effects in lateral transport.* Phys. Rev. Lett. **90**, 076807 (2003).

[63] J. Moser, A. Matos-Abiague, D. Schuh, W. Wegscheider, J. Fabian, and D. Weiss. *Tunneling anisotropic magnetoresistance and spin-orbit coupling in* Fe/GaAs/Au *tunnel junctions.* Phys. Rev. Lett. **99**, 056601 (2007).

[64] S. Ganichev and W. Prettl. *Spin photocurrents in quantum wells.* Journal of Physics: Condensed Matter **15**, R935 (2003).

[65] S. A. Tarasenko. *Interference of spin splittings in magneto-oscillation phenomena in two-dimensional systems.* Journal of Experimental and Theoretical Physics Letters **75**, 552–555 (2002).

[66] N. S. Averkiev, L. E. Golub, and M. M. Willander. *Spin relaxation anisotropy in two-dimensional semiconductor systems.* Journal of Physics: Condensed Matter **14**, R271 (2002).

[67] J. Schliemann, J. C. Egues, and D. Loss. *Nonballistic spin-field-effect transistor.* Phys. Rev. Lett. **90**, 146801 (2003).

[68] S. D. Ganichev, E. L. Ivchenko, V. V. Bel'kov, S. A. Tarasenko, M. Sollinger, D. Weiss, W. Wegscheider, and W. Prettl. *Spin-galvanic effect.* Nature **417**, 153 (2002).

[69] S. Giglberger, L. E. Golub, V. V. Bel'kov, S. N. Danilov, D. Schuh, C. Gerl, F. Rohlfing, J. Stahl, W. Wegscheider, D. Weiss, W. Prettl, and S. D. Ganichev. *Rashba and Dresselhaus spin splittings in semiconductor quantum wells measured by spin photocurrents.* Phys. Rev. B **75**, 035327 (2007).

[70] A. Manchon and S. Zhang. *Theory of spin torque due to spin-orbit coupling.* Physical Review B **79**, 094422 (2009).

[71] A. Matos-Abiague and R. L. Rodríguez-Suárez. *Spin-orbit coupling mediated spin torque in a single ferromagnetic layer.* Phys. Rev. B **80**, 094424 (2009).

[72] H. G. Bauer. *Linear and nonlinear magnetization dynamics in thin ferromagnetic films and nanostructures.* Universität Regensburg, PhD thesis, 2014.

[73] G. Abo, Y.-K. Hong, J. Park, J. Lee, W. Lee, and B.-C. Choi. *Definition of magnetic exchange length.* IEEE Transactions on Magnetics **49**, 4937–4939 (2013).

[74] J. Stigloher, M. Decker, H. S. Körner, K. Tanabe, T. Moriyama, T. Taniguchi, H. Hata, M. Madami, G. Gubbiotti, K. Kobayashi, T. Ono, and C. H. Back. *Snell's law for spin waves.* Phys. Rev. Lett. **117**, 037204 (2016).

[75] B. A. Kalinikos and A. N. Slavin. *Theory of dipole-exchange spin wave spectrum for ferromagnetic films with mixed exchange boundary conditions.* Journal of Physics C: Solid State Physics **19**, 7013 (1986).

[76] A. G. Gurevich. *Magnetization oscillations and waves.* Boca Raton: CRC Press, 1st ed ed., 1996.

[77] H. Körner. *Time-resolved Kerr microscopy of spin waves propagating in magnetic nanostructures.* Universität Regensburg, PhD thesis, 2017.

[78] C. Bayer, J. Jorzick, S. O. Demokritov, A. N. Slavin, K. Y. Guslienko, D. V. Berkov, N. L. Gorn, M. P. Kostylev, and B. Hillebrands, *Spin-wave excitations in finite rectangular elements*, vol. 111, 57-103. Springer Berlin Heidelberg, (2006).

[79] P. Bryant and H. Suhl. *Thin-film magnetic patterns in an external field.* Applied Physics Letters **54**, 2224–2226 (1989).

[80] J. Jorzick, S. O. Demokritov, B. Hillebrands, M. Bailleul, C. Fermon, K. Y. Guslienko, A. N. Slavin, D. V. Berkov, and N. L. Gorn. *Spin wave wells in nonellipsoidal micrometer size magnetic elements.* Phys. Rev. Lett. **88**, 047204 (2002).

[81] J. P. Park, P. Eames, D. M. Engebretson, J. Berezovsky, and P. A. Crowell. *Spatially Resolved Dynamics of Localized Spin-Wave Modes in Ferromagnetic Wires.* Phys. Rev. Lett. **89**, 277201 (2002).

[82] P. Bruno, Y. Suzuki, and C. Chappert. *Magneto-optical Kerr effect in a paramagnetic overlayer on a ferromagnetic substrate: A spin-polarized quantum size effect.* Phys. Rev. B **53**, 9214–9220 (1996).

[83] Y. Wang, R. Ramaswamy, and H. Yang. *FMR-related phenomena in spintronic devices.* Journal of Physics D: Applied Physics **51**, 273002 (2018).

[84] W. Thomson. *On the electro-dynamic qualities of metals: Effects of magnetization on the electric conductivity of nickel and of iron.* Proceedings of the Royal Society of London **8**, 546–550 (1857).

[85] N. Mecking, S. Gui, Y. and C.-M. Hu. *Microwave photovoltage and photoresistance effects in ferromagnetic microstrips.* Physical Review B **76** (2007).

[86] D. Fang. *Current-induced torque driven ferromagnetic resonance in magnetic microstructures.* University of Cambridge, PhD thesis, 2011.

[87] J. C. Sankey, Y.-T. Cui, J. Z. Sun, J. C. Slonczewski, R. A. Buhrman, and D. C. Ralph. *Measurement of the spin-transfer-torque vector in magnetic tunnel junctions.* Nature Physics **4**, 67 (2007).

[88] H. Kurebayashi, J. Sinova, D. Fang, A. C. Irvine, T. D. Skinner, J. Wunderlich, V. Novák, R. P. Campion, B. L. Gallagher, E. K. Vehstedt, L. P. Zărbo, K. Výborný, A. J. Ferguson, and T. Jungwirth. *An antidamping spin-orbit torque originating from the Berry curvature.* Nature Nanotechnology **9**, 211 (2014).

[89] T. D. Skinner, K. Olejník, L. K. Cunningham, H. Kurebayashi, R. P. Campion, B. L. Gallagher, T. Jungwirth, and A. J. Ferguson. *Complementary spin-Hall and inverse spin-galvanic effect torques in a ferromagnet/semiconductor bilayer.* Nature Communications **6**, 6730 (2015).

[90] K. Ando, S. Takahashi, K. Harii, K. Sasage, J. Ieda, S. Maekawa, and E. Saitoh. *Electric manipulation of spin relaxation using the spin Hall effect.* Phys. Rev. Lett. **101**, 036601 (2008).

[91] K. Y. Guslienko, S. O. Demokritov, B. Hillebrands, and A. N. Slavin. *Effective dipolar boundary conditions for dynamic magnetization in thin magnetic stripes.* Phys. Rev. B **66**, 132402 (2002).

[92] J. M. Shaw, T. J. Silva, M. L. Schneider, and R. D. McMichael. *Spin dynamics and mode structure in nanomagnet arrays: Effects of size and thickness on linewidth and damping.* Phys. Rev. B **79**, 184404 (2009).

[93] D. Wu, G. Yu, Q. Shao, X. Li, H. Wu, K. L. Wong, Z. Zhang, X. Han, K. A. Pedram, and K. L. Wang. *In-plane current-driven spin-orbit torque switching in perpendicularly magnetized films with enhanced thermal tolerance.* Applied Physics Letters **108** (2016).

[94] A. Vansteenkiste, J. Leliaert, M. Dvornik, M. Helsen, F. Garcia-Sanchez, and B. Van Waeyenberge. *The design and verification of MuMax3.* AIP Advances **4**, 107133 (2014).

[95] Langley. *The bolometer.* Nature **25**, 14–16 (1881).

[96] J. M. D. Coey. *Magnetism and magnetic materials.* Cambridge: Cambridge University Press, 2010.

[97] S. Kasai, K. Kondou, H. Sukegawa, S. Mitani, K. Tsukagoshi, and Y. Otani. *Modulation of effective damping constant using spin Hall effect.* Applied Physics Letters **104**, 092408 (2014).

[98] A. Bose, S. Dutta, S. Bhuktare, H. Singh, and A. A. Tulapurkar. *Sensitive measurement of spin-orbit torque driven ferromagnetic resonance detected by planar Hall geometry.* Applied Physics Letters **111**, 162405 (2017).

[99] C. T. Boone, J. M. Shaw, H. T. Nembach, and T. J. Silva. *Spin-scattering rates in metallic thin films measured by ferromagnetic resonance damping enhanced by spin-pumping.* Journal of Applied Physics **117**, 223910 (2015).

[100] J. C. Rojas-Sánchez, L. Vila, G. Desfonds, S. Gambarelli, J. P. Attané, J. M. De Teresa, C. Magén, and A. Fert. *Spin-to-charge conversion using Rashba coupling at the interface between non-magnetic materials.* Nature Communications **4**, 2944 (2013).

[101] A. Azevedo, L. H. Vilela-Leão, R. L. Rodríguez-Suárez, A. F. Lacerda Santos, and S. M. Rezende. *Spin pumping and anisotropic magnetoresistance voltages in magnetic bilayers: Theory and experiment.* Phys. Rev. B **83**, 144402 (2011).

[102] Y. Wang, P. Deorani, X. Qiu, J. H. Kwon, and H. Yang. *Determination of intrinsic spin Hall angle in Pt.* Applied Physics Letters **105**, 152412 (2014).

[103] E. Sagasta, Y. Omori, M. Isasa, M. Gradhand, L. E. Hueso, Y. Niimi, Y. Otani, and F. Casanova. *Tuning the spin Hall effect of Pt from the moderately dirty to the superclean regime.* Phys. Rev. B **94**, 060412 (2016).

[104] M.-H. Nguyen, D. C. Ralph, and R. A. Buhrman. *Spin Torque Study of the Spin Hall Conductivity and Spin Diffusion Length in Platinum Thin Films with Varying Resistivity.* Phys. Rev. Lett. **116**, 126601 (2016).

[105] M. Isasa, E. Villamor, L. E. Hueso, M. Gradhand, and F. Casanova. *Temperature dependence of spin diffusion length and spin Hall angle in Au and Pt.* Phys. Rev. B **91**, 024402 (2015).

[106] J. Kim, J. Sinha, M. Hayashi, M. Yamanouchi, S. Fukami, T. Suzuki, S. Mitani, and H. Ohno. *Layer thickness dependence of the current-induced effective field vector in Ta|CoFeB|MgO.* Nature Materials **12**, 240 (2012).

[107] M. Montazeri, P. Upadhyaya, M. C. Onbasli, G. Yu, K. L. Wong, M. Lang, Y. Fan, X. Li, P. Khalili Amiri, R. N. Schwartz, C. A. Ross, and K. L. Wang. *Magneto-optical investigation of spin-orbit torques in metallic and insulating magnetic heterostructures.* Nature Communications **6**, 8958 (2015).

[108] T. Hupfauer, A. Matos-Abiague, M. Gmitra, F. Schiller, J. Loher, D. Bougeard, C. H. Back, J. Fabian, and D. Weiss. *Emergence of spin-orbit fields in magnetotransport of quasi-two-dimensional iron on gallium arsenide.* Nature Communications **6**, 7374 (2015).

[109] H. Danan, A. Herr, and A. J. P. Meyer. *New determinations of the saturation magnetization of nickel and iron.* Journal of Applied Physics **39**, 669–670 (1968).

[110] S. Fukami, C. Zhang, S. DuttaGupta, A. Kurenkov, and H. Ohno. *Magnetization switching by spin-orbit torque in an antiferromagnet-ferromagnet bilayer system.* Nature Materials **15**, 535 (2016).

Danksagung

Meinen herzlichen Dank geht an folgende Personen:
Prof. Christian H. Back, für die Dokotorandenstelle an diesem Lehrstuhl und die Möglichkeit an diesem interessanten Thema zu arbeiten. Außerdem dafür, dass ich mich an mehreren verschiedenen Experimenten inklusive dem Aufbau einer Vakuumkammer beteiligen konnte und desweiteren mir ermöglichte, meine Forschungsergebnisse auf Konferenzen in Deutschland und Europa zu präsentieren.
Martin Decker, für die tolle Zusammenarbeit beim Proben herstellen, die Möglichkeit meine Proben im Laseraufbau messen zu dürfen, sowie die Diskussionen und Interpretation der Ergebnisse.
Matthias Kronseder, für das Wachstum zahlreicher Schichten, die Hilfe beim Betrieb der Vakuumanlagen und den vielen Diskussionen.
Johannes Stigloher, für die Diskussionen über die Spinwellen und der Hilfe bei dem Algorithmus der Mumax3 Simulationen.
Lin Chen, für die Interpretation der elektrischen SOT-FMR Messungen.
Helmut Körner, für die unzähligen SQUID Messungen an den verschiedenen Proben.
Maximilian Schmid und Stefan Günther, für die Einweisung in die Vakuumtechnik und Betreuung der Anlagen.
Martin Obstbaum, für die Anleitung zur Herstellung strukturierter Proben und elektrischen Messungen.
Markus Hollnberger, für die technische Unterstützung bei der Planung und Herstellung von Bauteilen.
Die Mechanik- und Elektronik-Werkstatt, die meine Bauteile perfekt hergestellt haben.
Magdalena Pfleger, Sylvia Hrdina, Claudia Zange und Doris Meier für die Hilfe bei allen administrativen Sachen.
Dem restlichen Lehrstuhl für die Geselligkeit, zahlreichen Dultbesuche und Lehrstuhlausfüge.
Meinen Eltern und meiner Schwester für die Unterstützung in allen Lebensbereichen.

Publication list

2018

Electric-field control of interfacial spin-orbit fields
L. Chen, M. Gmitra, M. Vogel, R. Islinger, M. Kronseder, D. Schuh, D. Bougeard, J. Fabian, D. Weiss and C. H. Back
Nature Electronics 1, 6, 350-355

2016

Robust spin-orbit torque and spin-galvanic effect at the Fe/GaAs (001) interface at room temperature
L. Chen, M. Decker, M. Kronseder, R. Islinger, M. Gmitra, D. Schuh, D. Bougeard, J. Fabian, D. Weiss and C. H. Back
Nature Communications 7, 13802

2014

Magnetic damping: domain wall dynamics versus local ferromagnetic resonance
T. Weindler, H. G. Bauer, R. Islinger, B. Böhm, J.-Y. Chauleau, and C. H. Back
Phys. Rev. Lett. 113, 237204